

Stefan Schade

## MHD Stability of ASDEX Upgrade and TEXTOR-94 Advanced Scenarios

# MHD Stability of ASDEX Upgrade and TEXTOR-94 Advanced Scenarios

Dissertation

Zur Erlangung des akademischen Grades  
Doktor der Naturwissenschaften  
(doctor rerum naturalium)

vorgelegt

der Mathematisch-Naturwissenschaftlichen Fakultät  
der Universität Rostock



von

Diplom-Physiker Stefan Schade  
geb. am 29.12.1972 in Braunfels

Rostock 2001

Gutachter:

*Prof. Dr. G. Röpke  
Fachbereich Physik  
Universität Rostock  
D-18051 Rostock  
Germany*

*Prof. Dr. S. Günter  
Max-Planck-Institut für Plasmaphysik  
Boltzmanstraße 2  
D-85748 Garching  
Germany*

*Dr. T. Hender  
EURATOM/UKAEA Fusion Association  
Culham Science Centre  
Abingdon  
Oxfordshire  
OX14 3DB  
United Kingdom*

Zur Erinnerung an meinen Vater  
Ing. grad. Horst Schade  
(1942-2000)

# Abstract

The inductive current drive limits conventional tokamaks to pulsed operation, which is unfavorable for a power producing reactor. For this reason, "advanced" tokamak scenarios which avoid this problem have been investigated in depth throughout the last decade. Unfortunately because of their special properties, these equilibria have the disadvantage that they are susceptible to certain magnetohydrodynamic (MHD) instabilities. Since these can deteriorate the confinement or even cause disruptions a close examination of the observed dynamics is of interest.

This thesis analyses advanced scenario experiments performed on TEXTOR-94 and on ASDEX Upgrade. Numerical simulations have been carried out and the results compared to the experimental measurements. The observed instabilities have been identified as double tearing modes, infernal modes, external kink modes or as a combination of these.

In addition to comparing the experimental results and numerical simulations as a mean to explain the plasma dynamics by the presence of a certain mode, this strategy also presents a way to examine the influence of certain experimental parameters such as a differential rotation of the plasma, the change of the magnetic structure or the influence of the pressure on the mode's growth.

The stabilisation of external modes by a conducting structure in the vicinity of the plasma surface has also been estimated for a kink unstable ASDEX Upgrade equilibrium.

## Deutschsprachiges Vorwort:

Ziel der fusionsorientierten Plasmaphysik ist die Nutzung der bei der Verschmelzung leichter Nuklide freiwerdenden Energie zur Produktion elektrischen Stroms. Daraus ergibt sich die Notwendigkeit, ein heißes, ionisiertes Gas bei möglichst hoher Dichte und Temperatur einzuschließen und thermisch zu isolieren. Eine Möglichkeit dafür bietet der Tokamak. Dabei werden die geladenen Teilchen durch eine Magnetfeldkonfiguration eingeperrt, welche ineinandergeschachtelte Tori aufspannt. Ein Gleichgewicht zwischen Magnetfeldkräften und dem kinetischen Druck des Plasmas wird jedoch bei konventionellem Betrieb aufgrund des induktiven Stromtriebes nur transient erreicht. Da für einen späteren Reaktorbetrieb eine kontinuierliche Stromproduktion wünschenswert ist, ist die Entwicklung eines stationären Tokamaks von großem Interesse. Als ein Konzept hierfür werden die "advanced" Szenarien an zahlreichen Experimenten untersucht. Dabei hat sich eine besondere Anfälligkeit gegenüber Instabilitäten offenbart: Abweichungen vom Gleichgewichtszustand können wachsen und den Einschluß verringern oder sogar das Kräftegleichgewicht zerstören, was zu einem disruptiven Ende der jeweiligen Entladung führt. Solche Instabilitäten bilden daher ein Hindernis sowohl für einen stationären Betrieb als auch für einen guten Einschluß und einen hohen Plasmadruck. Damit erschweren sie den Zugang zu einem brennenden Plasma.

Da folglich ein tieferes Verständnis der auftretenden Effekte von großem Interesse ist, untersucht die vorliegende Promotionsschrift verschiedene Instabilitäten. Verwendet wird dazu die Magnetohydrodynamik (MHD), welche das Plasma in einem Einflüssigkeitsbild beschreibt. Das Model erlaubt sowohl die Berechnung des Gleichgewichtszustandes als auch die Ableitung von linearisierten Stabilitätsgleichungen für Störgrößen, die auf ein Eigenwertproblem zurückgeführt, mittels existierender Computercodes gelöst werden können.

Es werden advanced Szenarien an den Tokamaks TEXTOR-94 und ASDEX Upgrade untersucht. Die vorgestellten Simulationen und der Vergleich mit Messungen ermöglichen die Identifikation der im Experiment beobachteten Aktivitäten als "Double-Tearing-Moden", "Infernal-Moden" und "Externe-Kink-Moden", bzw. als Kombination dieser. Der Einfluss verschiedener experimentrelevanter Parameter wie einer differentiellen Bewegung des Plasmas oder der Veränderung der magnetischen Struktur, des Druckes etc. wurden untersucht.

Darüber hinaus ermöglichen die vorgestellten Rechnungen einen tieferen Einblick in die, dem Verhalten der Instabilitäten zugrundeliegenden Mechanismen, insbesondere in die Kopplung und Entkopplung verschiedener Moden. Damit tragen die Untersuchungen zur Umgehung von Instabilitäten in zukünftigen Experimenten und damit zur Verbesserung des Einschlusses und einer weiteren Annäherung an die Zündbedingung bei.

Neben der Optimierung von Plasmaparametern wurde die Stabilisierung externer Moden mittels einer leitenden Struktur in der Nähe der Plasmaoberfläche angeregt. Am Beispiel von ASDEX Upgrade wird die durch eine derartige Anordnung zu erwartende Stabilisierung abgeschätzt.

Stefan Schade im Mai 2001

# Contents

<b>1</b>	<b>General Introduction</b>	<b>1</b>
<b>2</b>	<b>Theoretical Review</b>	<b>7</b>
2.1	Magnetohydrodynamics (MHD) . . . . .	7
2.1.1	Derivation . . . . .	7
2.1.2	One Fluid Resistive MHD Equations . . . . .	9
2.1.3	Timescales of MHD . . . . .	9
2.1.4	Resistivity and Flux Conservation . . . . .	11
2.2	Equilibrium . . . . .	11
2.2.1	From Force Balance to Toroidicity . . . . .	11
2.2.2	Toroidal Equilibria . . . . .	13
2.2.3	Bootstrap Current . . . . .	15
2.3	Stability . . . . .	17
2.3.1	Static Linear MHD . . . . .	17
2.3.2	The Energy Functional $\delta W$ . . . . .	19
2.3.3	The Linear Stability Code CASTOR . . . . .	20
2.3.4	Stability of a Rotating Plasma . . . . .	21
<b>3</b>	<b>Tokamak Research</b>	<b>22</b>
3.1	Modes of Operation . . . . .	22
3.1.1	Ohmic Plasmas . . . . .	22
3.1.2	L-Mode . . . . .	22
3.1.3	H-Mode . . . . .	22
3.1.4	Advanced Mode . . . . .	24
3.2	MHD Instabilities . . . . .	26
3.2.1	Tearing Modes (TM) . . . . .	26
3.2.2	Coupling and Double Tearing Modes (DTM) . . . . .	30
3.2.3	Kink Modes . . . . .	31



3.2.4	Ballooning Modes . . . . .	33
3.2.5	Infernal Modes . . . . .	34
<b>4</b>	<b>Decoupling of DTMs in TEXTOR-94</b>	<b>35</b>
4.1	DTM Activity in the Experiment . . . . .	36
4.1.1	The Device . . . . .	36
4.1.2	Reversed Shear Scenarios . . . . .	36
4.1.3	Internal Disruptions . . . . .	37
4.1.4	Equilibrium Properties . . . . .	38
4.2	The Plasma is Susceptible to the DTM . . . . .	40
4.2.1	Equilibrium Reconstruction . . . . .	41
4.2.2	Linear Calculations Yield DTM Activity . . . . .	42
4.3	Decoupling Mechanisms of the 2/1 DTM . . . . .	46
4.3.1	Decoupling by Distance . . . . .	46
4.3.2	Decoupling by Differential Rotation . . . . .	52
4.4	Application to the Experiment . . . . .	64
4.4.1	The Plasma is Unstable to DTM . . . . .	65
4.4.2	Differential Rotation can Contribute to a Stabilisation . . . . .	66
<b>5</b>	<b>MHD in ASDEX Upgrade Advanced Scenarios</b>	<b>67</b>
5.1	Experimental Background . . . . .	68
5.1.1	The Device . . . . .	68
5.1.2	ASDEX Upgrade Advanced Scenarios . . . . .	68
5.2	Technical Remarks . . . . .	69
5.3	Double Tearing Modes . . . . .	70
5.3.1	Experimental Observations . . . . .	70
5.3.2	Identification of the Mode . . . . .	70
5.3.3	Discussion of the Mode Dynamics . . . . .	72
5.4	Infernal Modes . . . . .	75
5.4.1	Experimental Observation . . . . .	75
5.4.2	Identification and Discussion . . . . .	76
5.5	External Kink Modes . . . . .	78
5.5.1	External Kink Modes Limit $\beta_N$ in Advanced Scenarios . . . . .	78
5.5.2	Wall Stabilisation . . . . .	80
5.6	Coupling Between Kink and Infernal Modes . . . . .	83

<b>6</b>	<b>Summary and Conclusion</b>	<b>85</b>
6.1	The Work Contributed to an Understanding of the Experiments . . .	85
6.1.1	TEXTOR-94 . . . . .	85
6.1.2	ASDEX Upgrade . . . . .	86
6.2	One can Recomend Strategies to Avoid Activities . . . . .	87
<b>A</b>	<b>Publications</b>	<b>96</b>
A.1	Contribution to Articles . . . . .	96
A.2	Contributions to Conference Presentations . . . . .	97
<b>B</b>	<b>Danksagung</b>	<b>99</b>
<b>C</b>	<b>Curriculum Vitae</b>	<b>100</b>
<b>D</b>	<b>Erklärung</b>	<b>101</b>

# Chapter 1

## General Introduction

Despite efforts to the contrary, technical progress and increasing wealth are likely to cause a further increase of the world's energy needs especially if developing countries are accounted for. Though the supply of natural gas and oil is assured for at least intermediate time periods, the extensive use of carbon based fuels and the accompanied emission of  $CO_2$  into the earth's atmosphere seems to affect the climate. Since the consequences of the potential climate change can be regarded as a huge threat it seems sensible to consider alternative sources of energy. Nuclear fusion presents one alternative to the use of fossil fuels.

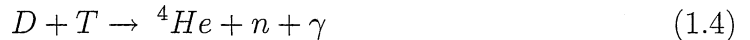
Nuclear power can be released through fission of heavy nuclei into middle weighted fragments. As these contain a statistical number of nucleons one has to deal with a mixture of many isotopes. Among these there are ones with extremely long lifetimes, which gives rise to the problem of safely storing the nuclear waste for geological timescales. Yet another problem emerges because current reactors contain the fuel for very long time periods, so they have to be regulated artificially to be kept from criticality. Since 1986 when the Chernobyl disaster occurred, the public support to this technology wanes. Fusion would also produce nuclear waste because neutrons activate the structures they encounter, but by the use of materials with light nuclei one can limit the production of long lived radioactive isotopes [1]. In contrast to a fission reactor, a fusion reactor is continuously fuelled thereby limiting the amount of energy that could be liberated in the event of an accident. Renewable energy sources also present intriguing alternatives, but as fusion itself they are not developed enough to provide a solution to the stated problems. It seems advisable to follow different strategies to provide a supply of clean, reliable and efficient power.

Terrestrial fusion has been inspired by the process in the sun. There the main reactions are as follows:



Since the process 1.1 is based on the weak interaction the reaction is slow, which is reflected in the sun's long lifetime. Terrestrial plasmas are much smaller, therefore a higher reaction rate is needed, ruling out weak processes.

For a fusion reaction to occur, the two nuclei have to "touch" each other by tunneling through the repulsive coulomb wall. Therefore the fusion cross sections are energy dependent and the process requires high temperatures ( $1 \text{ eV} \approx 1.16 \cdot 10^4 \text{ }^\circ\text{C}$ ). At achievable energies ( $< 20 \text{ keV}$ ) one favours the reaction



where the emerging  $\alpha$ -particle has a kinetic energy of 3.54 MeV. The aim is an ignited plasma, where all energy losses are compensated by  $\alpha$ -particles from the fusion reactions, which transfer their energy to the plasma while slowing down.

All thermal energy transport processes like diffusion, convection and others are described by the energy confinement time

$$\tau_E = \frac{\int n k (T_i + T_e) d^3x}{P}, \quad (1.5)$$

where  $P$  is the total power, that has to be deposited in the plasma to sustain steady state and  $n$  is the particle density. Thus the power loss is described by the thermal energy over the confinement time  $\frac{3}{2} n k (T_i + T_e) / \tau_E$ . It turns out that the condition for ignition can be reduced to a threshold for the so called triple product [2]:

$$n \tau_E T > 3 \cdot 10^{21} \frac{\text{keV s}}{\text{m}^3} \quad (1.6)$$

Thus a hot and dense plasma has to be well insulated to ignite. There are different approaches to fulfill this criteria: "inertial fusion" creates very dense plasmas for very short time intervals, while "magnetic fusion" confines a relatively thin, hot plasma for long times.

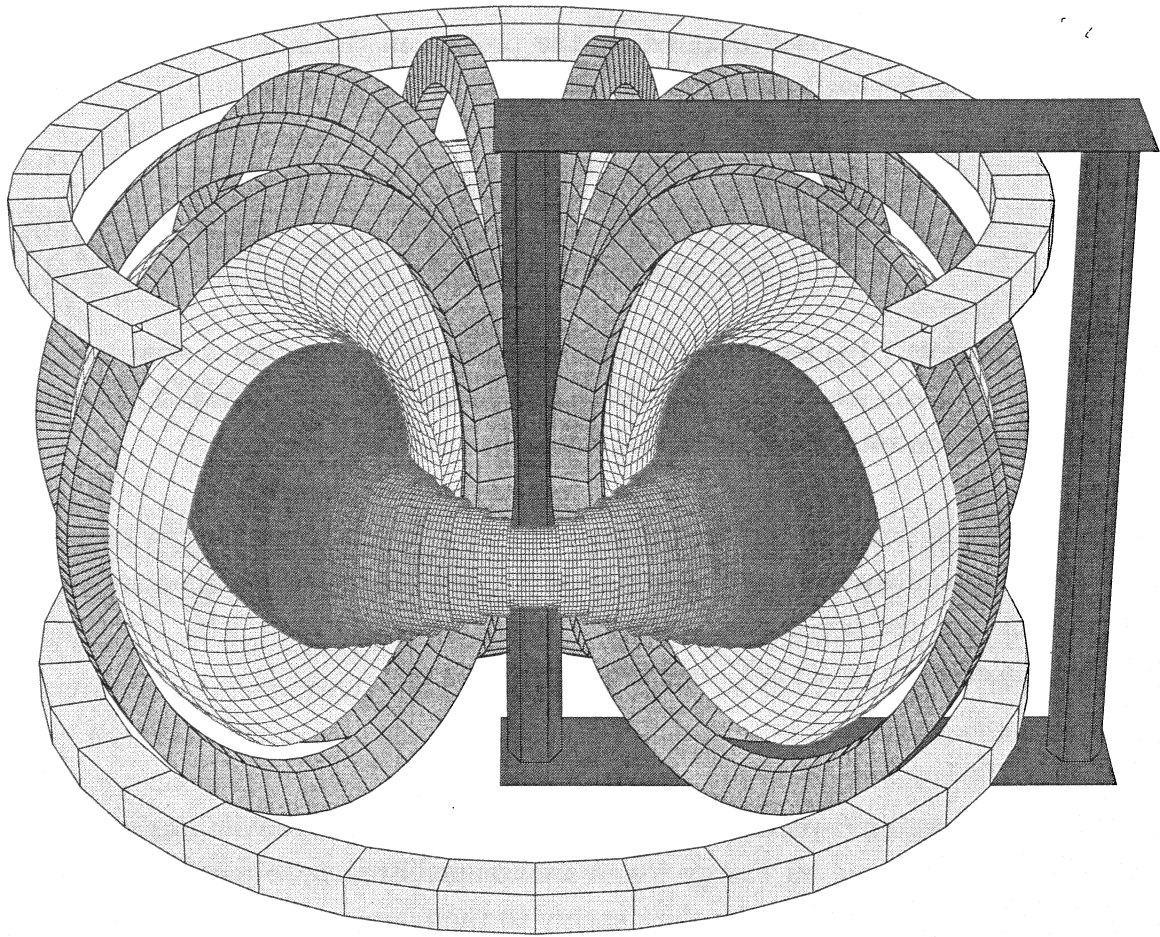


Figure 1.1: The tokamak configuration consists of the vacuum vessel (gray), the induction coil (red), and the toroidal field coils (green). The plasma particles in the vessel are confined to nested tori providing a thermal insulation. (The axisymmetric device has been cut open to exhibit all details.)

### Tokamaks

The configuration of the tokamak was proposed by A. Sacharov and realised by L. Artsimovich in Russia (1952). The name stands for “TOroidalnaya KAmera s MAgnitnymi Katuschkami” (toroidal chamber with magnetic field coils). Though further approaches like the non-axisymmetric stellarator exist, tokamak plasmas present the method to get closest to the ignition condition (Eq. 1.6) in the laboratory nowadays. They exhibit the highest temperature gradients known.

The structure of a tokamak is shown in Fig. 1.1. It confines the plasma by a magnetic field: Poloidal coils are wound around the torus and produce a toroidal magnetic field of a few Tesla. A toroidal current is driven in the plasma by induction generating a smaller poloidal field. The resulting field lines run helically on the shown set of nested tori. As the charged constituents of the plasma gyrate around the magnetic field lines each one is bound to a certain torus within one Lamor radius. Thus the magnetic field provides an insulation, permitting central temperatures of several keV in the plasma centre.

The plasma equilibrium can be described with “magnetohydrodynamics” (MHD) as described in Sect. 2.1. Sect. 2.2 presents how the force, caused by the kinetic pressure is balanced by the magnetic force. The stability of such an MHD equilibrium to a perturbation is regarded in Sect. 2.3.

Throughout the history of tokamak research it was possible to improve the confinement by exploring various modes of operation, as will be described in Sect. 3.1. The **H-factor** has been introduced to describe this advance. It is defined as the confinement time (Eq. 1.5) of a particular discharge over the one of a reference shot.

$$H = \frac{\tau_E}{\tau_L} \quad (1.7)$$

where  $\tau_L$  stands for the energy confinement time of an “L-mode” plasma (Sect. 3.1.2). So called H-mode plasmas (Sect. 3.1.3) exhibit an improved confinement  $H \approx 2$  which is the reason for the name “H(igh energy confinement)-factor”.

The “normalised  $\beta$ ” gives the ratio of the energy, stored in the kinetic pressure over the magnetic field energy. It is defined as:

$$\beta_N = \frac{\langle p \rangle a}{BI/2\mu_0} \quad (1.8)$$

Where  $a$  is the minor radius of the device,  $B$  denotes the magnetic field,  $\langle p \rangle$  is the average pressure, and  $I$  is the plasma current. Since the generation of the magnetic field is associated with high costs and a high pressure is desirable with respect to the triple product (Eq. 1.6), a high value for  $\beta_N$  is wanted. High pressure equilibria however give rise to numerous instabilities, some of which are described in Sect. 3.2. These degrade the confinement and result in a reduced H-factor or a disruption of

the discharge, which terminates the equilibrium. Thus it is of advantage to maximise the product  $\beta_N H$ . While maximum values of  $H$  approach 4, the product is reaching optimal values of  $\beta_N \cdot H \approx 9$  at  $H$ -values below 3 [3].

### Advanced Scenarios

The use of an inductive drive for the toroidal current limits the tokamak to pulsed operation. As the output of a power plant should be continuous, this is a big disadvantage for a power producing reactor. A new mode of operation, the “advanced scenario” (Sect. 3.1.4) tries to improve this situation using an intrinsic current that is caused by the pressure gradient and does not depend on an external drive (this “bootstrap current” is explained in Sect. 2.2.3). In addition this type of equilibrium can be associated with a transport barrier yielding an improved confinement and high H-factors. Optimising equilibria for a high bootstrap current, one is aiming for an ignited “steady state” tokamak. The condition for ignition and the fraction of the bootstrap current are therefore the figures of merit. They can be estimated for future devices from empirical scaling laws. The energy multiplication factor  $Q$  scales like [4, 5]:

$$g(\dots) \left( \frac{H I_{[MA]} R}{60 a} \right)^3 = \frac{Q}{Q + 5} \quad (1.9)$$

where  $g(\dots)$  is of the order unity,  $a$  represents the minor,  $R$  the major radius of the tokamak and  $I$  the plasma current. For ignition  $Q \rightarrow \infty$  and  $H I_{[MA]} R/a \geq 60$ . With  $\kappa$  denoting the elongation of the plasma cross section, the bootstrap current fraction scales as [6]:

$$f_{BS} \approx 0.1 \underbrace{H \beta_N}_I \underbrace{\sqrt{a R}}_{II} B (1 + \kappa^2) \quad (1.10)$$

Designs for conventional ignition devices did fulfill condition 1.9 by increasing the total current. Since this would reduce the bootstrap fraction (see Eq. 1.8 and Eq. 1.10) it is not a suitable strategy for advanced scenarios. The inverse aspect ratio  $\epsilon = a/R$  does not leave room for many changes either, so the confinement parameter  $H$  is of paramount importance for ignition.

Optimising the bootstrap current fraction by increasing term II in Eq. 1.10 would produce high costs as it represents the geometrical scale of the device.  $B$  is limited by the magnetic fields accessible with superconducting toroidal coils (circa 10 T). Finally the elongation  $\kappa$  cannot be increased to much as it gives rise to a vertical

shift of the plasma, the “vertical instability”. Thus an optimisation of the H-factor and the plasma pressure  $\beta_N$ , represented by term I are important.

### Magnetohydrodynamic Instabilities

The increase of the plasma pressure and  $\beta_N$  results in a stronger pressure gradient. As mentioned, this evokes instabilities, which can cause transport and degrade the confinement resulting in a reduction of the H-factor or even lead to a disruptive end of the discharge. Other instabilities are caused by the current gradient. Due to the special properties of advanced scenario type equilibria, instabilities constitute a challenge already for current experiments, which are transient because the pressure is too small to generate enough bootstrap current. Thus it is essential to gain further insight into the dynamics of MHD activities to combine high pressure and good confinement. As shown, an improvement in MHD stability could be utilized to obtain either one, or a combination of the following advantages:

- An increase of the bootstrap current fraction gives access to a steady state tokamak.
- It would be possible to reduce the machine’s size and cost at no expense for the plasma performance.
- Ignition could be reached more easily with a better confinement.

This is the reason, why careful analysis of the MHD activity in current experiments, the exploration of means of stabilisation and a deeper insight into the dynamics involved is of interest for fusion physics nowadays. In the work presented here, the MHD activity in advanced mode discharges on two tokamaks is analysed and means of stabilisation are discussed.



# Chapter 2

## Theoretical Review

### 2.1 Magnetohydrodynamics (MHD)

To deal with the many body problem of a hot, ionised plasma, a fluid picture offers the easiest treatment of the ensemble. A closed system is derived from the velocity moments of the kinetic equation for the ion and electron distribution functions. It is used to describe many aspects of fusion plasmas, in particular magnetic waves and macroscopic instabilities. There are however phenomena, that cannot be treated within the fluid picture.

#### 2.1.1 Derivation

Assuming high collisionality, the particles lose their individual identity and the trajectories are randomised. This requires the mean free path, which depends on the temperature ( $\lambda \propto T^2$ ), to be small compared to typical gradient scale lengths ( $L_{\parallel, \perp}$ ). Generally hot tokamak plasmas are not dense enough to justify this approach, but the presence of the magnetic field imposes a strongly anisotropic character on the system: In the direction parallel to the magnetic field the mean free path is long while the gradients are small resulting in a long gradient scale length ( $\lambda \ll L_{\parallel}$ ), whereas the perpendicular direction exhibits strong gradients. The resulting short perpendicular gradient scale lengths ( $L_{\perp} \ll \lambda$ ) do not violate the fluid approximation, because the perpendicular movement of the particle is restricted to a region of the Larmor radius ( $r_L \ll L_{\perp}$ ) as it is gyrating along the field line. Thus a fluid like behaviour can be assumed. Reflecting this, the first two velocity moments of the ion and electron distribution function are taken. The temporal evolution of each moment depends on the succeeding one in the “hierarchy” of moments, so the system

has to be closed. This can be done by assuming the pressure to behave adiabatically. One obtains an equation system describing the dynamics of an ensemble of charged liquids.

Further approximations are made:

1. The displacement current is neglected in Amperè's Law:

$$\underbrace{\frac{1}{c^2} \frac{\partial \mathbf{E}}{\partial t}}_{\omega/c^2 \mathbf{E} \approx 0} + \mu_0 \mathbf{J} = \nabla \times \mathbf{B} \quad (2.1)$$

This excludes high frequency phenomena from the system. It constitutes a sensible restriction because the transit time of a light wave through the physical domain is small compared to the timescales of interest.

2. Since the electron mass is much smaller than the ion mass it is neglected and the mass distribution is set by the ion mass and density. Electrons therefore have no inertia and equilibrate instantly.
3. The velocities of the ion and the electron fluid are assumed to be of the same order.
4. The pressure force is assumed to be much smaller than the Lorentz force.
5. Since even a slight separation of the ion and the electron fluid would give rise to a large repulsive electrostatic force, the charges are assumed to be equally distributed. The consideration is related to assumption 1, since this will cause the current in Eq. 2.1 to be divergence free. Therefore the continuity equation

$$\frac{\partial}{\partial t} \rho_{charge} + \nabla \cdot \mathbf{J} = 0 \quad (2.2)$$

prohibits the accumulation of a space charge. This concept is referred to as “quasineutrality”, it holds for low frequencies and macroscopic spatial scales.

Within one-fluid MHD, the mass density is represented by the scalar  $\rho$ , the plasma velocity is given by the vector field  $\mathbf{v}$  ( $\approx \mathbf{v}_{ions}$ ). Although there is just one fluid, a current density  $\mathbf{J}$  is accounted for. Thus the first moment yields the mass continuity equation, whereas the second moments of ion and electron distribution functions yield the force balance equations, and — introducing a macroscopic resistivity to account for the collision term and regarding assumptions 2 and 3 — Ohm's Law.

The resulting system is supplemented by the adiabatic closure and the Maxwell equations, neglecting the displacement current. It describes the behaviour of a neutral conducting fluid immersed in a magnetic field, hence it is called MHD (MagnetohydroDynamics). It applies to many phenomena encountered in a magnetised plasma. Obviously kinetic effects like the “bootstrap” current (see Sect. 2.2.3) cannot be described by this system.

### 2.1.2 One Fluid Resistive MHD Equations

moment equations:

$$\text{Mass continuity} \quad \frac{\partial}{\partial t} \rho + \nabla \cdot \rho \mathbf{v} = 0 \quad (2.3)$$

$$\text{Momentum Balance} \quad \rho \left( \frac{\partial}{\partial t} + \mathbf{v} \cdot \nabla \right) \mathbf{v} + \nabla p - \mathbf{J} \times \mathbf{B} = 0 \quad (2.4)$$

$$\text{Ohm's Law} \quad \mathbf{E} + \mathbf{v} \times \mathbf{B} - \eta \mathbf{J} = 0 \quad (2.5)$$

adiabatic closure:

$$\text{Adiabatic equation of state} \quad \rho k \left( \frac{\partial}{\partial t} T + \mathbf{v} \cdot \nabla T \right) - (1 - \gamma) p \nabla \cdot \mathbf{v} = 0 \quad (2.6)$$

Maxwell's equations:

$$\text{Amperè's Law} \quad \mu_0 \mathbf{J} = \nabla \times \mathbf{B} \quad (2.7)$$

$$\text{Faraday's Law} \quad -\frac{\partial}{\partial t} \mathbf{B} = \nabla \times \mathbf{E} \quad (2.8)$$

Where  $p$  represents the plasma pressure,  $\gamma$  is the adiabatic coefficient,  $\mathbf{E}$  and  $\mathbf{B}$  denote the electric and the magnetic field, respectively.  $\eta$  is the resistivity of the plasma,  $k$  denotes the Boltzmann constant, and  $T$  is the Temperature ( $p = \rho k T$ ). Details on the derivation of this system can be found in many plasma physics textbooks, e.g. [7].

### 2.1.3 Timescales of MHD

Although light waves were excluded from the system, there can be waves in the plasma. If a fluid element is moved away from its equilibrium position, there is a repelling force. This gives rise to two types of waves [8]:

“**Compressional**” Alfvén waves arise from compression and rarefaction of the magnetic field lines. The disturbance does not bend the equilibrium field ( $\tilde{\mathbf{B}} \parallel \mathbf{B}_0$ ). The resulting wave is longitudinal ( $\mathbf{v}_1 \parallel \mathbf{k} \perp \mathbf{B}_0$ ). It is related to the acoustic wave in an ideal gas propagating with the sound speed:

$$v_{sound}^2 = \frac{\gamma p_0}{\rho} \quad (2.9)$$

Unlike there, the acting force (see Eq. 2.4) is not only pressure but also magnetic. The resulting magnetosonic speed is given by

$$v_{magnetosonic}^2 = v_{sound}^2 + v_A^2 \quad (2.10)$$

Where  $v_A$  represents the speed of a purely magnetical wave, the so called “Alfvén” speed:

$$v_A = \frac{B_0}{\sqrt{\mu_0 \rho_0}} \quad (2.11)$$

The ratio of thermal to magnetic energy, described by the parameter  $\beta$  evaluates to:

$$\beta = \frac{\langle p \rangle}{B^2/2\mu_0} \quad (2.12)$$

Under usual tokamak conditions it is much smaller than unity. Consequently the magnetic contribution determines the characteristics of Alfvén waves in tokamaks.

“**Torsional**” Alfvén waves are transverse ( $\mathbf{v}_1 \perp \mathbf{k} \parallel \mathbf{B}_0$ ). They propagate along the equilibrium field lines and are comparable to the wave running along a string under tension. Their dynamics is based on the tension of the magnetic field line counteracting curvature. There is no compression necessary for this kind of wave, consequently there is no analogue in the ideal gas. They also travel with the Alfvén velocity.

With  $a$  representing the typical length scale of the tokamak (e.g. the minor radius), the **Alfvén time** is defined as the interval necessary for such a wave to propagate through the domain of the plasma. It defines the fastest timescale on which MHD effects can penetrate the system. Standard parameters yield a  $\tau_A$  of some  $\mu s$ .

$$\tau_A = \frac{a}{v_A} \quad (2.13)$$

## 2.1.4 Resistivity and Flux Conservation

If the resistivity is negligible ( $\eta \approx 0$ ) one speaks of “ideal MHD”. An important consequence of this limit is that the plasma fluid is “frozen” to the magnetic field lines. This implies that there can be no change in topology without resistivity.

Only when resistivity is accounted for, the magnetic field can change independently of the fluid velocity as can be seen in the following: Taking the curl, the equations 2.5, 2.7, 2.8, and  $\mathbf{v} = 0$  combine to yield:

$$\Delta \mathbf{B} = \frac{\mu_0}{\eta} \frac{\partial \mathbf{B}}{\partial t} \quad (2.14)$$

This has the form of a diffusion equation with the diffusion coefficient  $D_{mag} = \eta/\mu_0$ . The diffusion time over a characteristic length like the plasma radius is determining the **resistive time**

$$\tau_R = \frac{\mu_0 a^2}{\eta} \quad (2.15)$$

For realistic parameters this timescale is in the order of seconds and might even exceed the duration of the discharge. However the formation of an island for example (see Sect. 3.2.1) requires reconnection of the field lines only within a very narrow region (resistive layer) of approximately 1 cm. Therefore the instability can grow within milliseconds which is still much slower, than the Alfvén time but relevant for the experiment.

## 2.2 Equilibrium

### 2.2.1 From Force Balance to Toroidicity

If the plasma is in static equilibrium, there has to be an internal balance between the pressure and the forces due to the magnetic field. Equation 2.4 yields:

$$\nabla p = \mathbf{J} \times \mathbf{B} \quad (2.16)$$

A simple realisation of this force balance is the “z pinch”. In this arrangement there is an electric voltage applied to the ends of a plasma column. The resulting current ( $j_z$ ) flowing through the plasma generates a cylindrical magnetic field ( $B_\theta$ ) that counteracts the internal pressure.

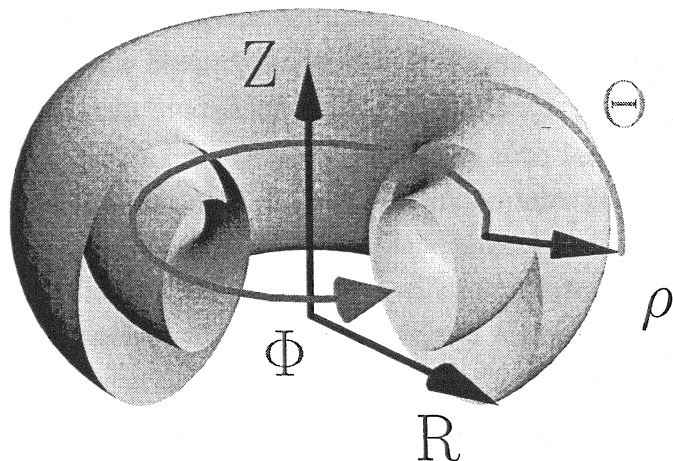


Figure 2.1: The cylindrical coordinates consist of the axial coordinate  $Z$ , the major radius  $R$  and the toroidal angle  $\Phi$ . The toroidal coordinate system is formed by the minor radius  $\rho$ , the poloidal angle  $\Theta$  and the toroidal angle  $\Phi$ .

This arrangement proves to be unstable to contraction. Due to the “frozen flux” theorem that has been described in Sect. 2.1.4, a contraction (reducing the area while the magnetic flux is kept fixed) increases the magnetic field and thus enhances the instability. Superposing an axial field ( $B_z$ ) improves the stability since it opposes a deformation of its field lines and thus provides a repelling force. For this arrangement, the addition of the axial and the cylindrical field lines yield a twisted structure reflected in its name: “screw pinch”.

None of the presented arrangements is a full equilibrium since the force balance is always violated at the ends. The solution to this problem is to bend the axial field in such a way, that the two ends join up with each other and the plasma forms a torus. Fig. 2.1 presents the coordinate systems used in this geometry.

By virtue of the periodicity in the poloidal and toroidal directions any field ( $X$ ) can be described by a Fourier decomposition into poloidal and toroidal harmonics,

$$X(\rho, \Theta, \Phi) = \sum_{m,n} X_{m,n}(\rho) e^{i(n\Phi - m\Theta)} \quad (2.17)$$

where  $m$  and  $n$  are the poloidal and toroidal mode numbers. Specifying these, the pitch angle of a helix winding around the torus is prescribed. The pair  $m/n$  is referred to as helicity.

## 2.2.2 Toroidal Equilibria

The toroidal arrangement is the topologically simplest magnetohydrodynamic equilibrium possible. It is realised in the tokamak concept which has been presented in the introduction (Fig. 1.1): the helical field consists of a toroidal component, which is generated by external coils - printed in green - and a poloidal component, caused by the toroidal current running in the plasma. This current is generated inductively by the red coil.

### Flux Functions

It follows from equation 2.16, that  $\mathbf{B} \cdot \nabla p = 0$ . Therefore the tori spanned by the magnetic field lines constitute surfaces of constant pressure. The current lines are bound to these surfaces as well because of the symmetry between current and magnetic field, displayed in the force balance. It is convenient to define the poloidal flux function  $\psi$  as the poloidal magnetic flux lying within each surface. Due to this definition  $\psi$  is a constant on the surfaces as well. It is therefore common to use the following quantity as a measure of the minor radius:

$$\rho_{pol} = \sqrt{\frac{\psi}{\psi(a)}} \quad (2.18)$$

All quantities that just depend on  $\rho_{pol}$  are called flux quantities.

### Grad-Shafranov Equation

Assuming toroidal symmetry it is possible to describe the force balance of this arrangement with a differential equation, the Grad-Shafranov-Equation [7]:

$$R \frac{\partial}{\partial R} \frac{1}{R} \frac{\partial \psi}{\partial R} + \frac{\partial^2 \psi}{\partial z^2} = \mu_0 R^2 p'(\psi) - \mu_0^2 f(\psi) f'(\psi) \quad (2.19)$$

with  $f = RB_\phi/\mu_0$  and  $\dots' = \nabla_\psi \dots$ . Solving this either with an ordering ansatz, or numerically it is found, that inner surfaces are shifted to higher radii for high pressure equilibria, an effect attributed to the magnetic “loop” force, which is trying to straighten the equilibrium field lines. This shift is known as the “Shafranov shift”.

For the following examinations the HELENA code [9] has been used to derive numerical solutions of this equation. The solutions account for the Shafranov shift and non-circular shaping. Apart from the MHD assumptions toroidal symmetry, appropriate boundary conditions and a static equilibrium are the only approximations made.

### The Safety Factor, Magnetic Shear and $\beta_{pol}$

As mentioned before the magnetic field lines lie within the flux surfaces and wind around the torus helically. The pitch of this helix depends on the ratio between the poloidal and toroidal magnetic fields.

Depending on the average pitch, the field line either spans the whole flux surface (2D) or runs back into itself (1D). The later case is referred to as a “resonant” field line. Since a perturbation of the equilibrium will propagate along the field lines as an Alfvén wave, a resonant surface will permit the formation of a standing wave, obviously an especially crucial condition considering stability.

Since the pitch is of such an importance to stability the “safety factor” is defined as the toroidal interval the field line has to span, to wind around the torus in poloidal direction once.

$$q = \frac{\Delta\Phi}{2\pi} \quad (2.20)$$

Taking into account the equation of the field line

$$\frac{R d\Phi}{dl} = \frac{B_\Phi}{B_\Theta} \quad (2.21)$$

the safety factor  $q$  is given by the average ratio of the magnetic fields along the field line.

$$q = \frac{1}{2\pi} \oint \frac{1}{R} \frac{B_\Phi}{B_\Theta} dl \quad (2.22)$$

A resonant field line is associated with a rational value of  $q$ . Since the safety factor is a flux surface quantity one refers to surfaces with resonant field lines as “rational” or “resonant” surfaces. The magnetic shear is defined as [10]:

$$s = \frac{\psi}{q} \frac{dq}{d\psi} \quad (2.23)$$

An equilibrium can be further characterised with the parameter  $\beta_{pol}$ :

$$\beta_{pol} = \frac{\int p dS / \int dS}{I^2 \mu_0 / l^2} \quad (2.24)$$

where the  $\int dS$  is the poloidal cross section,  $I$  denotes the toroidal plasma current and  $l$  is the poloidal perimeter of the plasma.



### 2.2.3 Bootstrap Current

It has already been pointed out that some effects cannot be described within a fluid picture. One example is the “bootstrap” current, mentioned in the introduction. It arises from the anisotropic distribution of particles, which do not stick to the flux surfaces but follow more complicated trajectories through the tokamak’s inhomogeneous fields. Fig. 2.2 presents the path of such a particle, which has been followed around the torus with the HAGIS code [11, 12] (I) and a sketch of the projection of two such “banana” orbits (their shape accounts for the name) onto the poloidal plane (II). Instead of simply gyrating along the field line the particle is periodically reflected as it tries to follow the field line to the inner domain of the tokamak.

The reason for this reflection is that the toroidal field falls off radially ( $B_\Phi \propto 1/R$ ) and is higher on the inside (therefore called: high field side - HFS), than on the outside (low field side - LFS). Since the magnetic moment ( $\mu = mv_\perp^2/2B$ ) is conserved  $v_\perp$  has to increase as the particle is moving inward. Because the total kinetic energy is conserved,  $v_\parallel$  decreases and if the initial parallel motion was too slow, it will come to a standstill before the HFS is reached. Thus “trapped particles” are reflected in the “mirror” formed by the magnetic field.

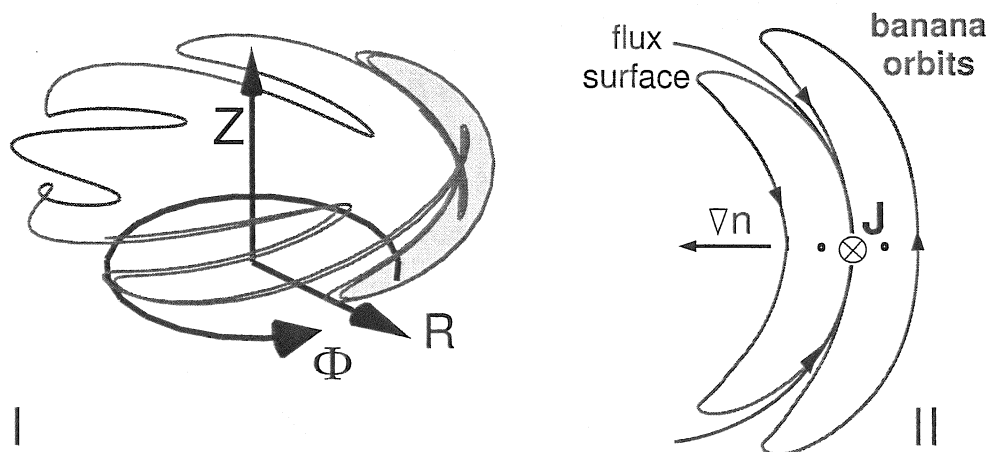


Figure 2.2: High energy particles do not stick to the fluid and follow more complicated trajectories through the tokamak field. I plots an exemplary trajectory of a particle moving around the torus, It has been calculated with the code HAGIS [11] [12]. II shows the projection of the trajectory upon the poloidal plane. Due to their shape, they are called banana orbits.

With  $B_{max/min}$  denoting the maximum/minimum magnetic field along a field line, the condition for a particle to escape this trap and become “passing” is:

$$\left(\frac{v_{\parallel}|_{\Theta=0}}{v_{\perp}|_{\Theta=0}}\right)^2 > \frac{B_{max} - B_{min}}{B_{min}} \quad (2.25)$$

Electrons and ions move in different directions. Due to the opposite charge the currents associated with the trapped electron and ion motion along the banana are parallel. In the presence of a density gradient (indicated in Fig. 2.2-11) there are more particles on the inner than on the outer banana. Thus the current pointing downward on the outer orbit cannot compensate the opposite current on the inner one. The resulting net-current is called the “banana current”.

Though the mechanism has been explained in the poloidal projection, the current is mainly toroidal, as the particle orbits follow the helical field lines ( $B_{\Theta} < B_{\Phi}$ ). (As stated before they are really deflected from the field line and the associated flux surface by drift motions, which accounts for the finite width of the banana orbits.) The banana current has been marked in Fig. 2.2-11; it associates to an asymmetric redistribution of the parallel velocity of electrons and ions in the domain of trapped particles (set by 2.25) as can be seen in Fig. 2.3-1. Because passing particles are not affected by the outlined mechanism, there are steep transitions appearing in the distribution function. At these points, particle-particle interactions will wipe out the steps for each species as shown for both electrons and ions in Fig. 2.3-11. The two resulting distribution functions are shifted against each other. This gives rise to a current in the parallel direction, larger than the original banana current, that is called the “bootstrap current”. Because the banana current is proportional to the density gradient and the average thermal velocity, the current density depends on the pressure gradient. A simplified formula is found in [6]:

$$j_B = \frac{c \epsilon^{3/2}}{B_p} T \frac{dn}{dr} \quad (2.26)$$

With  $\epsilon = r/R_0$  denoting the ratio of minor over major radius. The tokamak concept requires a toroidal current, to form the poloidal magnetic field. Conventionally this current is supplied by an external coil, as described in Sect. 2.2.2. The intrinsic bootstrap current is a welcome contribution, which is indicated by the name. The term “bootstrap”<sup>1</sup> is used to describe a situation where one gets something out of

<sup>1</sup>This goes back to the Baron von Münchhausen, who claimed, that he could “pull himself up by his bootstraps”.

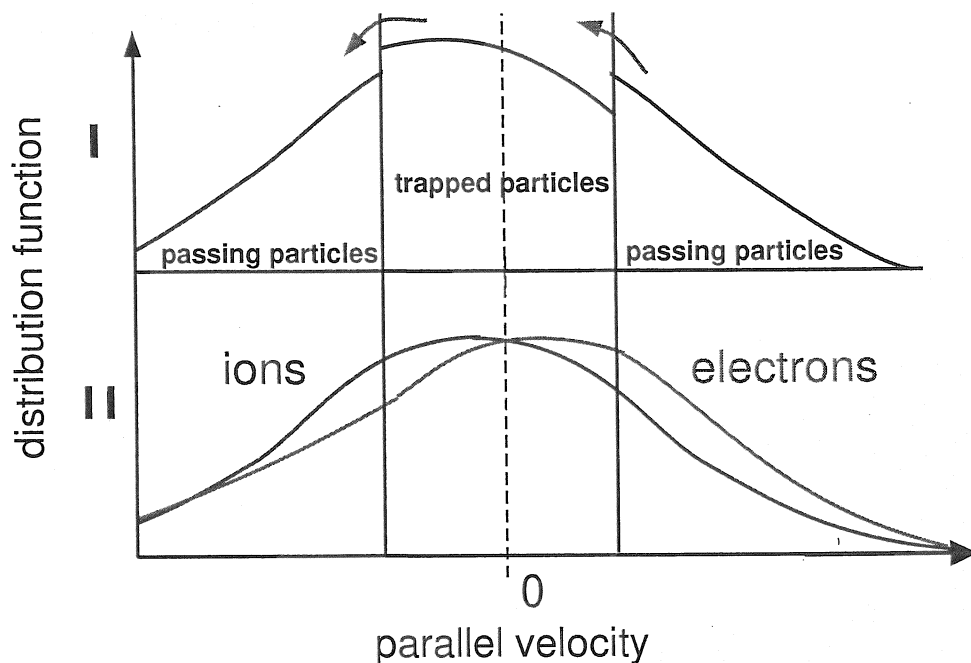


Figure 2.3: The distribution functions for ions and electrons exhibit step transitions in the distribution functions due to the banana current (I). Collisions wipe out the sharp transitions and cause the bootstrap current (II). [6]

nothing (compare the starting procedure of a computer, where the term “boot” is a contraction of bootstrap). The utilisation of this current is the basic idea of the “advanced scenarios” will be presented in more detail in Sect. 3.1.4.

## 2.3 Stability

### 2.3.1 Static Linear MHD

Linear stability analysis asks for the equilibrium’s reaction to an infinitesimal deviation from the force balance (the displacement  $\xi$ ), to see whether a repelling force counteracts this perturbation, or an instability is evoked. The common linearisation procedure is applied to MHD in many textbooks (e.g. [7]), all quantities are split into an equilibrium part and a perturbation:

$$\begin{aligned} \mathbf{X} &= \{\rho, p, T, \mathbf{v}, \xi, \mathbf{B}\} \\ \mathbf{X} &= \mathbf{X}_0 + \mathbf{X}_1 \end{aligned} \tag{2.27}$$

Since a static equilibrium is treated the velocity just consists of a perturbed part  $v = \tilde{v} = v_1 = \dot{\xi}_r$ . An harmonic ansatz is opportune:

$$f(\mathbf{x}, t) = f(\mathbf{x})e^{+\lambda t}, f = (\rho_1, P_1, \mathbf{B}_1, \mathbf{v}_1, \xi_1) \quad (2.28)$$

There is no initial displacement (i.e. the response of the equilibrium to an initial velocity perturbation is examined). Still, for small times the velocity profile can be interpreted as the spatial perturbation as well.

$$\tilde{v}_\rho \propto \dot{\xi}_\rho \propto \xi_\rho \text{Im}(\lambda) \quad (2.29)$$

The ansatz 2.28 is inserted into the the MHD equations (2.3 to 2.5). When dealing with the onset of the instability one assumes the perturbations to be small compared to the equilibrium quantities. Therefore terms of higher order in the perturbation are neglected. This yields the linearised equations. In a physical sense it means that there is no feedback of the evolving instability on the equilibrium. Therefore linear theory is not able to access the full dynamics of a completely evolved instability or to yield an amplitude of the perturbation.

static linearised MHD equation set:

$$\lambda \rho_1 = -\nabla \cdot (\rho_0 \mathbf{v}_1) \quad (2.30)$$

$$\lambda \rho_0 \mathbf{v}_1 = -k \nabla (\rho_0 T_1 + \rho_1 T_0) + \frac{1}{\mu_0} (\nabla \times \mathbf{B}_0) \times \mathbf{B}_1 + \frac{1}{\mu_0} (\nabla \times \mathbf{B}_1) \times \mathbf{B}_0 \quad (2.31)$$

$$\lambda \rho_0 T_1 = -\rho_0 \mathbf{v}_1 \nabla T_0 + (1 - \gamma) \rho_0 T_0 \nabla \mathbf{v}_1 \quad (2.32)$$

$$\lambda \mathbf{B}_1 = -\nabla \times \mathbf{B}_0 \times \mathbf{v}_1 - \nabla \times \eta \nabla \times \mathbf{B}_1 \quad (2.33)$$

The system of equations corresponds to a matrix equation in the following form.

$$L \mathbf{U} = \lambda R \mathbf{U} \quad (2.34)$$

with  $L$  and  $R$  being matrix operators,  $\lambda$  being an eigenvalue.  $\mathbf{U} = \{n_1, \mathbf{v}_1, T_1, \mathbf{B}_1\}$  represents the perturbed quantities.  $\mathbf{U}$  does not contain the displacement  $\xi$ , but:

$$\partial_t \mathbf{v}_1 = \partial_t^2 \xi \quad (2.35)$$

So the linearised momentum balance (Eq. 2.31) can be written as

$$n_0 \partial_t^2 \xi = -\nabla (n_0 T_1 + n_1 T_0) + (\nabla \times \mathbf{B}_0) \times \mathbf{B}_1 + (\nabla \times \mathbf{B}_1) \times \mathbf{B}_0 \quad (2.36)$$

The RHS of this equation is the linearised force operator  $F$ . It still contains the perturbed magnetic field. Due to the frozen flux theorem this quantity can be ascribed to the displacement. That does not work in the resistive case.

$$n_0\lambda^2\xi = \begin{cases} F(\xi) & \text{ideal MHD} \\ F(\xi, \mathbf{B}_1) & \text{resistive MHD} \end{cases} \quad (2.37)$$

In the ideal case the force operator is Hermitian [7], consequently the solution of the eigenvalue problem yields either a real or an imaginary eigenvalue. The former indicates an oscillation around the equilibrium position and therefore stability, the later indicates the growth of an instability. If resistivity is included the eigenvalue is complex and there can be a combination of oscillation and growth.

### 2.3.2 The Energy Functional $\delta W$

Apart from the numerical solution resulting in growth rates and eigenfunctions, the force operator can be further examined to gain qualitative insight into the behaviour of the system [13]. Multiplication of Eq. 2.36 with  $\xi$  and integration over space yields

$$\frac{1}{2} \int n_0\lambda^2\xi^2 d^3x = -\frac{1}{2} \int \xi \cdot F(\xi) d^3x \equiv \delta W \quad (2.38)$$

the LHS of which represents the mode's kinetic and the RHS its potential energy. The sign of the functional  $\delta W$  determines stability: in an unstable system, there are perturbations  $\xi$ , which reduce the potential energy ( $\delta W(\xi) < 0$ ), in a stable system, any physically allowable perturbation increases it ( $\delta W(\xi) > 0$ ). The energy functional can be split into contributions for plasma, surface and vacuum [2]:

$$\delta W = \delta W_P + \delta W_S + \delta W_V \quad (2.39)$$

$$\begin{aligned} \text{with: } \delta W_P = & \frac{1}{2} \int_P dV \left( \frac{B_1^2}{2\mu_0} + \frac{B_0^2}{2\mu_0} + (\nabla \cdot \xi_\perp + 2\xi_\perp \cdot \kappa)^2 + \gamma p_0 (\nabla \cdot \xi)^2 \right. \\ & \left. - 2(\xi_\perp \cdot \nabla p_0)(\kappa \cdot \xi_\perp) - \frac{j_\parallel}{B_0} (\xi_\perp \times \mathbf{B}_0) \cdot \mathbf{B}_1 \right) \end{aligned} \quad (2.40)$$

$$\delta W_S = \int_S dS \left( (\mathbf{n} \cdot \xi)^2 \mathbf{n} \left| p_0 + \frac{B_0^2}{2\mu_0} \right| \right) \quad (2.41)$$

$$\delta W_V = \frac{1}{2} \int_V dV \frac{B_1^2}{2\mu_0} \quad (2.42)$$

where  $\kappa = \mathbf{B}_0 \cdot \nabla \mathbf{B}_0 / B_0$  is the curvature vector of the equilibrium magnetic field and  $\mathbf{n}$  is the normal displacement of the plasma surface.

- The first four terms in Eq. 2.40 are all positive and stabilising. They account for the energy expense to evoke magnetosonic waves, the next one accounts for the contribution when the equilibrium gives in to the pressure force. As it is proportional to  $(\kappa \cdot \xi_{\perp})$  it is stabilising on the high field side and destabilising on the low field side of the torus. The last term describes the destabilising influence of the current giving rise to current driven instabilities like the kink.
- The surface term (Eq. 2.41) vanishes if there is no normal displacement at the surface.
- the vacuum part (Eq. 2.42) represents the transfer of energy into the perturbed magnetic field outside the plasma

### 2.3.3 The Linear Stability Code CASTOR

The problem of linear MHD has been shown to be equivalent to the eigenvalue problem Eq. 2.34. It is solved numerically by the code CASTOR [14]. The equilibrium fields entering the force operator are read in from a numerical solution of the Grad-Shafranov-Equation calculated with HELENA (see Sect. 2.2.2).

Advantage of the toroidal symmetry is taken. All fields are represented by their Fourier harmonics (Eq. 2.17). Neglecting the changes of the equilibrium that are caused by the evolving perturbation, the toroidal symmetry is preserved in the linear picture. Therefore modes of different toroidicity do not interfere with each other and only one toroidal harmonic ( $n$ ) at a time has to be considered. Since it is impossible to solve for an infinite number of poloidal harmonics, one is limited to an interval  $m = m_1 \dots m_2$ . Therefore the disturbances take the form:

$$X(\mathbf{x}) = \sum_{m=m_1}^{m_2} X_{m,n}(\rho) e^{i(n\Phi - m\Theta) + \lambda t} \quad (2.43)$$

the radial dependence  $X_{m,n}(\rho)$  is represented by a list of discrete points.

As a result, the code returns the complex eigenvalue  $\lambda = \Gamma + i \cdot \omega$  and the radial profiles of the included harmonics of the perturbed quantities. In principle one would have to sum up the complex eigenfunctions for all harmonics and take the real part of the resulting term to determine the spatial structure of the mode.

### 2.3.4 Stability of a Rotating Plasma

Under certain experimental conditions (see chapter 4), the plasma exhibits a toroidal flow that can yield an influence on the stability of the plasma. To account for this, the linearised equations have to be supplemented by the terms containing the undisturbed velocity ( $\mathbf{v}_0$ ) [15, 16], which were taken to be zero before.

linearised MHD for flow equilibria:

$$\lambda\rho_1 = -\nabla \cdot (\rho_0\mathbf{v}_1) - \nabla \cdot (\rho_1\mathbf{v}_0) \quad (2.44)$$

$$\begin{aligned} \lambda\rho_0\mathbf{v}_1 = & -k\nabla(\rho_0T_1 + \rho_1T_0) && \text{pressure term} \\ & + \frac{1}{\mu_0}(\nabla \times \mathbf{B}_0) \times \mathbf{B}_1 && \mathbf{J} \times \mathbf{B} \text{ term} \\ & + \frac{1}{\mu_0}(\nabla \times \mathbf{B}_1) \times \mathbf{B}_0 \\ & \left. \begin{aligned} & -\rho_1(\mathbf{v}_0 \cdot \nabla)\mathbf{v}_0 \quad (\text{centrifugal force}) \\ & -\rho_0(\mathbf{v}_1 \cdot \nabla)\mathbf{v}_0 \quad (\text{coriolis force}) \\ & -\rho_0(\mathbf{v}_0 \cdot \nabla)\mathbf{v}_1 \end{aligned} \right\} && \text{inertia term} \end{aligned} \quad (2.45)$$

$$\begin{aligned} \lambda\rho_0T_1 = & -\rho_0k\mathbf{v}_1 \cdot \nabla T_0 - \rho_0k\mathbf{v}_0 \cdot \nabla T_1 - \rho_1k\mathbf{v}_0 \cdot \nabla T_0 \\ & + (1-\gamma)\rho_0kT_0\nabla\mathbf{v}_1 \\ & + (1-\gamma)\rho_0kT_1\nabla\mathbf{v}_0 + (1-\gamma)\rho_1kT_0\nabla\mathbf{v}_0 \end{aligned} \quad (2.46)$$

$$\lambda\mathbf{B}_1 = -\nabla \times \eta\nabla \times \mathbf{B}_1 - \nabla \times \mathbf{B}_0 \times \mathbf{v}_1 - \nabla \times \mathbf{B}_1 \times \mathbf{v}_0 \quad (2.47)$$

Accounting for a radially varying toroidal rotation only, the equilibrium velocity may be written in terms of the rotation frequency of the plasma and the cylindrical coordinate  $\mathbf{v}_0 = \Omega R$ . Thus the ‘‘inertia terms’’ in Eq. 2.45 can be identified as contributions to the coriolis force ( $\propto \rho\Omega$ ) and the centrifugal force ( $\propto \rho\Omega^2$ ). The other contributions are easily recognisable by comparison with the MHD equations (Eq. 2.3 to Eq. 2.8)

Toroidal rotation has been implemented into CASTOR [16]. As resistivity did before, toroidal rotation results in a complex eigenvalue, the imaginary part of which describes the rotation frequency of the mode. The calculation can either be based on static or dynamic equilibria accounting for the change of the equilibrium due to inertial forces to Eq. 2.19 [17]. The first case is limited to moderate velocities at which the rotation energy stored in the plasma is small compared to the energy of the kinetic pressure.

# Chapter 3

## Tokamak Research

### 3.1 Modes of Operation

In the history of plasma physics an improvement of the confinement has always been one object of tokamak research. The discharge parameters encountered throughout this development are generally put into four categories:

#### 3.1.1 Ohmic Plasmas

The toroidal current not only generates the magnetic field, but also provides a source of energy in a resistive plasma due to the ohmic power ( $I^2\eta$ ). Since the resistivity is dropping like  $\eta \propto T_e^{-3/2}$  the efficiency of this heating mechanism collapses at high temperatures and the plasma energy is limited [18].

#### 3.1.2 L-Mode

Higher temperatures could be accessed by auxiliary heating mechanisms like the injection of energetic neutral particle beams or of radio frequency waves. However the power deposition in the plasma affects the confinement time ( $\tau_E \propto P^{-0.5}$ ) [19] pointing to minimum requirements for ignition, which are hard to realise. This regime is called the "low confinement mode".

#### 3.1.3 H-Mode

Early tokamak plasmas were bounded by material limiters, so the hot plasma is in direct contact with a plate. Impurities are eroded and pollute the bulk plasma. To



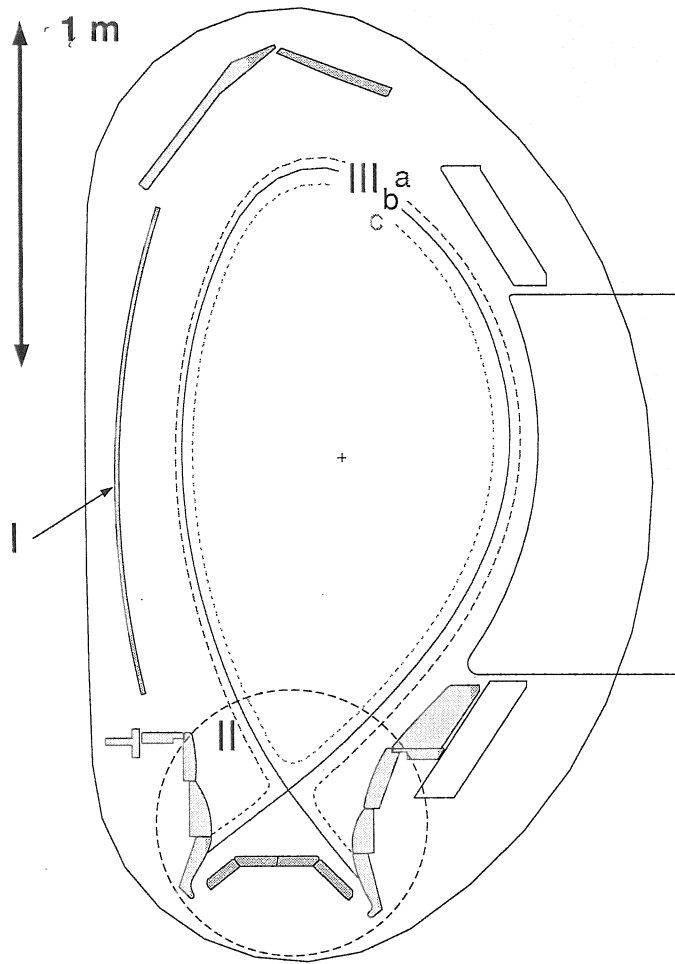


Figure 3.1: The poloidal cross section of ASDEX Upgrade. The limiter (I) and the divertor plates (II) are visible. For diverted discharges, the flux topology (III) of vacuum (a) and plasma (c) domain are separated by the separatrix (b).

avoid this the divertor, a special field geometry separating plasma and vacuum has been developed.

An example for a limiter and an divertor can be seen in the poloidal cross section of ASDEX Upgrade (Fig. 3.1), a mid sized tokamak sited in Garching, Germany. In the plasma domain (III c) the field consists of the usual nested tori, whereas the field lines in the vacuum region (III a) are redirected against special target plates (II). Thus the inevitable sputtering process does not happen in the vicinity of the plasma as in limited cases, but in a region, specially designed to prevent recycling. Particles in the vacuum regions will follow the field line to the divertor plates. ASDEX Upgrade can be operated with a limiter (I) as well.

The exploration of these edge geometries has already been one of the scientific objectives of the present machine's predecessor, ASDEX (Axial Symmetric Divertor

EXperiment). It has been there, where a new operation mode, offering a higher confinement (therefore called “H-mode”) has been found [20]. The divertor helps to sustain high edge gradients and an improved confinement, however H-modes have been found in limited plasmas as well [21].

### 3.1.4 Advanced Mode

One of the biggest problems of the tokamak concept is arising from the inductive current drive, which limits the duration of the discharge. Being limited to pulsed operation constitutes a huge restriction with respect to a power producing reactor as a power plant should run continuously. Alternative ways to drive the plasma current,  $I_P$ , e.g. the injection of a neutral particle beam (NBI) are generally so ineffective that they can only assist, but not replace the main current drive. The bootstrap current described in Sect. 2.2.3 is not depending on an outer drive and thus presents a solution to this problem. If the equilibrium can be optimised in such a way that the bootstrap effect is providing most of the current, slight corrections of the current profile could be realised by ECRH (Electron Cyclotron Radiative Heating).

An equilibrium, optimised for a high bootstrap fraction  $I_B/I_P$  will look different from a conventional one, as can be seen in Fig. 3.2: Being pressure gradient driven, the bootstrap current is peaking off axis, which directly associates to a changed current profile. As the current generates the poloidal field, the peak in the current density is associated with a minimum in the safety factor (compare Eq. 2.22). A falling safety factor is associated with a negative shear (Eq. 2.23), therefore these  $q$  profiles are characterised as reversed shear, the minimum region is referred to as low shear region.

Low and reversed shear gains access to the second stable region of ballooning stability (see Sect. 3.2.4) stabilising high toroidal mode numbers ( $n \rightarrow \infty$ ) [22] and suppresses turbulent transport [23, 24, 25, 26]. Thus an “internal transport barrier” (ITB) is established which permits the sustainment of very high pressure gradients. These yield a high bootstrap current (Eq. 2.26) giving rise to a positive feedback between the current and the pressure profile. Establishing this however relies on high pressure equilibria with a high value of  $\beta_{pol}$  (Eq. 2.24). The special magnetic structure and the high pressure account for a range of MHD activities making the realisation of this feedback an ambitious goal.

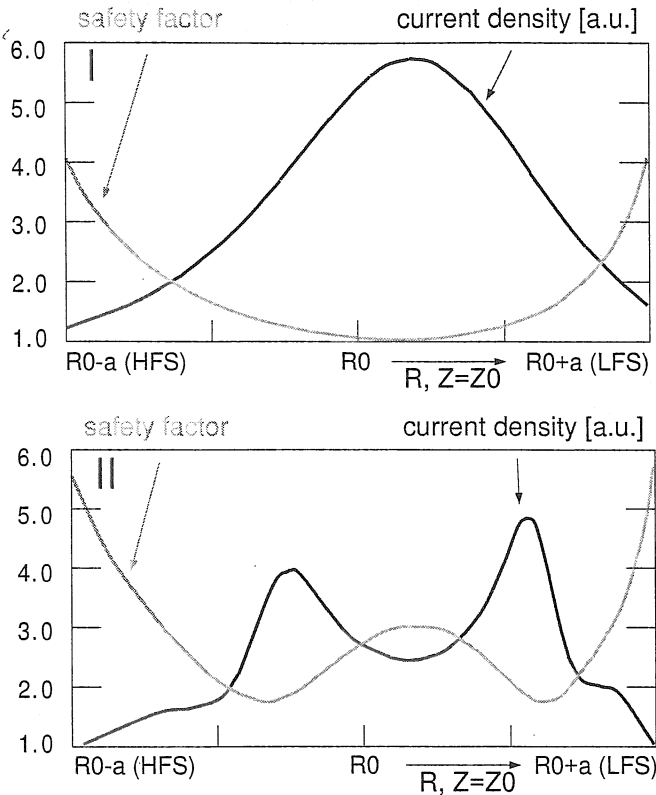


Figure 3.2: Safety factor and current density for a conventional (I) and a reversed shear equilibrium (II) are plotted along the mid-plane ( $Z = Z_0$ ,  $R_0 - a < R < R_0 + a$ ) of the torus, where  $a$  denotes the minor radius.

The beneficial aspects of negative shear with respect to ideal and resistive MHD stability have been long known [27, 28, 29]. While theoretical considerations of the matter reach back to the sixties [30], advanced scenarios have been picked up as a subject of experimental research just throughout the last decade. These studies are motivated by the possibility of a steady state tokamak, which is enabled by access to a higher plasma pressure and by the reduction in size and cost of future machines, whether they are designed for further research or power production [31].

There are several ways to generate the hollow current profile exhibited by Fig. 3.2-II. Most common is the method of early heating [32]: As the discharge is starting the inductively driven current does penetrate the cold plasma from the outside. Since the process is depending on resistivity and therefore temperature (compare Eq. 2.14) the current diffuses inward quickly resulting in conventional profiles (Fig.

3.2-1). This can be prevented by early heating the plasma core (e.g. NBI) causing a central hole in the current profile. Since the diffusion is thus just slowed, the reversed shear is a transient feature, which is lost as the current diffuses inward. Once the plasma current was fed off axis (ideally by a high bootstrap fraction) a steady state can be achieved.

Reversed shear scenarios have been observed on many major tokamak experiments: on the "Joined European Torus" (JET) at Culham, U.K. [33], the "Tokamak fusion test reactor" (TFTR) at Princeton, U.S. [34], D-IIID at San Diego, U.S. [10] and JT-60 Upgrade at Naka, Japan [35] as well, as at ASDEX Upgrade in Garching, Germany [36] and TEXTOR-94 in Juelich, Germany [37].

## 3.2 MHD Instabilities

### 3.2.1 Tearing Modes (TM)

The Tearing Mode (TM) instability is driven by the radial gradient of the toroidal current density. During its growth, the equilibrium field lines "tear" and rejoin forming islands. This process has inspired the name.

The formation of the island constitutes a change in topology, as shown in Fig. 3.3, which projects the magnetic field minus the equilibrium magnetic field at the

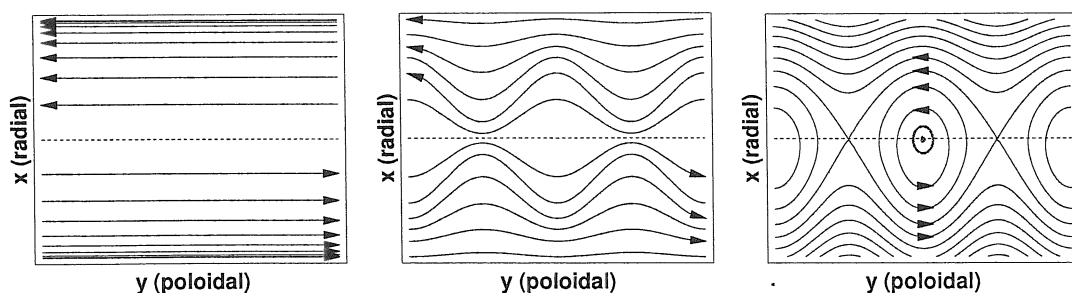


Figure 3.3: All three graphs show the projection of  $\mathbf{B}^* = \mathbf{B} - \mathbf{B}_0|_{r_s}$  upon the poloidal plane. The abscissa represents the poloidal angle and the ordinate is running in radial direction focusing on an interval around the rational surface, which is indicated by a dotted line. The first graph shows the equilibrium structure, the second an ideal perturbation. The third graph exhibits the magnetic island, formed by the TM after reconnection has been taking place around the rational surface.

rational surface ( $\mathbf{B}^* = \mathbf{B} - \mathbf{B}_0|_{r_s}$ ) upon a part of the poloidal cross section. This is equivalent to the topology seen when viewing along the resonant field line.

In the left picture the equilibrium is sketched. Due to its definition  $\mathbf{B}^*$  vanishes at the rational surface. The shear evokes a poloidal field contribution growing stronger as the resonant surface is left behind. The poloidal field will change directions as the resonant surface is passed. The central picture shows the change arising from a resonant disturbance. So far complying with ideal MHD there is no change in the topology. As resistivity is considered in a narrow domain around the rational surface the field lines can break up and rejoin forming islands, as shown in the right picture. While the instability is growing, there is a perturbed current flowing within the resistive layer in direction of the resonant field lines.

The islands are emerging on a local resistive diffusion time. Since the timescale of ideal MHD,  $\tau_A$ , is much smaller (see Sect. 2.1.3) the intermediate ideal plasma is going to adapt to the disturbance attuning to a changed equilibrium state. The current gradient around the rational surface does change, in the case of an unstable mode feeding energy into the resistive layer.

### Linear Theory

The mode has been discovered in a linear analysis of a pinch equilibrium [38]. The idea of this approach is to separate the plasma into a layer around the rational surface that has to be treated with resistive MHD and the remaining, ideal region.

For a large aspect ratio tokamak, the MHD force equation yields [39] the so called "tearing mode equation":

$$\frac{1}{r} \frac{d}{dr} r \frac{d\psi}{dr} - \frac{m^2}{r^2} \psi - \frac{m \nabla_r j_\Phi}{B_\Theta (m - nq)} \psi = 0 \quad (3.1)$$

This differential equation determines the profile of the perturbed flux in the region outside the resistive layer. Using appropriate boundary conditions it can be calculated from the core and the edge of the plasma independently up to the resonant surface. Being the solutions of a linear equation, it is possible to match the amplitudes of the both branches. The perturbed current is visible as a kink in the

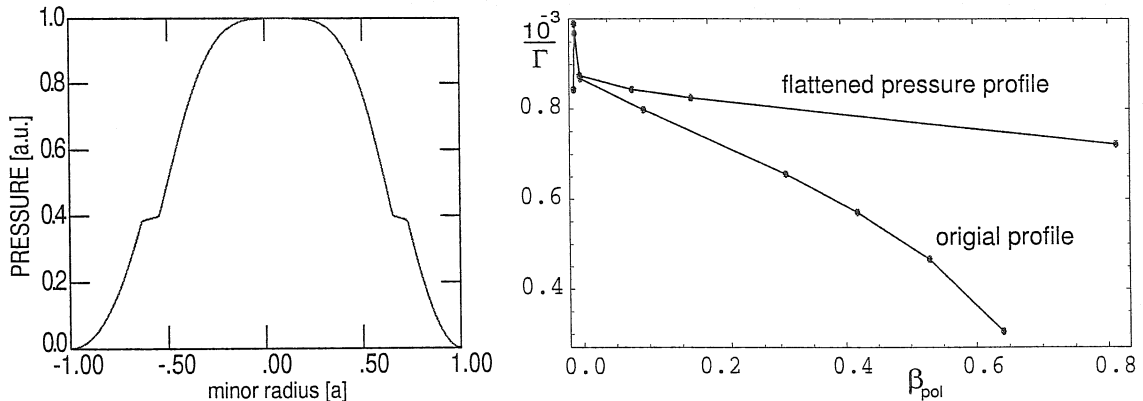


Figure 3.4: The reaction of a global change in plasma pressure of two TM unstable Equilibria was analysed with CASTOR. The difference of the two equilibria is, that in one case the pressure profile is locally flattened in a narrow region around the rational surface. The resulting growth rates are plotted (normalised to the Alfvén time) against  $\beta_{pol}$  yielding a measure for the pressure.

resulting total profile. To characterise this, the parameter  $\Delta'$  is defined as

$$\Delta' = \frac{\lim_{\delta \rightarrow 0} \psi'(r)|_{r=rs+\delta} - \lim_{\delta \rightarrow 0} \psi'(r)|_{r=rs-\delta}}{\psi(rs)} \quad (3.2)$$

with  $\delta$  denoting the width of the resistive layer and  $rs$  being the location of the rational surface. This parameter is a stability criterion for the TM growth.  $\Delta' < 0$  is associated with stability, instability occurs for  $\Delta' > 0$ .

### The Glasser Effect

Initially the analytical models were based on ordering assumptions like a small pressure. Extending them to finite pressure [40] and applying it to tokamak geometry [41] it is found that finite pressure yields a stabilising influence on the TM growth. This is caused by an interaction with the pressure dependent Pfirsch Schlüter current, which is oriented parallel to the magnetic field.

$$J_{PS} \propto \frac{1}{B_\Theta} \frac{r}{R} \frac{dp}{dr} \quad (3.3)$$

Fig. 3.4 presents a calculation illustrating the effect on the TM growth. The reaction of a global change in plasma pressure of two TM unstable equilibria was analysed with CASTOR. In one case the pressure profile has been flattened around the location of the TM as shown in the picture. It can be clearly seen from the scan that the

decrease of the growth rate is due to the local pressure gradient at the position of the mode. Because a disappearing pressure gradient gave rise to numerical problems (accounting for the spikes in the right graph) the pressure gradient was not reduced to zero in the flattened region, so the upper curve does also decrease somewhat. The stabilising mechanism is called "Glasser Effect". Owing to this effect most high pressure tokamak equilibria are stable against classical tearing modes.

### Tearing modes affect the confinement

As the fluid motion is bound to the flux topology, the nested surfaces provide the thermal insulation of the plasma. Since the island structure short circuits two different radial positions the mode deteriorates the confinement.

If two modes of different helicity reside so close to each other that their islands overlap, the consequence is an ergodisation of the field. So far the field lines were resonant covering one dimension or rational spanning surfaces (2D) since even an evolved island preserves discrete flux surfaces. But in the overlapping region, the field lines loose this restriction moving freely in space. If major parts of the plasma are ergodised the equilibrium is destroyed and the plasma disrupts [42].

If a single island exceeds a certain size the pressure profile will be flattened locally because of the transport of particles and energy parallel to the field. One important result is the rise of neoclassical TM.

### Neoclassical Tearing modes (NTM)

The neoclassical bootstrap current has been presented in Sect. 2.2.3 as a helical current being caused by the pressure gradient. If the pressure profile is now flattened inside the island, the result will be a local "hole" in the bootstrap current which is equivalent to a disturbed current in the opposite direction. Running in helical direction this current interacts with the island current in such a way that the TM is destabilised by high pressure and the associated bootstrap current in positive shear [43] and stabilised for a falling safety factor [44]. It should be noted that the calculation with the flattened profile (Fig. 3.4) has nothing to do with neoclassical effects. The NTM is based on nonlinear physics not accessible to the linear code CASTOR.

### 3.2.2 Coupling and Double Tearing Modes (DTM)

The matching procedure outlined above can be extended to deal with multiple TMs at different locations in the plasma. This was first done in a cylindrical [45], later also in toroidal geometry [46]. As the ideal plasma is split by resistive layers several times the matching conditions take the form of a matrix equation.

The formalism can also be applied to an instability of importance in advanced scenarios, the DTM shown in Fig. 3.5. Due to the nonmonotonic safety factor (C) rational surfaces (e.g.  $q = 2$ ) can appear at two radial positions ( $rs_1 < rs_2$ ). This enables two TM to grow. Owing to the equilibrium structure the islands in the falling  $q$  region have a different orientation than the ones in rising  $q$ . Therefore the disturbed currents in the topology sketch (B) are oriented differently for the two island chains. Since both islands have the same helicity they yield a strong mutual influence on each other that destabilises the mode. In Fig. 3.5-A, a snapshot of a nonlinear evolution, taken from a cylinder code [47] has been projected onto the poloidal plane. The contours represent  $B^*$  and the colour the temperature topology which is changed by transport.

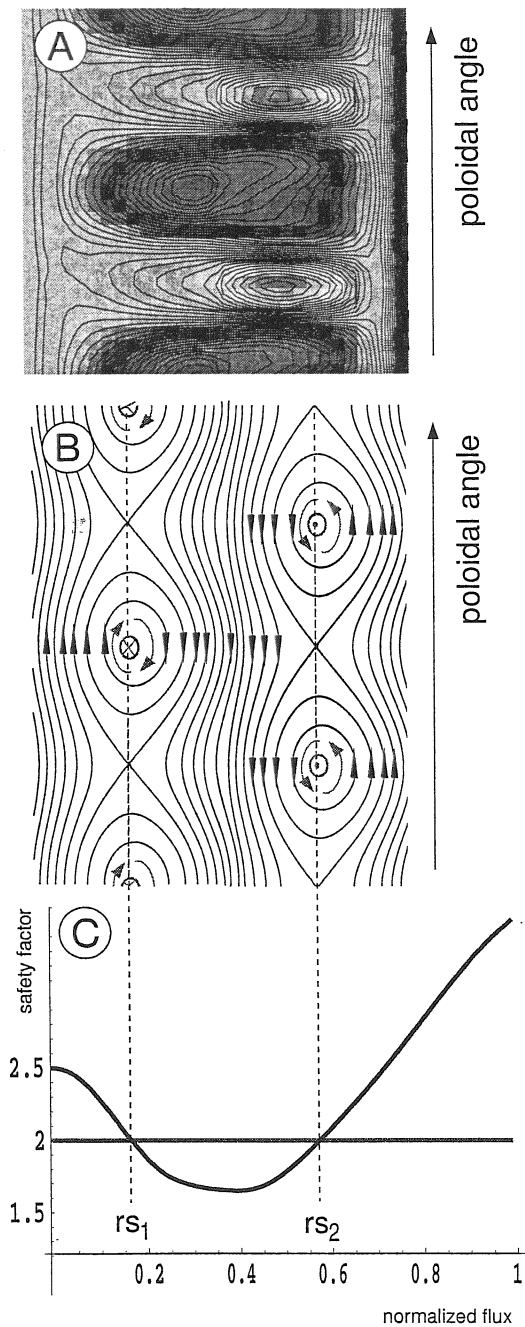


Figure 3.5: Reversed shear  $q$  profile (C) give rise to the growth of two neighbouring TM of the same helicity (B). (A) presents a nonlinear cylinder calculation.



The magnetic flux perturbation is determined by the “tearing mode equation” (Eq. 3.1) also for coupled TM. It can be expressed as [48]:

$$\tilde{\psi} = \tilde{\psi}_1 + \tilde{\psi}_2 \quad (3.4)$$

while  $\tilde{\psi}_1$  is vanishing at the plasma centre and at the outer rational surface ( $\tilde{\psi}_1(rs_2) = \tilde{\psi}_1(0) = 0$ ),  $\tilde{\psi}_2$  is vanishing at the first rational surface and at the plasma edge ( $\tilde{\psi}_2(rs_1) = \tilde{\psi}_2(b) = 0$ ). Now the matching procedure is extended and each part,  $j$ , yields a  $\Delta'$  condition on each rational surface,  $i$  [48]:

$$\Delta'_{ij} = \frac{\lim_{\delta \rightarrow 0} \psi'_j(r) \Big|_{r=rs_i-\delta}^{r=rs_i+\delta}}{\psi_j(rs_j)} \quad (3.5)$$

where  $\psi'_j(r) = 0$  for radii where the function is not defined. This allows to separate the intrinsic instability of the  $i$ -th mode  $\Delta'_{ij}$  from the influence by the neighbouring mode  $j$ ,  $\Delta'_{ij}$ .

An analysis of the influence of the off axis contributions to  $\Delta'$  [49] reveals a destabilisation, which becomes the bigger, the closer the modes are positioned. This causes the mutual boost that has been mentioned above. It is easy to imagine, that a differential rotation of the two mode locations will influence the coupling behaviour. Indeed this question has been analysed both with analytical models [50] and numerical codes [48].

### 3.2.3 Kink Modes

The physical mechanism evoking the kink mode can be seen from the energy functional (Eq. 2.39). The mode is ideal and primarily current driven. It is appropriate to regard the low  $\beta$  approximation. Restricting the considerations to a large aspect ratio ( $\epsilon \equiv a/R_0 \ll 1$ ) and small mode numbers yields [2]:

$$\delta W = \frac{2\pi^2 B_{0\phi}^2}{\mu_0 R_0} \left\{ \int_a^0 \left( (r \nabla_r \xi r)^2 + (m^2 - 1) \xi^2 \right) \left( \frac{n}{m} - \frac{1}{q} \right) r dr \right. \\ \left. \left( \frac{2}{q_a} \left( \frac{n}{m} - \frac{1}{q_a} \right) + (1 + m) \left( \frac{n}{m} - \frac{1}{q_a} \right) \right)^2 a^2 \xi_a^2 \right\} \quad (3.6)$$

where the subscript  $a$  denotes the values at the plasma surface ( $r = a$ ).

This equation yields insight into the stability properties of the system: The **internal kink** ( $\xi_a = 0$ ) is stable for  $m > 1$ , since all terms become positive. The condition for

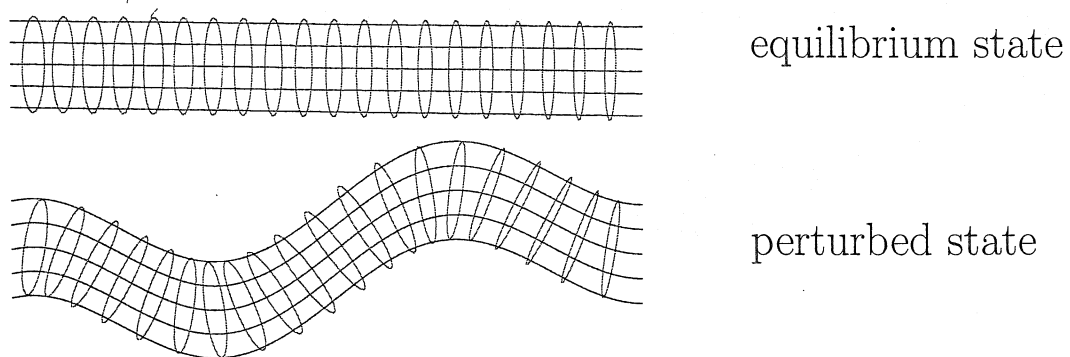


Figure 3.6: A simplified sketch of the kink instability: The helical magnetic field is split into the the toroidal (horizontal, blue) and the poloidal contribution (red) Only the toroidal field counteracts the shown perturbation, the poloidal field (associated with the toroidal current) amplifies it.

**external kinks** however is less restrictive. If  $m/n > q_a$ , the surface term becomes negative and might compensate the positive contribution of the plasma term. Just if  $m/n < q_a$ , stability is certain, in other words: The plasma is stable to external modes if the resonant surface is in the plasma. Whether a mode really becomes unstable depends on the value of  $q_a$  and the equilibrium current profile. Since the internal inductance is defined as

$$l_i = \frac{2 \int_0^a B_{\Theta}^2 r dr}{a^2 B_{\Theta a}^2} \quad (3.7)$$

it characterises the current distribution. Kink modes turn out to be especially unstable for low values of  $l_i$  and a  $q_a$  slightly below the mode's helicity. The growth rates and the unstable domain degrade with a rising mode number  $m$ .

The reason that the toroidal current density and the associated poloidal magnetic field are yielding such an influence on stability can be seen in a heuristic picture of the instability. Fig. 3.6 presents a simplified sketch of the mode's topology. The helical field is divided into the toroidal and the poloidal contribution. The magnetic field is associated with a force pointing to the center of the plasma, since it has to counteract the pressure. If the column is kinked, the poloidal field lines move closer to each other on one side and away from each other on the other side. Thus the magnetic force is amplifying the instability and since the poloidal field is not bended, there is no repelling contribution. It is just the superposed toroidal field that yields a stabilising contribution, since the field lines oppose the deformation.

The shown picture also illustrates, why the internal kink is more stable than the external kink. As in this case only the inner domain of the plasma is exhibiting the described deformation, the kinked column is surrounded by the outer undisturbed plasma. Thus the plasma needs to be compressed at the expense of free energy, which yields a stabilisation on the mode. The external kink requires a vacuum around the plasma, since a rigid wall would not permit the surface displacement.

Fig. 3.6 is simplified in that the direction of the displacement on the poloidal is not varying along the toroidal angle. Such a topology would associate to the mode numbers  $(n = 1, m = 0)$ . In an arbitrary  $(m, n)$  case, the structure would resemble a screw-like twisted towel, which kinks due to the contracting force.

### 3.2.4 Ballooning Modes

The analysis of the current driven modes was focused on small modenumbers as high  $n$  modes tend to be strongly stabilised by the energy required to perturb the magnetic field. This stabilisation is vanishing around the rational surface associated to the mode's helicity as seen from Eq. 3.6 as  $q = m/n$ . Therefore high  $n$  modes are concentrated around their resonant surfaces. In the limit  $n \rightarrow \infty$  the number of these surfaces becomes infinite and their separation zero, allowing a numerical treatment of the modes [51, 52].

As the volume contribution (Eq. 2.40) to the energy functional has been discussed it has been pointed out that due to the dot product of the curvature vector and the pressure gradient the contribution is positive and thus stabilising on the high field side ( $\kappa \parallel \xi_{\perp}$ ) and negative and destabilising on the low field side of the torus ( $\kappa \text{ anti-} \parallel \xi_{\perp}$ ). Ballooning modes are therefore localised in the region of unfavorable curvature. They limit the achievable  $\beta$  for a given shear. However a **second stable region** permitting even higher pressures at a very low shear arises from the negative local shear in the bad curvature region due to the Shafranov shift (Sect. 2.2.2) [22]. Both domains are connected by toroidicity and non-circular poloidal cross sections, providing access to this operational range to shaped tokamaks. It is second stability that surpresses ballooning modes in the low and negative shear region of advanced scenarios. This mechanism is essential for the creation of a transport barrier and hence for the advanced tokamak concept.

### 3.2.5 Infernal Modes

Manickam et al [27] pointed out that in regions of low shear, the standard ballooning theory breaks down and low  $n$  modes can be destabilised. The emerging instabilities were called “infernal modes”. The analysis was extended to non-monotonic profiles [28] ascribing MHD activity observed in the JT-60 tokamak to the infernal mode and showing that  $\beta_{pol}$  in reversed shear profiles can be limited by this type of instability. Extensive parameter scans based on the CASTOR code can be found in [53].

## Chapter 4

# Decoupling of DTMs in TEXTOR-94

This chapter refers to experiments performed at the TEXTOR-94 tokamak. Reversed shear scenarios in this machine suffer from strong mode activity causing a flattening of the central profiles, therefore called an internal disruption. The activity is found in discharges with ohmic or RF (Radio Frequency) wave heating, however plasmas which are heated by NBI (Neutral Beam Injection) are stable though the magnetic properties of the equilibrium are similar.

On the basis of the experimental observation, which is briefly summarised in Sect. 4.1, the mode activity is identified as a set of coupled DTMs (Double Tearing Modes) of the helicities  $2/1$  and  $3/2$  in Sect. 4.2. Since a characteristic feature of the discharges with neutral beam injection is a sheared toroidal rotation of the plasma, Sect. 4.3 performs further studies on the influence of differential rotation and a variation of the distance of the rational surfaces on the growth of the instability. The coupling mechanism, which acts as the main driving force of the DTM, is discussed in detail.

Finally the numerical results are applied to explain the experimental observations in Sect. 4.4. It turns out that the stabilisation by NBI found in the experiment can indeed be ascribed to the sheared rotation introduced by the tangential injection.

## 4.1 DTM Activity in the Experiment

The experimental results are only briefly reviewed. More detailed information can be found in [54].

### 4.1.1 The Device

TEXTOR-94 stands for "Tokamak EXperiment for Technology Orientated Research". It is sited at Jülich, Germany, has a major radius of  $R = 1.75$  m and a minor radius of  $a = 51$  cm. The plasma temperature is somewhat lower than on ASDEX Upgrade and reaches approximately 1 keV.

The shape of the poloidal cross section is circular, and the plasma is limited by a toroidally symmetric belt limiter. Poloidal limiters can additionally be inserted into the plasma. Supplementing the ohmic power, radio frequency heating can be supplied by two ICRH (Ion Cyclotron Radiative Heating) antenna with a maximum heating power of 2 MW each. On top of that, there exist two tangential neutral beam injectors providing up to 4 MW. The safety factor profile is measured by FIR (Far InfraRed) polarimetry [55]. Since this requires a twofold inversion of line integrated data, the accuracy of the profiles is limited to 20% - 30% at half radius and even less in the plasma centre [56].

### 4.1.2 Reversed Shear Scenarios

The examination of high-Z materials like tungsten and molybdenum as a possible divertor material is part of the scientific program of TEXTOR-94. During these studies material erodes from test samples which have been inserted into the plasma. It has been observed that these high-Z impurities accumulate in the centre where they cause radiation and cool the inner domain; thus reducing the conductivity of the core affects the current profile resulting in a change of the safety factor. It has been shown by measurements that the change is sufficient to obtain a strong shear reversal [56]. This presents an alternative way of generating this type of  $q$  profile to the more conventional strategy of early heating (see Sect. 3.1.4). It hinders the current diffusion to the centre resulting in a hollow profile of the current density.

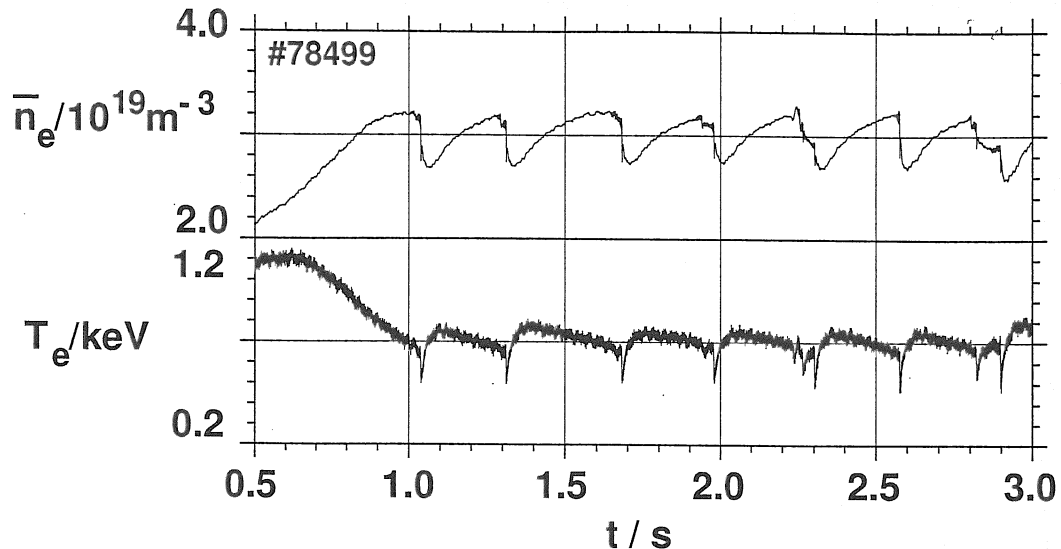


Figure 4.1: The temporal evolution of TEXTOR-94 #78499: The central values of electron density and the electron temperature versus time [54].

### 4.1.3 Internal Disruptions

Strange behaviour of the plasma was observed in the reversed shear scenarios: within 100 ms the electron density profile peaks, while the electron temperature and pressure are flattened or even become hollow. After these changes, there is a rapid decay in all profiles. The timescale of the final crash is less than 1 ms which rules out a diffusive process (see Eq. 2.15). The  $q$  profile is also changed during the crash as seen in Fig. 4.3. This behaviour is similar to the sawtooth instability [57].

The temporal evolution of the ohmic discharge (TEXTOR-94 #78499) is presented in Fig. 4.1 to illustrate this behaviour. The accumulation of sputtered material starts at  $t = 0.6$  s, as indicated by a drop in the central temperature. After the reversed shear has thus been established a series of crash events occurs.

Further insight is gained from the signals of an array of Mirnov coils. Fourier analysis allows one to separate the activity of the various mode numbers, as shown in Fig. 4.2. Note that the time axis has been stretched substantially focusing on the interval before one crash. The traces exhibit a strong activity of the helicities 2/1 and 3/2 evolving on the resistive timescale (Sect. 2.1.3) finally triggering the internal disruption. The following analysis will show that the activity is caused by DTM.

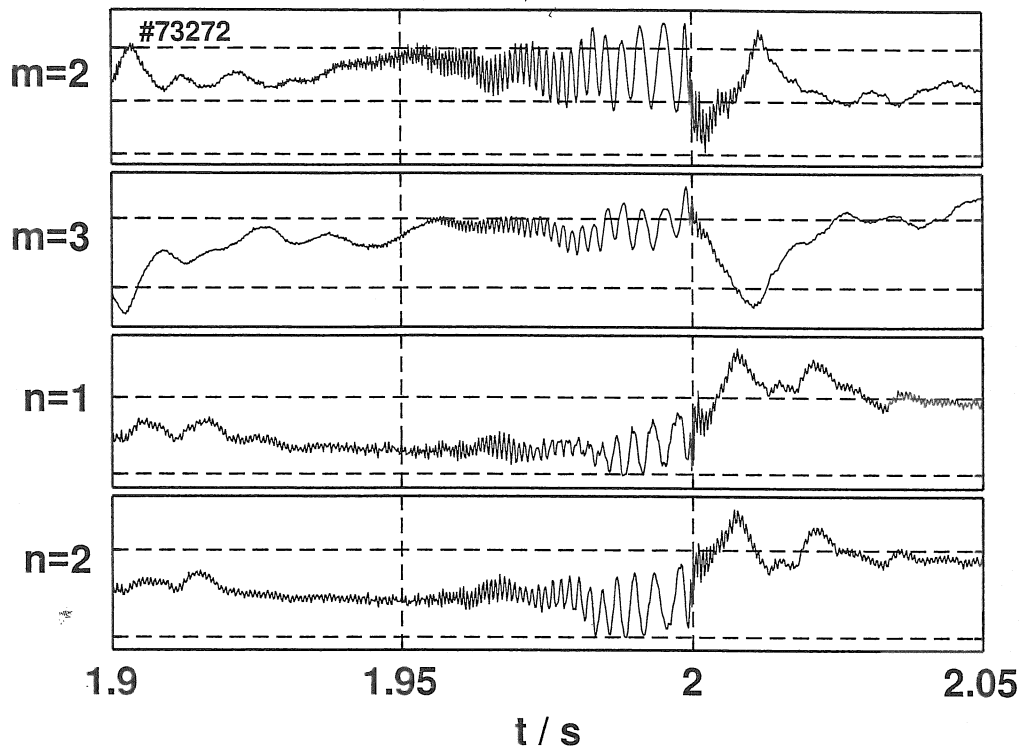


Figure 4.2: The Mirnov Signal of the Activity preceding a crash ( $t \approx 2$  s) in the ICRH heated discharge TEXTOR-94 #73272: Plotted are the Fourier amplitudes of the signals for various poloidal and toroidal mode numbers versus time [54].

Internal disruptions are found in reversed shear scenarios whether they are generated by impurity accumulation or early heating. Neither the equilibrium structure (i.e. the  $q$  profile) nor the mode behaviour differs for plasmas with ohmic and ICRH heating. For discharges heated with neutral beams the crashes are suppressed. This is astonishing since the magnetic properties of the plasma are not substantially changed by the choice of the heating mechanism.

#### 4.1.4 Equilibrium Properties

Two sets of equilibrium profiles are shown in Fig. 4.3. The discharge #79424 is an ohmic one but also represents the radiation heated experiments. #69876 has been heated by neutral beam injection. The profiles exhibit slight differences between



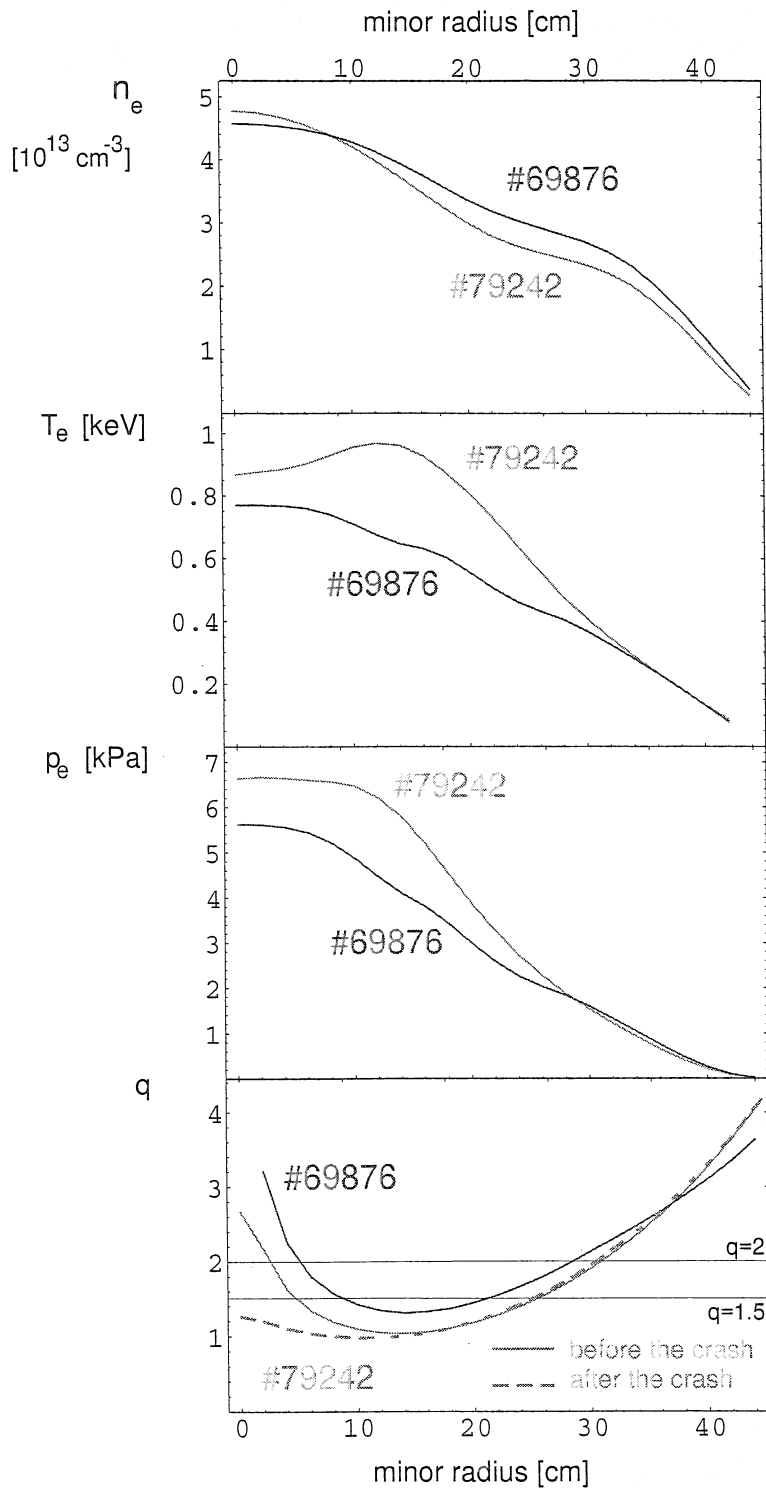


Figure 4.3: Experimental profiles of two TEXTOR-94 discharges. #79242 was purely ohmically heated, whereas #69876 was heated by NBI as well. The safety factor for shot #79242 has been displayed before and after the crash.

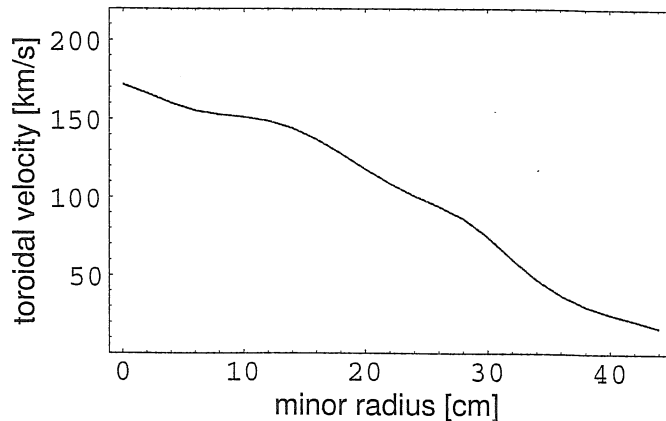


Figure 4.4: The toroidal rotation of the plasma in the TEXTOR-94 discharge #69876, caused by the neutral beam injection is plotted versus the minor radius.

the two types. The flattening of the electron temperature and pressure are already signs of the mode activity that is preceding the crash and has been described above. The change however is too small to account for the difference in stability. It can be seen that the  $q$  profile is changed during the crash. This change is ascribed to the enhanced current diffusion caused by the DTM.

An additional difference of the two types of discharges is the presence of a strong toroidal rotation imposed on the plasma by the tangential injection, as seen from the radial velocity profile (Fig. 4.4). This results in a strong relative movement of the resonant surfaces. Such a differential rotation damps the modes growth and thus contributes to a stabilisation of the plasma as can be seen in the following analysis. In both experiments the toroidal magnetic field was 2.229 Tesla.

## 4.2 The Plasma is Susceptible to the DTM

Linear calculations on the two shots presented in Sect. 4.1 have been performed. They indicate a DTM growth on timescales comparable to the ones in the experiment.

## 4.2.1 Equilibrium Reconstruction

The stability analysis is based on a numerical equilibrium, i.e. a solution of the Grad-Shafranov equation (Eq. 2.19). This solution has been generated using the HELENA code presented in Sect. 2.2.2.

Instead of preparing two distinct equilibria, each one representing one of the discharges and comparing their stability properties a different strategy is followed: Utilising the common features of both shots one reference equilibrium has been created. It is to be conceived as a typical TEXTOR-94 reversed shear scenario rather than as the reconstruction of one particular discharge. Following this approach it is possible to separate different features to attain a closer understanding of the effects of mode growth and damping rather than just to reproduce the experiments.

The profiles of both shots are similar in shape, but not in the absolute values of the  $q$  and the pressure profile as seen in Fig. 4.3. #69876 has been chosen as a reference, while #79242 is characterised by a slight increase of the central pressure and a lower minimum in the safety factor  $q$ , associated with a wider distance between the rational surfaces.

Performing the stability analysis on the reference equilibrium it is still possible to account for the difference in the safety factor. Since  $q$  is determined by the pitch angle of the helical field (Eq. 2.22) and thus by the ratio  $B_\Phi/B_\Theta$ , it is possible to change it by rescaling the plasma current that is generating the poloidal magnetic field while the toroidal field is kept fixed.

The modes we will study are primarily current gradient driven, the pressure enters just via the stabilising “Glasser effect” (see Sect. 3.2.1). Since the pressure is low, the stabilisation is limited, and the slight difference between the two discharges is negligible.

Fig. 4.5 offers a comparison of the experimental profiles of safety factor and pressure with the reconstructed ones. The profiles agree well with the one exception of the behaviour of the safety factor on axis. Here it should be noted that  $q$  cannot have a gradient on axis (see Sect. 2.2.2) and that the diagnostics measuring it is less reliable deep inside the plasma as already mentioned in Sect. 4.1.1.

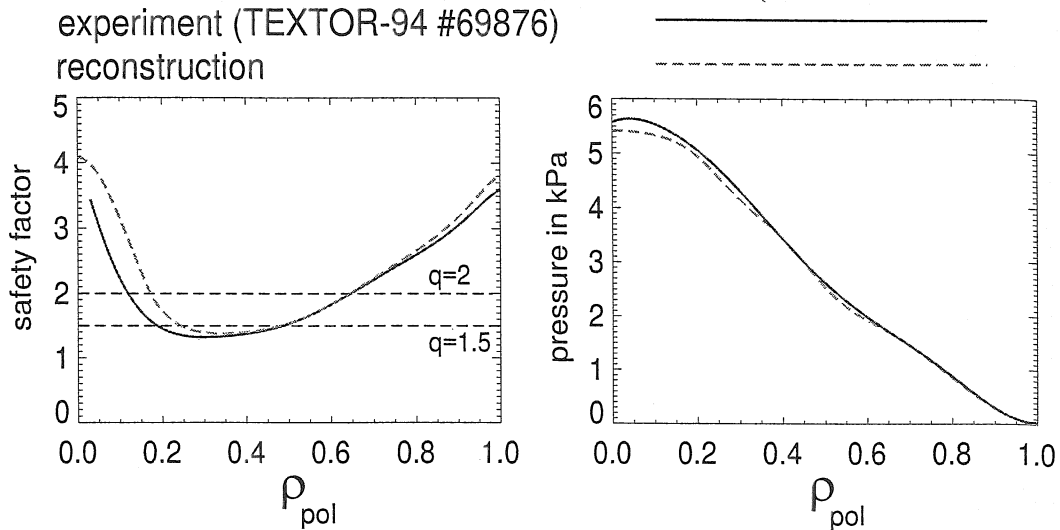


Figure 4.5: A comparison of the profiles for safety factor and pressure obtained from experimental data with the ones of the reference equilibrium shows good agreement.

HELENA solves the equilibrium in axisymmetric toroidal geometry. The resulting flux surface topology is presented in Fig. 4.6. The spatial coordinates  $X$  and  $Y$  are normalised to the minor radius of the plasma and span the poloidal plane. In the lower part of the picture the current density and the normalised flux are plotted along the symmetry axis ( $Y = 0$ ,  $-1 < X < 1$ ). The Shafranov shift (Sect. 2.2.2) relocating the inner flux surfaces to the low field side is clearly visible in both plots.

The circular shape of the plasma surface agrees with the actual shape in the experiment. Yet the use of a static equilibrium indeed implies a simplification. This will be justified before the effect of toroidal rotation on the mode's growth is actually examined.

#### 4.2.2 Linear Calculations Yield DTM Activity

The linear stability of this reference equilibrium has been examined using CASTOR. This code solves the linear MHD eigenvalue problem (Eq. 2.34). It has been described in Sect. 2.3.3.

### HELENA EQUILIBRIUM

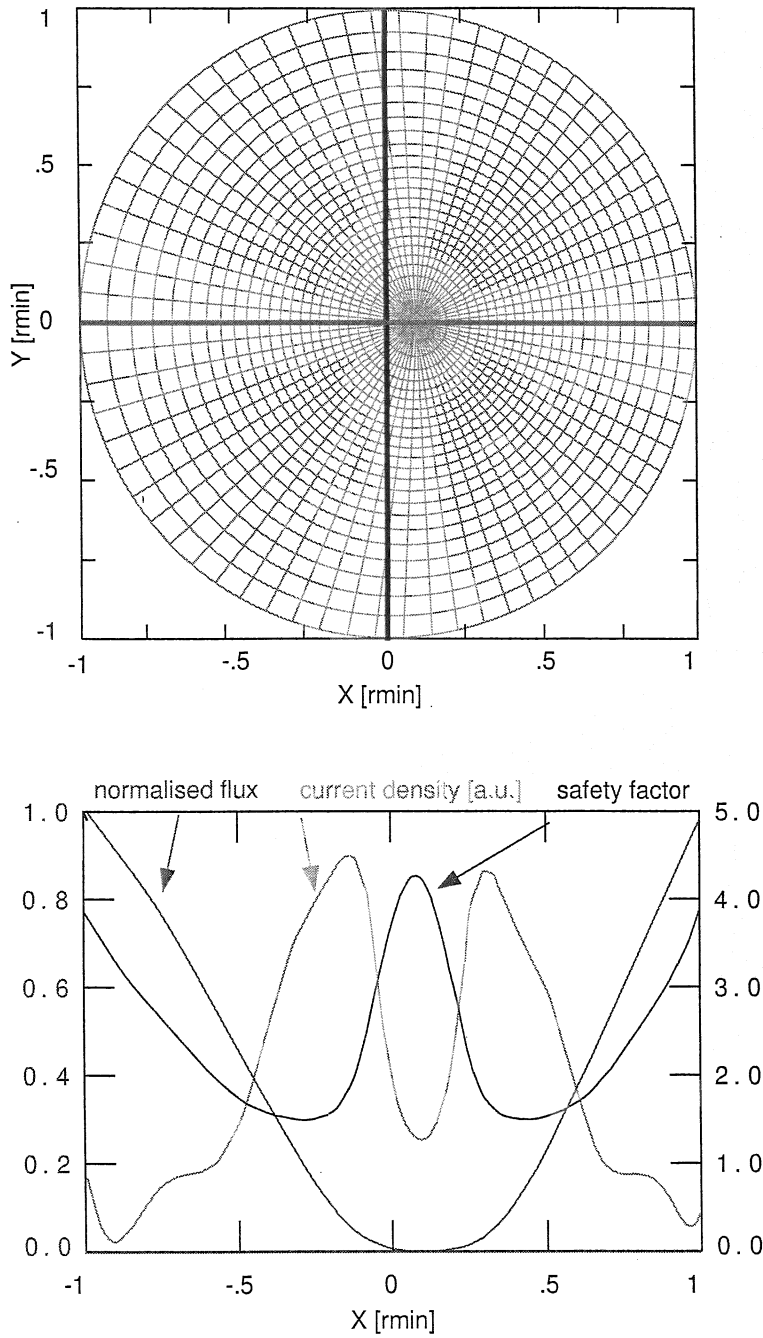


Figure 4.6: The flux topology and the  $\Psi(r)/\Psi(a)$ ,  $q$  and  $j_\Phi$  profiles of the reconstructed equilibrium. The current density, safety factor and the value of the normalised flux are plotted along the midplane of this domain ( $Y = 0$ ,  $-1 < X < 1$ ). The Shafranov shift is visible in both plots.

All calculations in this chapter consider 11 poloidal mode numbers ( $m$ ). Higher harmonics do not yield relevant changes since the amplitudes fall off quickly with the mode number (see Fig. 4.8 and Fig. 4.17). Neglecting the changes of the equilibrium that are caused by the evolving perturbation the toroidal symmetry is preserved in the linear picture. Therefore modes of different toroidicity do not interfere with each other. Accordingly the cases for toroidicity  $n = 1$  (associated with the 2/1 mode) and  $n = 2$  (associated with the 3/2 mode) have been treated separately.

The calculations have been carried out with free boundary conditions permitting external modes. A fast growing internal activity has been found. Displaying the characteristic structure of the eigenfunction and a resistivity dependent growth rate, the mode is identified as a DTM that has been described in Sect. 3.2.2.

The value of  $q_{min}$  has been varied as described in Sect. 4.2.1. Thus shifting the  $q$  profile up and down, the distance between the two  $q = 2$  surfaces changes as well. The response of the growth rate  $\Gamma = \text{Re}(\lambda)$  to this change is shown in Fig. 4.7. Plotted are the growth rates of two toroidal mode numbers  $n = 2$  (gray/green) and  $n = 1$  (black/red) against the minimum value of the safety factor.

To allow a certain DTM to evolve the associated rational surfaces have to be present in the plasma, so each mode is limited to the region where the minimum safety factor does not exceed the mode's helicity ( $q_{min} < m/n$ ). In these regions the distance between the correspondent rational surfaces can be read from the upper scale. It is common to use the value of  $\rho_{pol}$  (Eq. 2.18) as a measure for the minor radius. Instead of the physical length the difference in this quantity  $\Delta\rho_{pol}$  will be used to characterise the space between two points of that domain. It is simply referred to as distance in the following.

For a low  $q_{min} \approx 1.2$ , the  $q = 2$  and  $q = 1.5$  rational surfaces are very far apart, so both modes are relatively stable. As the  $q$  profile is lifted, the 3/2 surfaces draw nearer to each other. The two tearing modes lock and begin to destabilise each other. Once the modes are very close, the rational surfaces approach the bottom of the  $q$  structure. Since the valley is associated with a maximum in the current density (comp. Fig. 4.6), the current gradient at the mode location providing the drive of the tearing mode (see Sect. 3.2.1) decreases and the mode is weakened. The pressure profile can also contribute to this effect: As the transport barrier is asso-

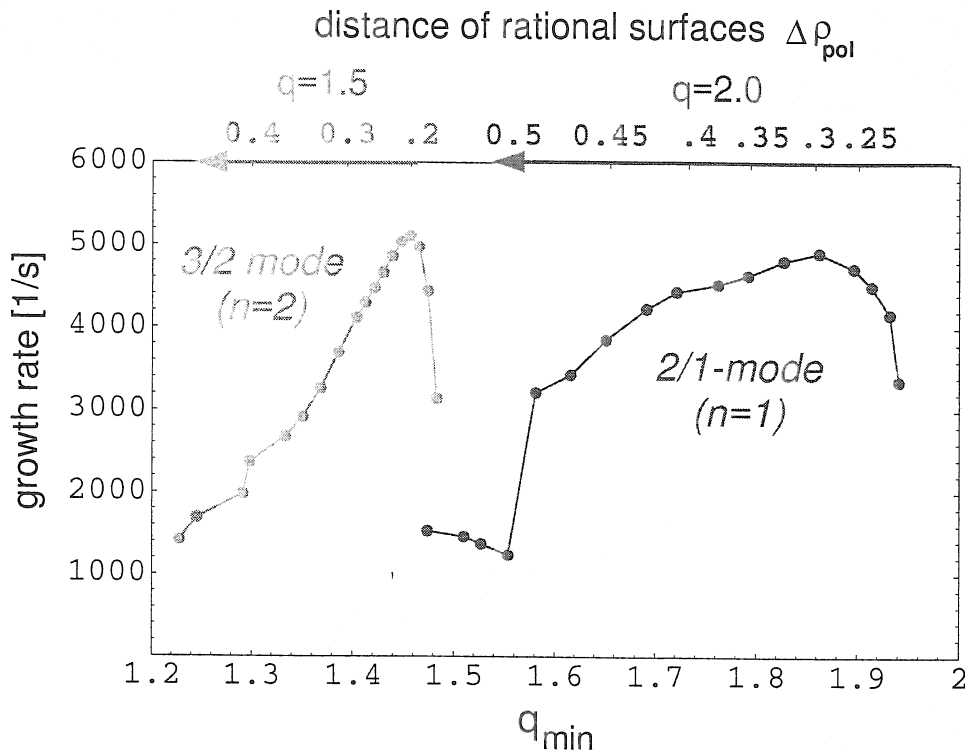


Figure 4.7: Plotted are the linear growth rates of 3/2 and 2/1 DTM activity, as obtained with the CASTOR code for varying  $q$  profiles. On the upper scale one can see the distance of the mode locations, that changes as the safety factor is scaled up and down.

ciated with the low shear region (see Sect. 3.1.4) the Glasser effect can contribute to a stabilisation. In our example however there is no distinct barrier visible in the pressure (see Fig. 4.5). As  $q_{min} = 1.5$  is reached the correspondent rational surfaces are expelled from the plasma and the mode activity disappears.

From here on we will regard the 2/1 mode since this is the fastest growing instability. Since the  $q = 2$  surfaces are still quite distant to each other there is a narrow region of relative stability  $1.5 < q_{min} < 1.6$ . Passing that, the 2/1 mode becomes suddenly more unstable to exhibit a strong activity over a wide region of parameters  $1.6 < q_{min} < 1.9$ . The growth rate increases as the mode locations move closer because the mutual influence of the modes is growing. Since the equilibrium gradients differ for different radii, there is an additional structure superposed upon this rise. Around  $q_{min} = 1.9$  the growth rate decreases as the two DTM islands melt together. The mode vanishes completely as the rational surfaces disappear.

The DTM instability has been found to be a robust feature of reversed shear scenarios at TEXTOR-94 as long as there are small  $m$  rational surfaces at a low distance to each other present in the plasma. So far the stabilising influence of the rotation, caused by NBI has not been taken into account.

### 4.3 Decoupling Mechanisms of the 2/1 DTM

The 2/1 branch has been picked as the subject of further examinations. The reason for this choice is threefold:  $\Delta\rho_{pol}$  is bigger for this helicity resulting in a higher differential rotation, which suggests a key role in the stabilisation by the neutral beam injection. In addition the wider separation implies that the fully evolved modes short circuit a wider interval of the minor radius and are therefore essential for an explanation of the observed transport (see Sect. 3.2.1). Finally the sudden change of the growth rate around  $q_{min} \approx 1.6$  in Fig. 4.7 is an interesting feature.

Two ways of stabilising the DTM are examined independently. One is to spatially separate the mode locations and therefore weaken the mutual coupling, the other is to introduce a sheared toroidal rotation prohibiting the locking of the modes. The results permit an insight into the coupling mechanisms of the DTM, they are of a general nature and can be at least qualitatively applied to other helicities as well.

#### 4.3.1 Decoupling by Distance

##### The Spatial Structure of the Mode

Fig. 4.7 has shown the reaction of the 2/1 modes growth rate to a variation of the distance of the rational surfaces. The sudden change at  $\Delta\rho_{pol} \approx 0.5$  is associated with a change of the mode's spatial structure. This rearrangement will be referred to as a shift between even and odd phase. A case without a fixed phase will be called unlocked. The effect, the topology yields on the growth rate will be separated from the increasing mutual boost, the approaching modes yield on each other. This boost will be referred to as coupling. The distinction made is artificial but convenient for the further discussion, which will show that both effects are related and result from the off diagonal matrix elements of  $\Delta'$  (Eq. 3.5).



The transition between odd and even state can be observed on the eigenfunctions shown in 4.8-1-11-111. Presented is the real part of the complex eigenfunction of the radial displacement plotted against the minor radius for three example distances. The imaginary part is omitted since it is very similar as long as there is no rotation involved. Within the linear picture, the graphs can also be taken as a plot of the plasma displacement  $\xi_r$  itself.

In the upper case the modes are very distant resulting in an even state. In the second example the modes are closer, so the DTM is fully evolved. The third picture displays the structure for very closely positioned modes.

Fig. 4.8-a-b sketches the projections of the field lines onto a section of the poloidal plane exhibiting the island structures for an even and an odd DTM. The growth of the instability is associated with the so called "Rutherford" current flowing around the rational surfaces [58]. The direction of this disturbed current is indicated in the O- and X-points.

**Intermediate Distances Yield the Typical Odd DTM Structure:** Fig. 4.8-11 depicts the typical features of a DTM eigenfunction. Each resonant surface in the plasma is associated with a jump in the corresponding helicity, indicating an island chain. The dominant structure is the  $m = 2$  helicity. Although the other poloidal numbers contribute, the plasma topology will be dominated by the two islands of helicity 2/1.

The structure of the mode can be derived from the mode profiles shown by the use of Eq. 2.43. In principle it is necessary to evaluate the sum over the poloidal harmonics and to consider the real and imaginary part of the profile. However the consideration can be restricted to the dominating  $m = 2$  contribution. If we choose the poloidal cross section at a toroidal angle of  $\Phi = 0$  we are left with a rather simple expression for the physically relevant real part of the disturbance:

$$\xi(\rho_{pol}, \Theta) \approx \text{Re}(\xi_2(\rho_{pol})) \cdot \cos(-2\Theta) - \text{Im}(\xi_2(\rho_{pol})) \cdot \sin(-2\Theta) \quad (4.1)$$

Following the eigenfunction in Fig. 4.8-11 the plasma topology schematically sketched in Fig. 4.8-b is obtained. First we regard an poloidal angle of  $\Theta \cdot m = 0$  corresponding to the baseline of the topology picture. The cos function yields unity while the sin is vanishing, therefore the displacement can be read directly from the real part of the eigenfunction.

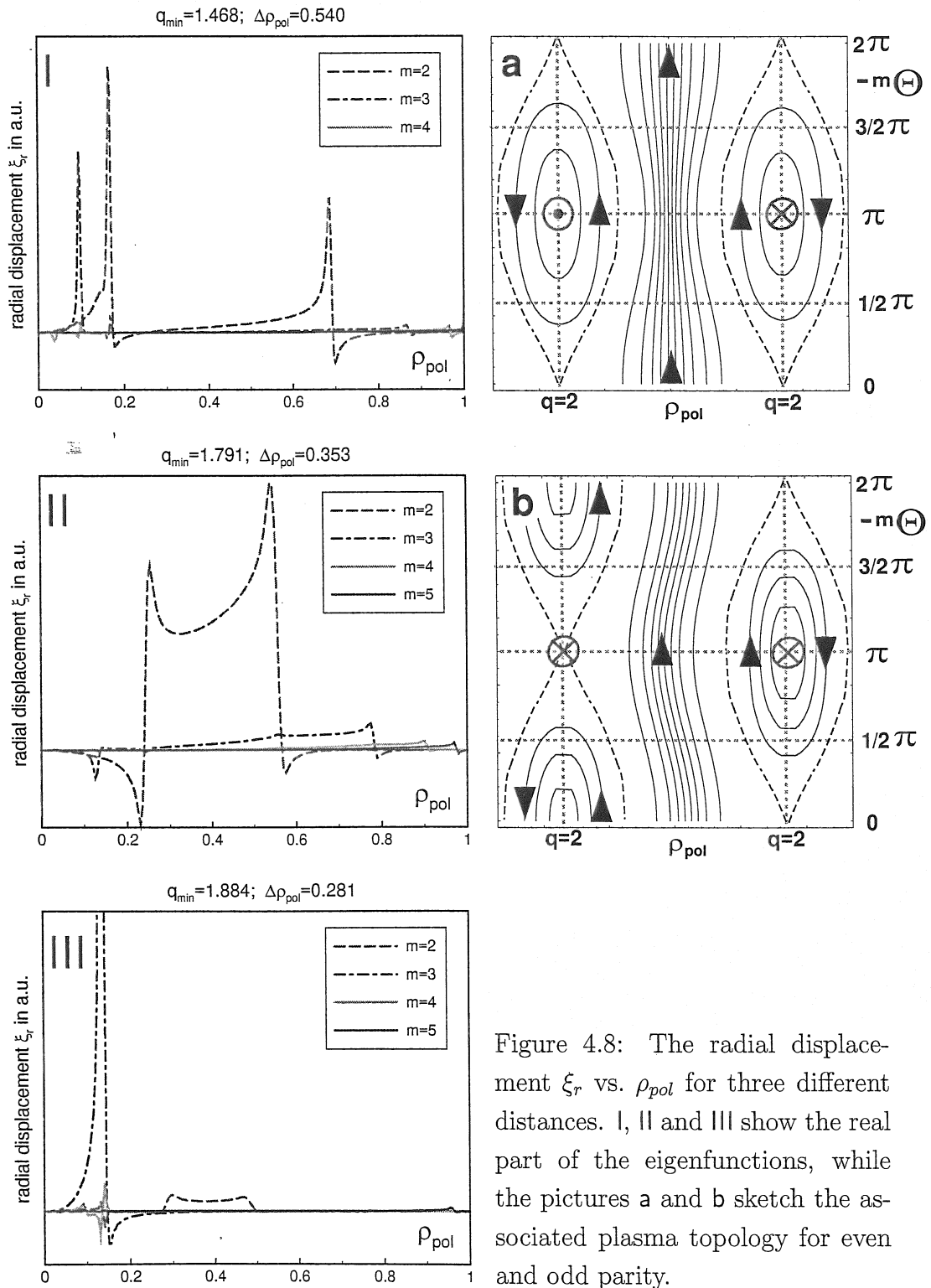


Figure 4.8: The radial displacement  $\xi_r$  vs.  $\rho_{pol}$  for three different distances. I, II and III show the real part of the eigenfunctions, while the pictures a and b sketch the associated plasma topology for even and odd parity.

The displacement starts negative, corresponding with a shift to the left. It grows stronger, as the rational surface is approached and changes sign there. This is how the island is formed. Now the displacement remains positive, so the intermediate flux surfaces are all shifted to the right. The X-point is formed in a corresponding way. As the helical angle is changed to  $-\Theta \cdot m = 1/2 \pi$ , the cosine yields -1 so there is first an X-, then an O-point.

It should be noted that the ordinate of the topology plot represents the product of the poloidal angle and the poloidal mode number ( $m = 2$  in this case). It is therefore misleading that its scale spans an interval of  $2\pi$ , the range covered is really just one half of the physical domain, so there follows a second pair of islands.

**At Small Distances the DTM Disappears Again:** Figure 4.8-III shows the eigenfunction for close distances between the rational surfaces. Since the minimum in  $q$  is associated with a peak in the current density (Fig. 4.6), the current gradient at the mode location is reduced. The dominating structure is now the single tearing mode at the inner  $q = 3$  surface which has moved to a higher  $\rho_{pol}$ . Nevertheless, the DTM is still essential for the growth of the instability since this arrangement can be stabilised by a sheared rotation, as shown later on.

**For Great Distances the Mode Topology is Even:** Fig. 4.8-I shows the structure of the even mode. Essentially, the left part of the  $m = 2$  component changed its sign which corresponds to a shift of the inner island indicated in Fig. 4.8-a as can be easily reconstructed with the considerations related above.

**The modes yield a force on each other:** For the even case the modes have the same phase in the poloidal plane, so the O-points of neighbouring islands are placed at one poloidal angle. This implies, that the Rutherford currents are running opposite to each other. The magnetostatic force between the two O-points is therefore repelling, while the X-points of one and the O-points of the other island chain attract each other since they are associated with parallel currents.

**The Transition:** Each of the two cases (even and odd) presents a valid solution of the eigenvalue problem of linear stability (Eq. 2.34). The fact that only one solution is found numerically does not imply the non-existence of the other. The eigenvalue of the even solution is usually very small because the mode has to counteract the

repelling force between the two disturbed currents. If the modes are moved further apart and the magnetostatic force between the island chains is weakened, the growth rates become comparable. Therefore the even solution “masks” the odd one. Starting a nonlinear simulation from the even case it is found, that one island chain shifts and the parity becomes odd [59].

### The Growth Rate

The transition between the two geometries and the associated sudden change of the growth rate exhibited by Fig. 4.7 is also visible in Fig. 4.9, which is another representation of the same data. Here, the real part of the eigenvalue has been plotted against the distance between the two 2/1 modes. The abscissa values decrease to the right side to preserve the main features of the graph, otherwise it would have flipped over since a low  $q_{min}$  matches a big  $\Delta\rho_{pol}$ .

**The sudden change in the growth rate results from the topology change:** The point of the increase in growth rate ( $\Delta\rho_{pol} \approx 0.5$ ) constitutes the borderline between the regime of odd and even mode activity. It can be seen from linear theory [50] that the transition inverts the effect of the off-axis elements of  $\Delta'$  (comp. Sect. 3.2.2). While the mutual influence of the island chains, which is described by this term, destabilises an odd mode, it stabilises an even one. A less formal argument can be obtained from an energy consideration. As the force between the O- points is repelling, the shift from the odd to even parity requires the islands to do work against each other and reduces the free energy of the mode, thus weakening its growth. Finally one can assume that the growth rate of a decoupled mode with no off-axis contribution to  $\Delta'$  lies halfway between the coupled and decoupled values. The prediction of the decoupled growth rate at  $\Delta\rho_{pol} \approx 0.5$  is marked in Fig. 4.9. Thus the contribution of the coupling (i.e.  $\Delta'_{ij}$ ) to the growth can be separated from the “intrinsic” growth of each mode (i.e.  $\Delta'_{ii}$ ).

In the nonlinear stage, an additional contribution arises from magnetic tension. It is easier to bend the undisturbed flux surfaces between the shifted island chains as can be seen in Fig. 4.8-b, than to compress the same surfaces between two island that are in even phase like in Fig. 4.8-a. This reduces the free energy of the system and is stabilising in the latter case. Since the linear stability problem only considers the onset of the mode, the islands can be regarded as infinitesimal small and the above described effect is not accessible to linear calculations.

As the Modes Draw Closer, the  $\Delta'_{ij}$  contribution grows stronger: The coupling between the two islands depends on their distance, therefore the growth rate is rising as the distance between the modes is reduced ( $0.3 < \Delta\rho_{pol} < 0.5$ ).

The  $\Delta'_{ii}$  contribution is weakened for small distances: As the modes move closer, the rational surfaces approach the minimum in the safety factor and the local current gradient is reduced (comp. Fig. 4.6). As the TM is a current gradient driven mode, this weakens the intrinsic growth of each island chain described by  $\Delta'_{ii}$ .

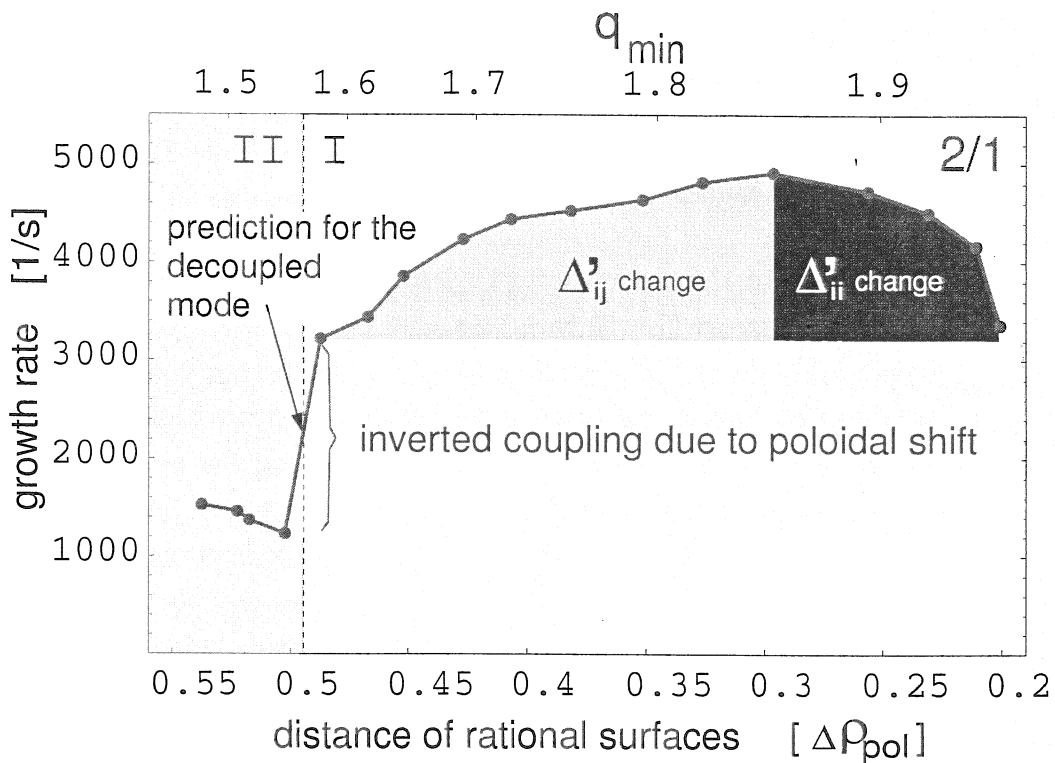


Figure 4.9: The 2/1 DTM growth rate  $\Gamma$ , as found with CASTOR in 1/s vs. the distance of the  $q = 2$  rational surfaces ( $\Delta\rho_{pol}$ ). The drastic increase at  $\Delta\rho_{pol} \approx 0.5$  marks the transition between odd (I) and even (II) parity. This allows an estimate of the contribution of the mutual coupling to the growth. The resulting prediction for the growth rate of an decoupled mode at  $\Delta\rho_{pol} \approx 0.5$  is marked. The succeeding rise is due to the growing coupling between the approaching modes which yields an increase of  $\Delta'_{ij}$ . Finally the growth rate is reduced because the local current gradient is reduced which weakens the intrinsic growth at each surface ( $\Delta'_{ii}$ ).

### 4.3.2 Decoupling by Differential Rotation

The poloidal orientation of the modes was found to yield a big influence on the stability of the plasma. In a plasma with a sheared rotation the modes can be deterred from obtaining a fixed phase by the drag of the bulk plasma. The following examinations are therefore devoted to the effect of differential rotation on the DTM's growth and frequency. At least the rotational decoupling of toroidally coupled classical TM in a monotonic shear has been subject to analytical [60] as well as numerical studies [50]. The formalism is applicable to DTM as well [49]. This application has just recently become subject of numerical studies [61, 16].

The magnetostatic force between the disturbed currents binding the islands together depends on the distance between the modes and opposes the disconnection. It is therefore expected to be the harder to unlock the islands, the closer they are. In Sect. 4.3.1 it has already been described that the force influences the free energy and the growth rate. The frequency of the mode will reflect it's co-movement with the plasma.

#### The static equilibrium approximation

Given a substantial toroidal rotation the equilibrium will change because the static MHD force balance (Eq. 2.16) is complemented by an inertia term. One consequence is that the mass distribution will be shifted to the low field side of the torus by the centrifugal force, so that density and thus the pressure are no longer flux functions [17]. Though considering toroidal rotation, the following calculations have been carried out on a static equilibrium which can only be justified up to a certain velocity.

To estimate at which velocity the static equilibrium approximation breaks down we compare the kinetic energy stored in the plasma rotation with the energy of the kinetic pressure. This relation is given by the square of the Mach number:

$$M_t^2 = \frac{m_i \Omega^2 R^2 a}{kT} \frac{a}{R} \quad (4.2)$$

Here  $m_i$  denotes the ion mass and  $n$  the particle density.  $\Omega$  is the frequency of the toroidal rotation and  $R$  is the big radius. The ion sound speed is given by:

$$c_s^2 = \frac{nkT}{nm_i} = \frac{p}{\rho_m} \quad (4.3)$$

So  $M_t$  is given by the fraction of the rotation velocity on axis over  $c_s$ :

$$M_t = \frac{v_{tor}}{c_s} \quad (4.4)$$

Inserting the experimental plasma parameters from Sect. 4.1.4, an ion sound speed of  $c_s \approx 253 \text{ km/s}$  is obtained. The experimental rotation of  $v_{tor} \approx 150 \text{ km/s}$  yields a Mach number of  $M_t \approx 0.18$ .

This number already justifies the use of a static equilibrium, but in order to rule out any inconsistency arising from the consideration of a high absolute rotation, a profile different from the experimental one has been used. Since the crucial parameter for the stability of the DTM is not the absolute speed of a mode, but the relative movement between the mode locations a step profile corresponding to a moving core plasma containing the inner mode and a resting shell containing the outer one has been chosen. To ensure numerical stability, the transition between the two regions is smooth.

The profiles are presented in Fig. 4.10, where the amplitude is given in units of the Alfvén frequency. For the physical and geometrical parameters discussed its highest value corresponds to a rotation of the plasma center of  $\approx 50 \text{ km/s}$ . Using these profiles, the examination can be restricted to moderate velocities similar to the differential rotation seen in the experiment. This results in a lower Mach number of  $M_t \leq 0.06$ .

Additionally the various positions occupied by the two rational surfaces as  $q_{min}$  is swept have been marked to verify that neither of the rational surfaces enters the region of sheared rotation. The therefore independent adjustment of mode distance and the differential rotation offers a separation of both effects and constitutes yet another advantage over the use of the experimental profile. A simpler profile prevents contradicting effects interfering with each other and yields a clearer result.

### Linear Growth Rate of the Mode

Extending the scan of  $\Delta\rho_{pol}$ , that was presented in Sect. 4.3.1, the central rotation has been varied as well. Thus the rational surfaces perform a relative movement with the speed  $v_{diff}$ . Fig. 4.11-a projects the results in the plane formed by the

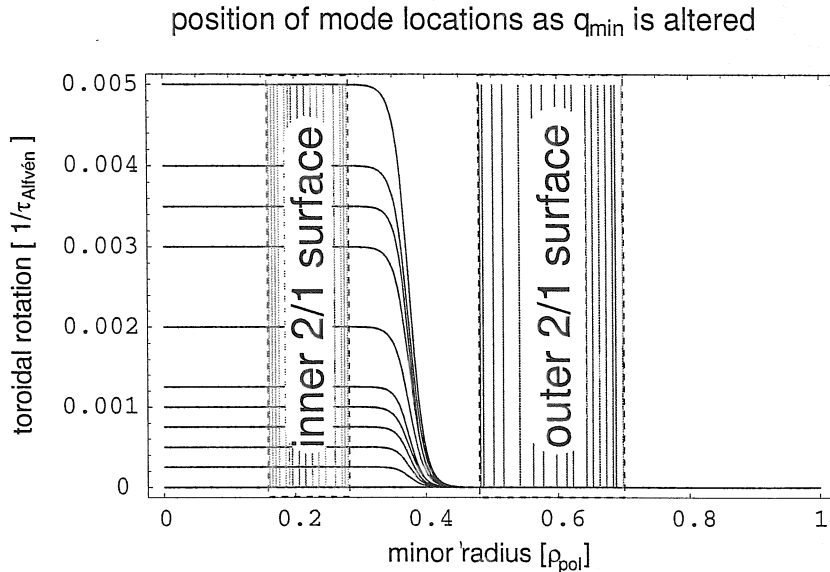


Figure 4.10: The plot visualises the velocity profiles used for the analysis. As the range of  $q$  profiles is swept by changing  $q_{min}$  the rational surfaces take various positions. These are indicated by vertical lines.

growth rate and the mode distance. In Fig. 4.11-b three example trajectories are projected into the  $\Gamma$ - $\Delta v_{diff}$  plane. Representing the rotationless case, the known relation between the mode distance and the growth rate (Fig. 4.9) reappears as the boldly plotted gray/green curve in Fig. 4.11-a. It displays the known sudden change, that was ascribed to the parity change of the islands. As the rotation increases this feature disappears and the whole curve drops to a saturation level.

The second diagram permits one to judge how fast the saturation occurs. Out of the many distances examined three representative cases have been selected:

- small  $\Delta\rho_{pol}$ , accordingly highly coupled modes with the highest growth rates
- intermediate  $\Delta\rho_{pol}$ , weakly coupled with lower growth rates
- large distance between the rational surfaces, therefore even modes with the lowest growth rates

In the first case of high coupling, rotation reduces the growth rate. The saturation level is reached at  $v_{diff} < 20 \frac{km}{s}$ . The weaker coupled mode is also stabilised, though the total effect is smaller - the saturation level is reached at  $v_{diff} \leq 10 \frac{km}{s}$ .



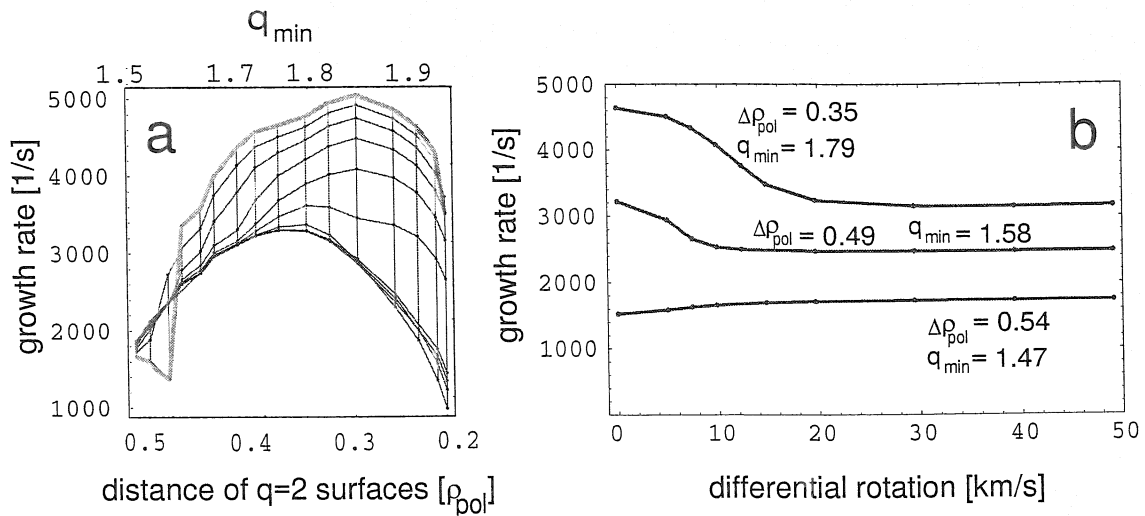


Figure 4.11: The distance of the rational surfaces and the velocity of the core plasma have been scanned separately. (a) is a projection of the data into the  $\Delta\rho_{pol}$ -growth rate plane. (b) is a projection of three example trajectories into the  $v_{diff}$ -growth rate plane.

In the third case, rotation yields no stabilisation but provides a source of free energy destabilising the system in agreement with theory [61]. The presented shape of the first and second case agrees well with analytical models based on the  $\Delta'$  formalism, describing the influence of a sheared velocity on the growth of coupled TMs [62, 48].

Both plots are projections of a two dimensional scan in distance and differential rotation. The complete surface is shown in Fig. 4.12 from two different view points to exhibit all details.

In the upper plot the sudden drop, which was associated with the topology change is clearly visible. This structure disappears quickly as the central plasma starts to rotate. The loss of this feature is due to the fact that the initial poloidal orientation of the two island chains becomes irrelevant, as the islands start to move with respect to each other. The mutual influence formerly dependent on their relative position is now averaged over the full circle.

The two island chains do not exhibit a relative movement for all values of distance and toroidal rotation. Especially for small distances and small rotation velocities, the islands counteract the movement of the bulk plasma and the growth rate does

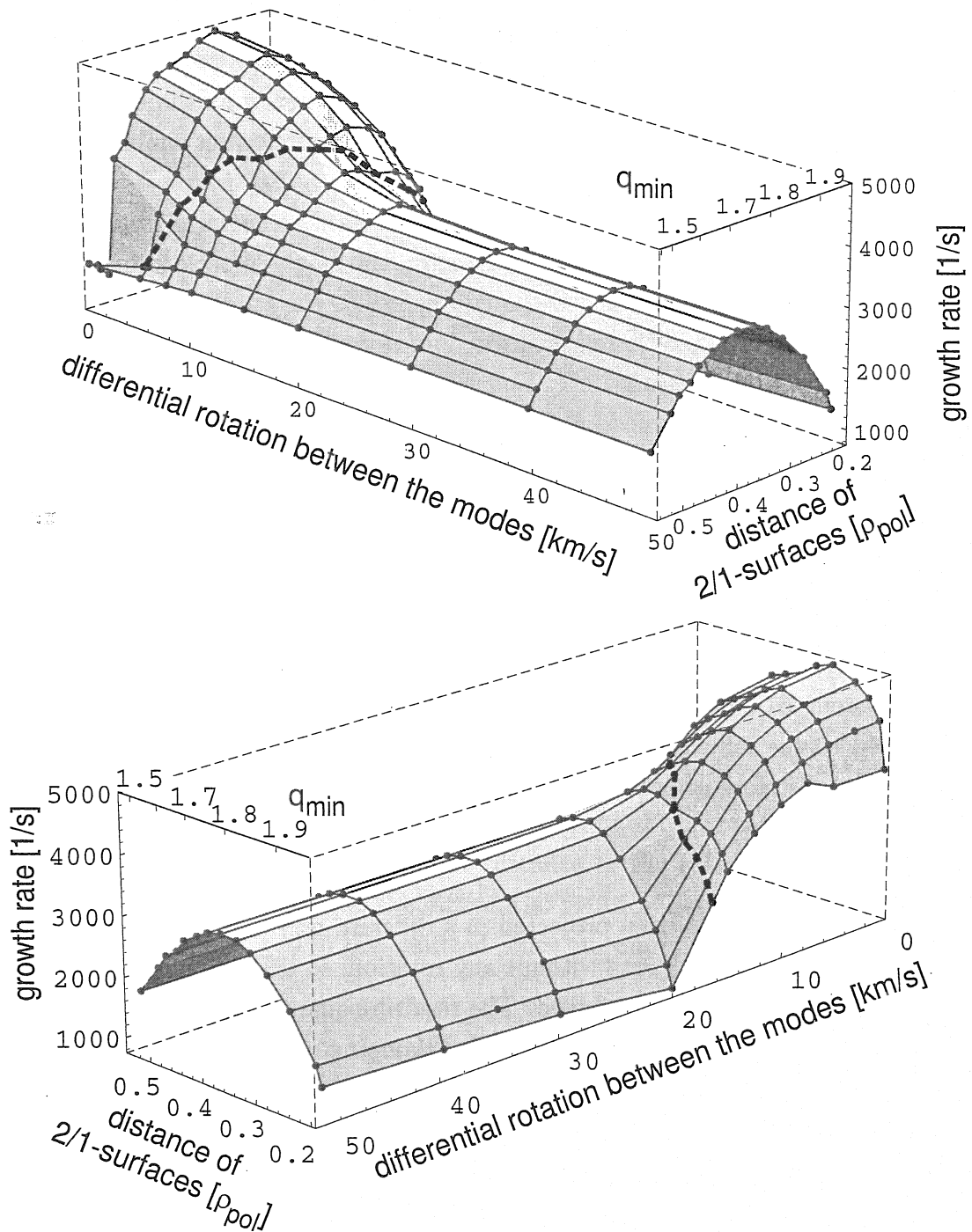


Figure 4.12: The distance of the rational surfaces and the velocity of the core plasma have been varied independently. The plots show the resulting surface from two different angles to exhibit all details. The dashed line separates the surface into one region where the modes are locked and unlocked region. Its strict definition is derived from the mode oscillatory behaviour in section 4.3.2.

not change compared to the static case. The reason for this is the magnetostatic force arising from the Rutherford currents which binds the two island chains together. In Sect. 4.3.1 it was alleged that this force depends on the distance of the rational surfaces, a statement that is confirmed by the following analysis.

The growth rate drops to the saturation level as the central plasma is rotating with a velocity of  $\Delta v_{diff} \approx 20 \frac{km}{s}$ . At this point, the magnetostatic force cannot prevent the islands from being unlocked anymore. Once the modes are thus separated a further increase of the sheared rotation does not affect the growth rate anymore. The transition from locked to unlocked islands is marked by a dashed line in the plot. Its strict definition is derived from the mode oscillatory behaviour in Sect. 4.3.2.

The lower diagram of Fig. 4.12 exhibits the mode behaviour at small distances between the rational surfaces. Again the dashed line separating the locked from the unlocked domain is visible. Saturation is reached above  $\Delta v_{diff} \approx 20 \frac{km}{s}$ . As the trajectories of a fixed distance pass the point of saturation, the growth rate increases again. The rise is evoked by the rotation, which increases the free energy of the system [61]. It can be seen, however, that the amount of this growth is small compared to the influence of the decoupling mechanisms discussed in this section and can be therefore neglected.

### damping

Now the same data has been projected in a different way. All the growth rates are normalised to the growth rate without any rotation, so the influence of the varying profiles on the eigenvalue is excluded. The resulting quantity describes the reduction of growth by the rotation and will be called damping.

Fig. 4.13 portrays the damping against the known parameters. Again there is a dashed line separating the region of locked modes from the one after the unlocking. This time the distance scale does not contain the point  $\Delta \rho_{pol} = 0.5$  because around this point the mode is even and the decoupling cannot yield a stabilisation.

Also in this representation, the saturation above  $v_{diff} \approx 20 \frac{km}{s}$  can be seen. In the saturated domain, the projections onto the  $\Delta \rho_{pol}-\Gamma$  plane fall monotonically towards small distances. From this it can be concluded that a reduction in mode

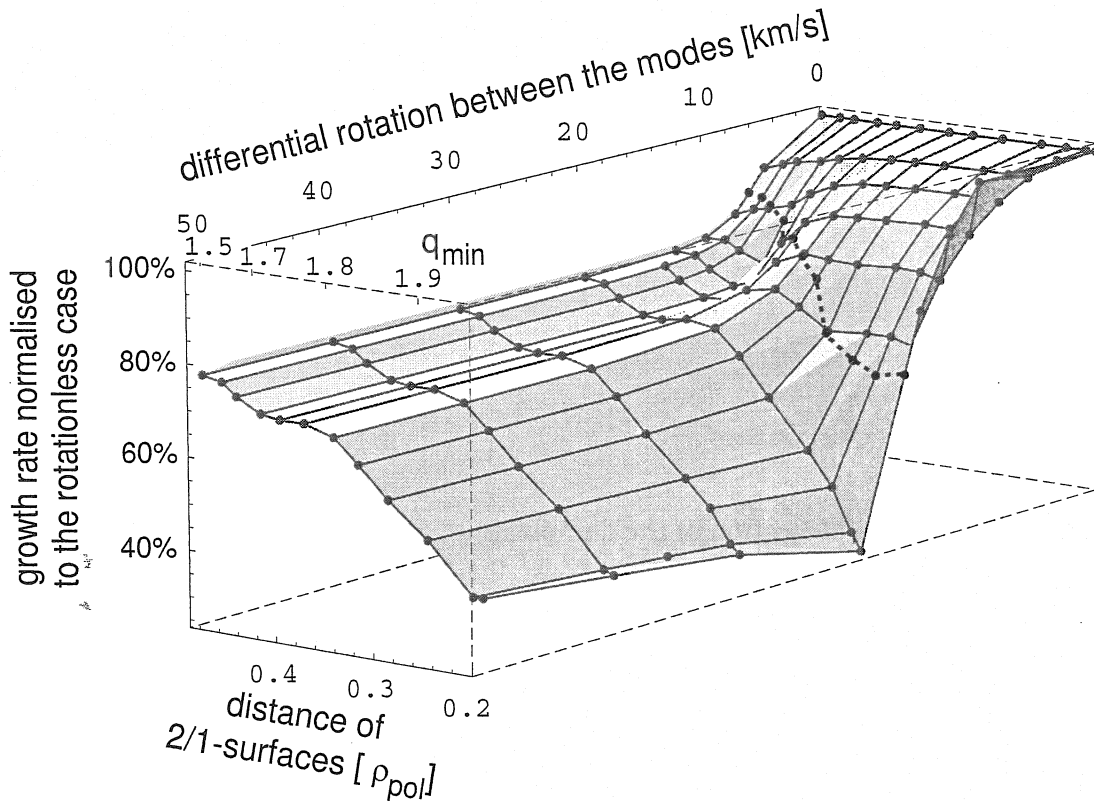


Figure 4.13: The damping, i.e. the growth rate,  $\Gamma$ , normalised to the value without rotation, is plotted against the distance of the rational surfaces and the velocity of the core plasma (i.e. the differential rotation between the two surfaces). Big distances ( $\Delta\rho_{pol} \geq 0.5$ ) are omitted since no damping is observed for these parameters.

distance is not only associated with a stronger magnetostatic force, and accordingly with an amplification of the mutual drive of the mode. Since also for the lowest distances the decoupling is significant, the eigenfunction shown in Fig. 4.8-III is still a DTM activity, although the mode picture suggests a single tearing mode character of helicity 3/1.

Also the dependence on distance of the binding force is confirmed by this diagram. Just around  $v_{diff} \approx 8 \frac{km}{s}$ ,  $\Delta\rho_{pol} \approx 0.4$  and again at  $v_{diff} \approx 15 \frac{km}{s}$  and minimal  $\Delta\rho_{pol}$ , there is a shoulder-like formation visible in the rising slope.

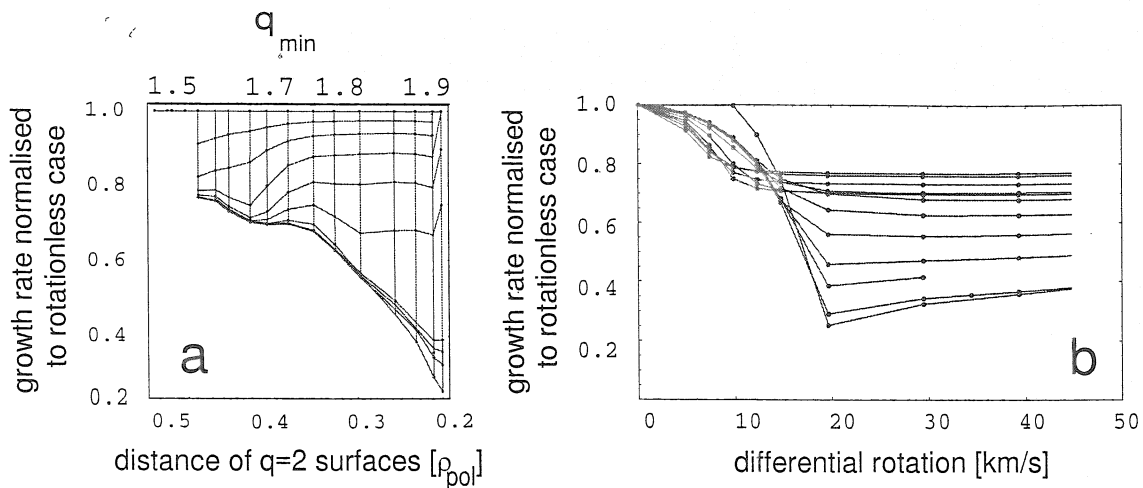


Figure 4.14: (a) is a projection of the damping into the  $\Delta\rho_{pol}-\Gamma/\Gamma_{v_{diff}=0}$  plane. (b) is a projection into the  $v_{diff}-\Gamma/\Gamma_{v_{diff}=0}$  plane.

The projections of the decoupling are shown in Fig. 4.14. Regarding diagram a, the rotationless data can be recognised as the top line equal to one (since the growth rates have been normalised to this case). The lowest line represents the saturated state, which falls nearly monotonically with decreasing distance between the two  $q = 2$  surfaces. The intermediate lines represent states with increasing differential rotation, some of which exhibit an increase of the normalised growth rate with decreasing  $\Delta\rho_{pol}$ . This increase indicates that modes with a greater distance between the rational surfaces are already disconnected while closer ones are still bound together. The structure corresponds to the shoulder of the three dimensional graph, Fig. 4.13. Accordingly the transition to the saturated state clearly starts at the higher distance.

Fig. 4.14-b represents the projection in the other plane. All the curves start at unity to drop to a saturation level at a certain position. It can be plainly seen, that the later the drop occurs, the greater it is and vice versa. Rational surfaces that are far apart are easy to disconnect, but the reduction in growth rate is limited, while nearby modes are harder to disconnect but offer a massive drop of the growth rate.

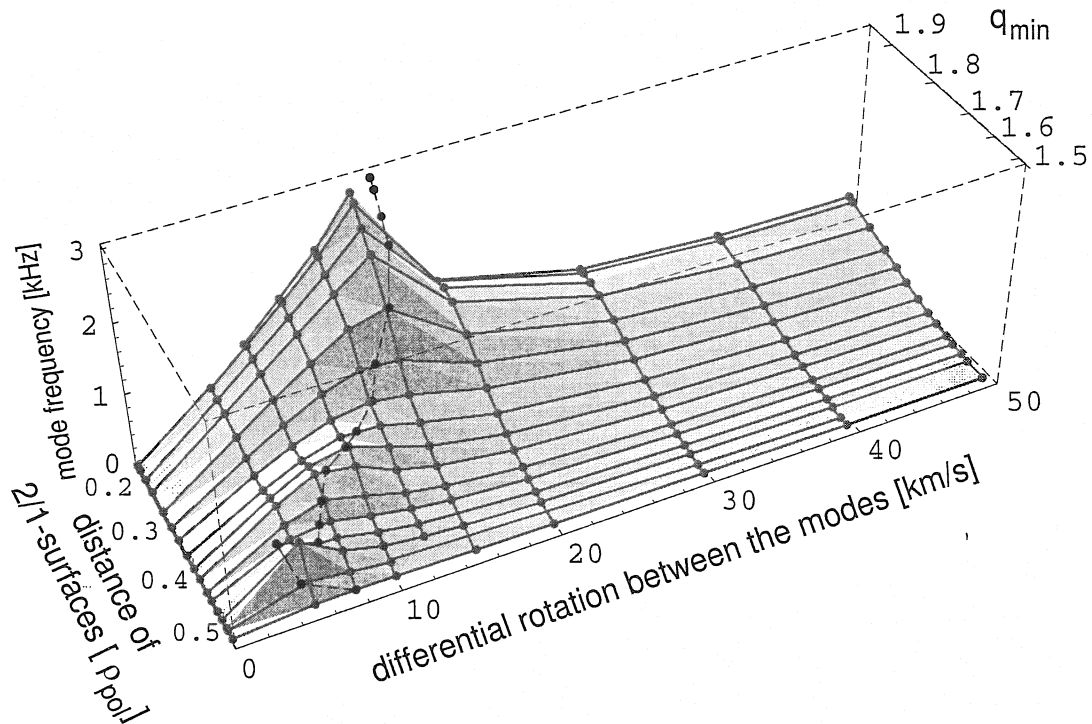


Figure 4.15:  $\omega$  versus  $\Delta\rho_{pol}$  and  $v_{diff}$ : For each curve of a fixed  $\Delta\rho_{pol}$ , a maximum has been estimated by interpolation. The position of these maxima has been marked with a set of blue dots and connected with a dashed line. This line marks the point at which the islands unlock.

### Mode Oscillation

The rotation of the bulk plasma induces an oscillation of the mode. The eigenvalue is complex anyway since we solve for resistive MHD, but the rotation dominates the imaginary part.

For  $\Omega \rightarrow \infty$  The mode picks up the frequency of the plasma at the location of the driving mode [60], but the result for finite  $\Omega$ , shown in Fig. 4.15, turns out to be more complicated. The mode is driven unstable by the outer rational surface, which is at rest (compare Fig. 4.10). Still the movement of the central plasma yields a drag on the DTM, that accelerates the mode. This drag is not surprisingly the bigger, the closer the surfaces are to each other and the faster the plasma core rotates. Still, when the drag becomes too large, the island chains disconnect and the mode oscillation relaxes again.

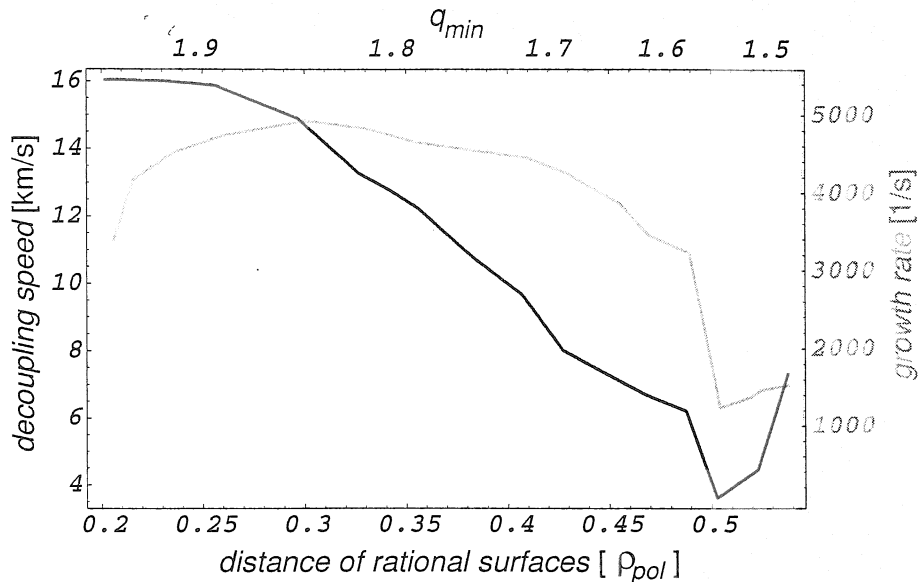


Figure 4.16: Plotted is the speed which is necessary to decouple the islands vs. their distance ( $\Delta\rho_{pol}$ ). The curve is monotonically falling until the shaded domain is reached. The evolution of the growth rate has been superposed to illustrate that this is the domain where the island topology changes due to the large distance.

Since the outer mode supplies the drive, the reaction to an accelerating plasma core is first a co-movement and then a deceleration as the modes are disconnected. Thus the velocity at which the islands unlock can be defined as the maximum of the mode oscillation for a fixed distance. In Fig. 4.15 the points above the surface are the maxima of a spline interpolation and the dashed line connecting them separates the region of a connected DTM from the one of disconnected modes. It was this border line which was shown in the previous plots (compare Fig. 4.12 and Fig. 4.13).

Projecting this line to the plane formed by the two parameter axes yields the velocity necessary to decouple two modes as a function of their distance (Fig. 4.16). The graph is monotonically falling up to  $\Delta\rho_{pol} \approx 0.5$ , which is complying with the stated reduction of the binding magnetostatic force with an increase of the distance. The reason this trend does not hold for greater distances is, of course, that here the mode is already even in the static case. Therefore there is no force counteracting the unlocking leaving the decoupling speed meaningless. To illustrate this, a copy of Fig. 4.9 is superposed, showing that this is indeed the position at which the modes change parity.

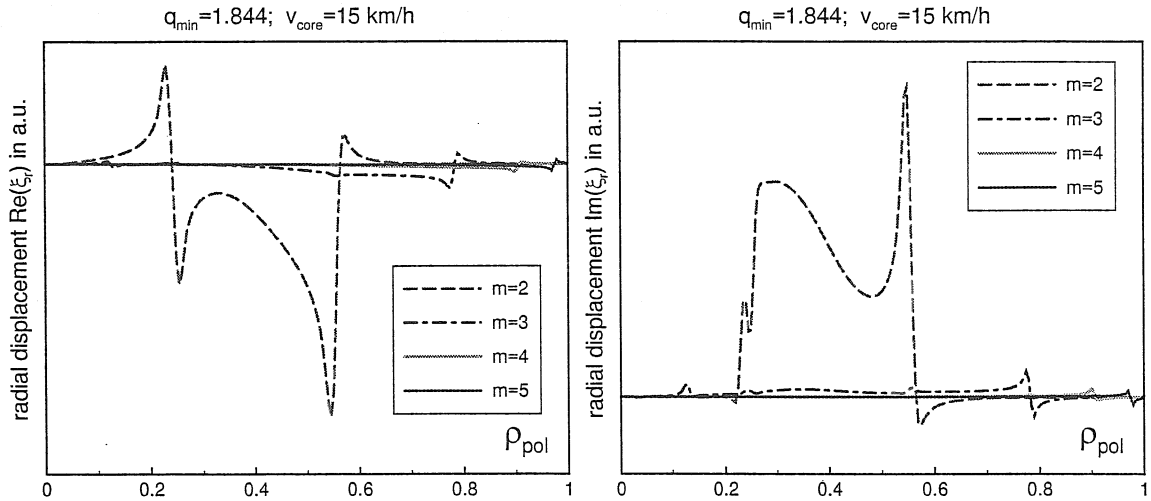


Figure 4.17: Real and imaginary part of the radial displacement  $\xi_r$  are projected vs.  $\rho_{\text{pol}}$ . The sheared zone has been extended to a tenth of the minor radius to obtain a clearer picture.

### Mode Structure

Finally, the structure of the eigenfunctions is examined. Unlike before, the imaginary part differs substantially from the real one because the rotation amplifies the non-hermitian character of the system. Again, the perturbation topology can be derived from Eq. 2.43. This expression shows, that exchanging both graphs corresponds to a mere shift in poloidal direction.

The outer mode is the one surviving the decoupling as could be seen from the oscillatory behaviour. The eigenfunction of the rotational case is shown in Fig. 4.17. One of the branches persists to exhibit the typical DTM character, whereas the other is changed by rotation. The right half of the profile is not altered, so the topology of the outer island chain does not change. However, the inner island is deformed by the relative movement with respect to the outer region. Since there is still a jump visible, an island will continue to exist.

The preceding examination allows a comparison of the different stabilisation mechanisms in the linear  $\Delta'$  theory (comp. Sect. 3.2.2). Fig. 4.18 presents the stabilisation yielded by rotation and an increase of the distance. The growth rate  $\Gamma$  has been plotted against the distance of the two surfaces for the rotationless case and the one with a substantial differential rotation yielding the described stabilisation.





As already marked in Fig. 4.9, the growth rate for a decoupled mode is expected halfway between the one for odd and even topology. This is confirmed by a comparison of the growth rates in the marked parameter range around  $\Delta\rho_{pol} \approx 0.5$  in Fig. 4.18. Since the mode distance is almost fixed for the points within this interval, the difference in stability is purely caused by a change of the mode's topology.

Case a represents an odd phase of the islands, as indicated in the topology sketch.  $\Delta'_{ij}$  acts destabilising in this case and stabilising in case c. For rotationally even modes the fixed phase between the islands is lost as in case b. Both topologies alternate, resulting in an intermediate growth rate which is equivalent to a suppression of the mutual coupling.

Now it becomes apparent why the modes with a low value of  $\Delta\rho_{pol}$  were reaching the lowest values in Fig. 4.13. As the intrinsic growth is already reduced the mode depends on the coupling and could be stabilised to values around 20% of the initial growth rate as can be seen from Fig. 4.14. For cases with a greater distance between the resonant surfaces ( $\Delta\rho_{pol} \approx 0.4$ ) the stabilisation could only reach 60%.

It has been shown that even a sheared rotation of moderate differential velocity is able to unlock and decouple the DTM. The saturated growth rate depends on the value of  $\Delta'$  at the most unstable surface that has to be calculated by solving the ideal MHD equations in the external regions. This result confirms the analytic theory of standard tearing modes [62] that also applies for DTM in reversed shear. The statement, that DTM can be "readily stabilised" by a sheared flow [61] seems to be too general and depends on the equilibrium profiles. The examination presented before rather relates a behaviour similar to results for standard tearing modes [48]. It should be remarked, that CASTOR does not account for viscosity. Viscous forces can be expected to further reduce the speed that is necessary to yield an unlocking. The resulting growth rate of the rotational case is not expected to be reduced substantially [63].

## 4.4 Application to the Experiment

The considerations have been motivated by the unclear "internal disruptions" in TEXTOR-94. The observed activity could indeed be identified as a set of coupled

DTMs since the equilibria are unstable to this instability and the observations (fast crashes, change of the safety factor profile etc.) can be explained with the presence of magnetic islands. Furthermore it has been found that NBI can easily decouple the modes and possibly yield a stabilisation.

#### 4.4.1 The Plasma is Unstable to DTM

##### The used Equilibria Represent the Discharges:

With the experimental uncertainty in the  $q$  measurement of at least 20% it is of no avail to study the differences of the safety factor between the particular discharges exhibited in Fig. 4.3, especially since the characteristic features of the profiles of the discharge #72942 are already caused by the presence of magnetic islands.

The uncertainty of the measurement has also to be kept in mind when one regards the central disagreement with the safety factor profile of the reconstruction shown in Fig. 4.5. The variation is induced by the necessity of a vanishing gradient on the magnetic axis (i.e.  $\rho_{pol} = 0$ ).

##### A DTM Activity has been Found. It can Account for the Observation:

A linear analysis yields a strongly growing DTM activity for most values of  $q_{min}$ . Only in a narrow region of parameters is there a gap indicating a relative stabilisation (Fig. 4.7). The reason for this gap is that the code converges to the even solution shading the odd one, which is of physical evidence. The result is of interest anyway since it allows to compare the odd and even case with the rotational decoupled mode, which has no fixed parity, as done in Fig. 4.18. The 2/1 DTM is not studied below  $q_{min} = 1.5$  because there the 3/2 mode is destabilised contributing to the further growth of the 2/1 DTM by nonlinear coupling which is not accessible by our simulation.

For experimental values of  $q_{min}$ , both the 3/2 and the 2/1 branch are unstable. These helicities are also seen in the diagnostics as shown in Fig. 4.2. The growth of two helicities implies 4 island chains. Since the islands short circuit the confinement as related in Sect. 3.2.1, they can cause the flattening of the central profiles of pressure and density.

If these islands overlap, they cause ergodisation, which can account for the crashes, which have been observed. However the saturated island size is not accessible to linear theory so it cannot be decided whether the islands overlap.

Also the observed flattening of the safety factor profile during the instability (Fig. 4.3) can be explained with DTMs. It has recently been shown that the island structure associated with a DTM accounts for a diffusion of the current density. This process can cause a flattening of the  $q$  profile [44].

#### 4.4.2 Differential Rotation can Contribute to a Stabilisation

A sheared toroidal rotation has been shown to be capable of unlocking the two modes and thus damping the growth. A comparison of the speed (Fig. 4.16) necessary to decouple modes at a certain distance and the experimental velocity profile (Fig. 4.4) shows that both helicities, the 3/2 and the 2/1 can be expected to be decoupled.

The decoupling resulted in a decrease of the linear growth rate. The remaining activity still exhibits a strong growth, which has not been observed in the experiment. This growth is caused by an unfavourable value of  $\Delta'(rs_2)$  at the outer rational surface. Though associated with a certain radius this stability parameter depends on the complete equilibrium, especially on the complete radial evolution of the current density and therefore the  $q$  profile. Due to the uncertainty of the measurement, precise agreement could not be expected. A lower value of the safety factor on the axis could possibly change the stability behaviour.

Because of the high rotation frequency, the islands are not directly accessible to the diagnostics in the presence of the neutral beam. A slower growing but persisting instability can still prevent the islands from overlapping and thus account for the observed suppression of the crashes.

Thus the calculations indicate, that the velocity profile imposed on the plasma by the NBI accounts for the stabilisation of the modes and the suppression of the crashes in the experiments.

## Chapter 5

# MHD in ASDEX Upgrade Advanced Scenarios

This chapter examines MHD events in reversed shear scenarios at ASDEX Upgrade. The special structure exhibited by this type of discharge accounts for a variety of activities, which deteriorate the improved transport or cause disruptions.

The instabilities found in the experiment could be identified as double tearing modes (Sect. 5.3), infernal modes (Sect. 5.4), and a combination of infernal and external kink modes (Sect. 5.6). It will be discussed how these activities affect the equilibrium and how their dependence on a variation of the experimental parameters can be explained. Means of stabilisation will be proposed.

To gain access to a higher value of the volume averaged pressure — and thus an increased  $\beta_N$  — it is preferable to push the internal transport barrier outwards increasing the domain of the hot plasma. As shown in Sect. 5.5, such a change could invoke external kink modes.

Theory predicts a stabilisation of external modes by a conducting structure in the vicinity of the plasma surface. Sect. 5.5.2 will discuss where a partial wall is best positioned to stabilise the external kink mode. The possible reduction in growth rate is estimated for axisymmetric ASDEX Upgrade geometry. These examinations are of special interest since the external kink in conjunction with the infernal mode accounts for disruptions in current experiments as shown in Sect. 5.6.

## 5.1 Experimental Background

This is a brief review of the experimental results, upon which the subsequent discussion focuses. More information on reversed shear at ASDEX Upgrade can be found in [36].

### 5.1.1 The Device

A picture of the poloidal cross section of ASDEX Upgrade has already been presented in Fig. 3.1. The device is sited in Garching, Germany and is a successor to the tokamak ASDEX, which was operated from 1980 until 1990. The name stands for “Axial Symmetric Divertor EXperiment” (compare Sect. 3.1.3). ASDEX Upgrade has a toroidal field of 2.5 T, a major radius of  $R \approx 1.65$  m and a minor radius of  $a \approx 0.5$  m. It is strongly shaped (elongation of the poloidal cross section  $\approx 1.6$ ), providing access to the second stable regime of ballooning modes (see Sect. 3.2.4).

The ions are heated by 4 neutral beam injectors (NBI) providing a total power of 20 MW. Up to 1.2 MW of ECRH (Electron Cyclotron Radiative Heating) can be provided by three gyrotrons. As a consequence temperatures in ASDEX Upgrade advanced scenarios can well exceed 10 keV.

The plasma can be analysed with a wide range of diagnostics, amongst which the Mirnov Coils and the SXR (Soft X-Ray) diagnostic give access to the MHD modes [64]. The ECE (Electron Cyclotron Emission) diagnostic is operated at various lines of sight. A topological analysis yields profile information of the associated temperature fluctuations [65]. The  $q$  profile can be derived from the 10-channel MSE (Motional Stark Effect) polarimeter [66] if at least one beam PINI (Positive Ion Neutral Injector) of the NBI is active.

### 5.1.2 ASDEX Upgrade Advanced Scenarios

The ASDEX Upgrade reversed shear discharges considered below were achieved by the method of early heating, described in Sect. 3.1.4. During the ramp-up phase 5 MW of NBI were injected resulting in a reduced current diffusion to the core and a strong shear reversal with initial  $q$  values on axis ( $q_0$ ) exceeding 6. The steep edge pressure gradients of an H-Mode plasma evoke a neoclassical current in that region and reduce the internal inductance (Eq. 3.7). In a reversed shear plasma, this would

cause MHD modes and subsequent disruptions, therefore this type of discharge has to be kept in the low confinement mode artificially. To prevent an L-H-transition, the plasma is kept in contact with the inner limiter on the high field side. Large pressure gradients ( $\approx 100 \frac{kPa}{a}$ ,  $a$  denoting the minor radius) and a high bootstrap current fraction (up to  $f_{BS} = 50\%$ ) have thus been achieved.

As the current is only partially driven by the bootstrap effect the reversed features of the profiles are transient. Though the diffusion process has been slowed down, the inductive current will still penetrate to the centre establishing a conventional current and  $q$  profile (comp. Fig. 3.2-1). The safety factor is therefore constantly changing throughout the discharge, as can be seen in the time traces of an example shot in Fig. 5.1-b. The whole profile is flattened and sinks to lower values until finally the reversed shear is lost.

As the  $q$  profile passes rational surfaces various MHD instabilities occur. They terminate virtually every shot by either destroying the ITB or even causing a disruption and constitute an obstacle for the further development of advanced tokamaks.

## 5.2 Technical Remarks

All theoretical investigations rely upon an accurate description of the real plasma configuration. The experimental measurements are therefore used as an input to the code CLISTE (Complete Interpretive Suite for Tokamak Equilibria), which calculates the solution to The Grad-Shafranov Equation that exhibits the smallest disagreement to the measurements [67]. The reconstructed equilibria are generally available for many shots and time points. They can be re-calculated with HELENA and thus be used as the basis of a linear stability calculation with CASTOR.

As one can specify the profiles of the pressure gradient and the function  $f$  (compare. Eq. 2.19) in HELENA it is possible to set up an iteration loop to realise a certain  $q$  profile [68]. Furthermore the safety factor of a fixed equilibrium can be rescaled to higher or lower values prior to the stability calculation with CASTOR as already described in Sect. 4.2.1.

For the following calculations, the experimental resistivity was estimated by the well known Spitzer formula [69, 2]. This estimate is sufficient in this context. The

growth rates exhibit a slight change with resistivity but the physical mechanisms would not change for a slightly different value.

## 5.3 Double Tearing Modes

### 5.3.1 Experimental Observations

Fig. 5.1 shows the time development of a NBI heated ASDEX Upgrade reversed shear discharge. a shows the central value of the temperature of electrons and ions, b presents the evolution of the safety factor. Passing the rational surface, its minimum value rests for some time at  $q = 2$ . c gives the Mirnov signal for this interval.

It can be seen from the safety factor evolution that the whole  $q$  profile is moving downwards throughout the discharge. As the minimal value of the safety factor approaches 2, the onset of  $n = 1$ ,  $m = 2$  activity can be observed in the Mirnov coils. It starts as fishbone activity<sup>1</sup>. It constitutes the otherwise stable internal kink mode of helicity 2,1 that is driven unstable by the fast ion population arising from additional heating [70]. Afterwards a continuous mode appears at about 0.68 s. It is only transient and disappears again as  $q_{\min}$  falls below 2. In Fig. 5.1-a it can be observed that the continuous mode deteriorates the improved transport and yields a reduction of the central temperatures. The electron temperature is lower because the neutral beams predominately heat the ions and an improved electron confinement does not automatically result in high electron temperatures. Nevertheless the activity is visible in both channels as a temporary drop.

If central ECRH is added to discharges similar to the one described above high continuous electron temperatures ( $T_e \approx T_i \approx 10$  keV) can be achieved as well. An interesting feature is that the  $n = 1$ ,  $m = 2$  instability observed before, is now suppressed. The mode does not appear at all if the ECRH was provided before the expected onset, or disappears as soon as the electron heating is switched on.

### 5.3.2 Identification of the Mode

A stability analysis with CASTOR was done on the reconstructed equilibrium at  $t = 0.72$  s. The most unstable mode found is a  $m = 2$ ,  $n = 1$  resistive mode. The

---

<sup>1</sup>The name accounts for its appearance in the Mirnov signal.



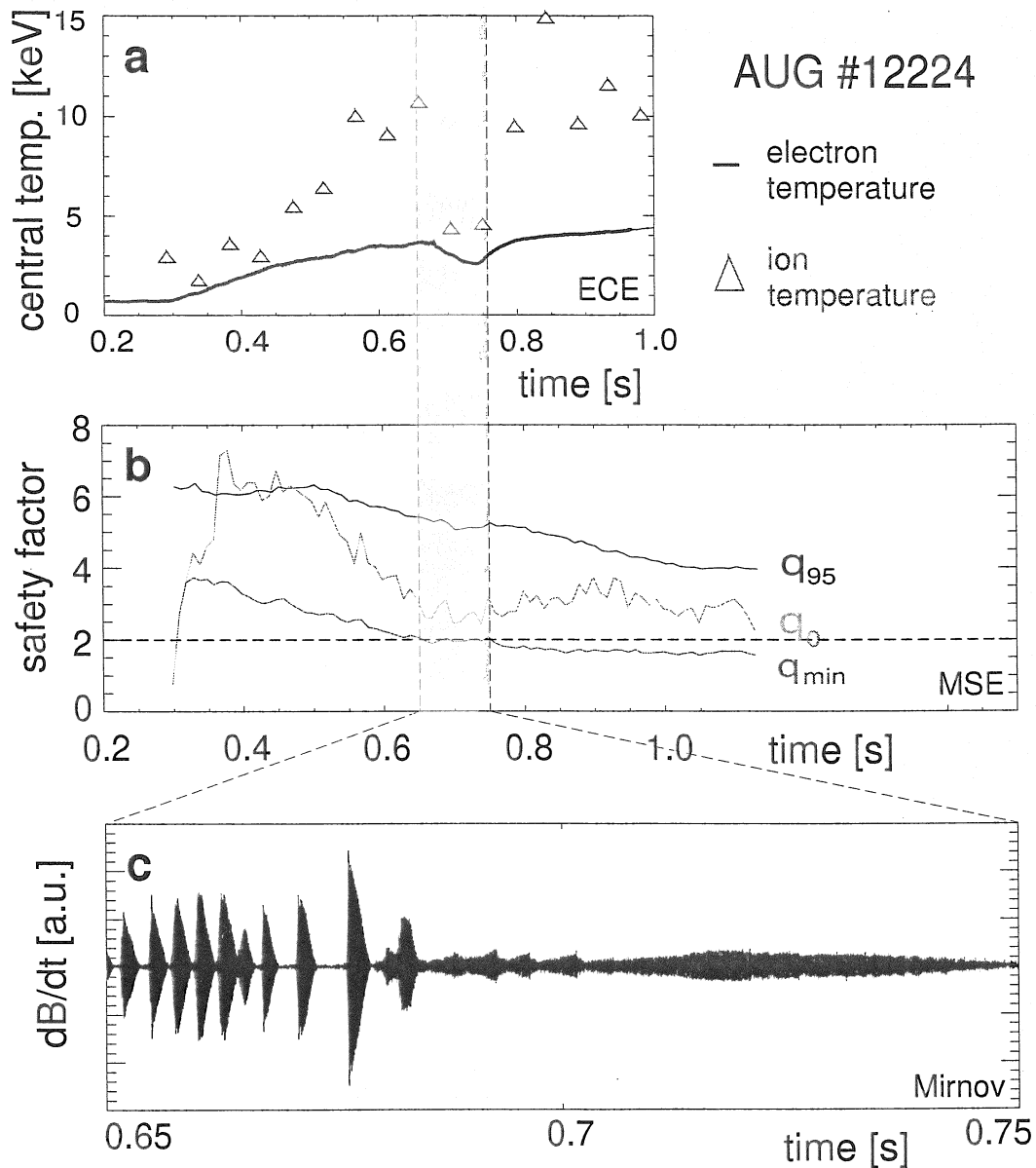


Figure 5.1: The temporal evolution of a purely NBI heated discharge: a shows the central value of the temperature of electrons and ions, measured with the ECE diagnostic, versus time. b presents the evolution of the safety factor on axis ( $q_0$ ), near the edge ( $q_{95}$ ) and in the minimum ( $q_{min}$ ). The minimum value of  $q$  stays fixed for  $\approx 0.1$  s as  $q = 2$  is passed. c gives the Mirnov signal for this time interval, that has also been marked in a and b.

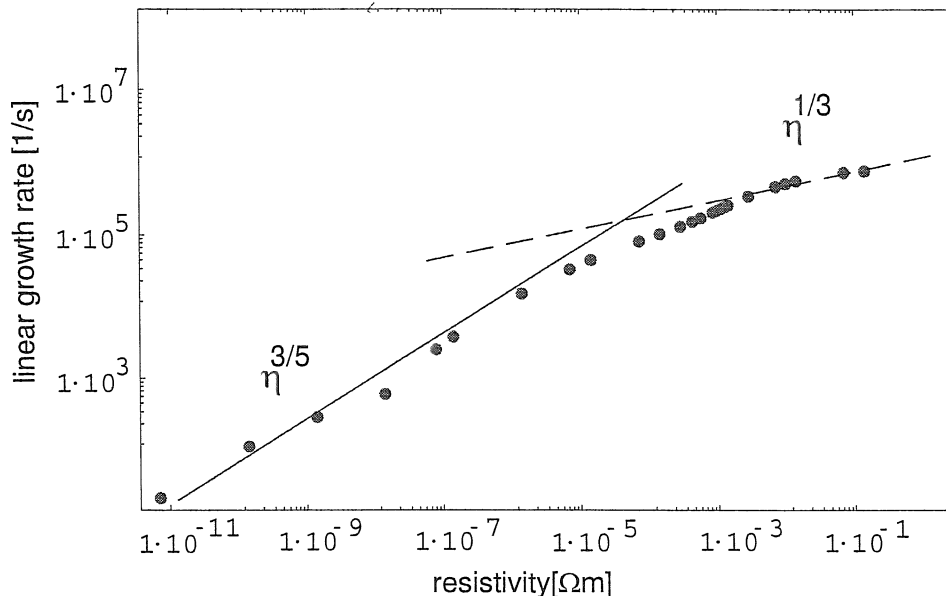


Figure 5.2: Dependence of the linear growth rate of the DTM on resistivity: At low resistivities, single tearing mode scaling ( $\Gamma \propto \eta^{3/5}$ ) is found, whereas for large resistivities DTM scaling ( $\Gamma \propto \eta^{1/3}$ ) applies.

dependence of the growth rate  $\Gamma$  on resistivity  $\eta$  can be seen in in Fig. 5.2. It is characteristic for the DTM. For low resistivities, the coupling between the two rational surfaces is weak, resulting in a single tearing mode scaling ( $\Gamma \propto \eta^{3/5}$ ) [38]. For larger resistivities, the growth rates, DTM scaling ( $\Gamma \propto \eta^{1/3}$ ) [45] applies.

The eigenfunction found with the CASTOR code exhibits two jumps and associates to the typical phase shifted island structure of an evolved DTM, as has already been described in Sect. 4.3.1. A comparison with the eigenfunction derived from the temperature fluctuations measured by ECE is presented in Fig. 5.3. Though the radial range of the diagnostic is limited, there is convincing agreement between the measurement and the linear calculation.

### 5.3.3 Discussion of the Mode Dynamics

It has been stated before that the DTM is associated with a pair of islands, which short circuit the thermal insulation of the nested flux surfaces. The presence of two island chains can thus account for the deterioration of the confinement observed in the central temperatures.

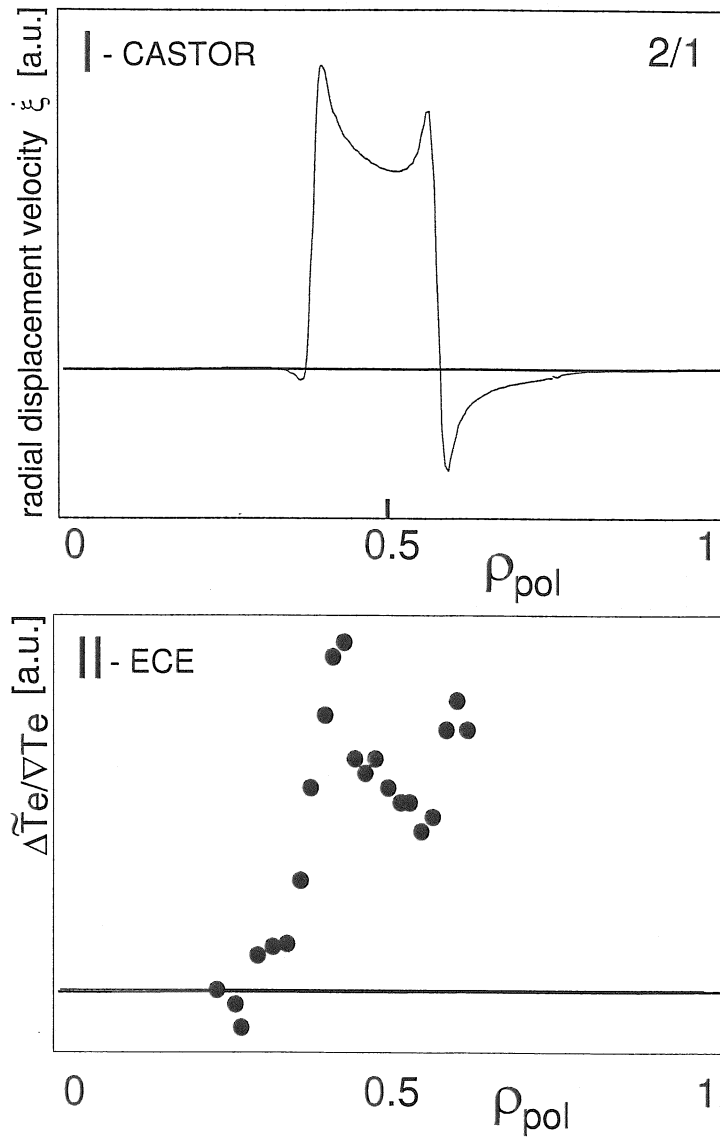


Figure 5.3: Eigenfunction of the 2/1 double tearing mode: I shows the result of a linear stability analysis with CASTOR, II shows the ECE measurement ( $\Delta\tilde{T}_e/\nabla T_e$ ).

To understand the transient character of the mode, calculations have been performed in which the  $q$  profile has been moved up and down to account for the temporal change exhibited by Fig. 5.1-b. In Fig. 5.4 the resulting growth rate has been projected against the minimum value of the safety factor. The DTM is limited to  $q_{min} < 2$  since the rational surfaces have to be present in the plasma. Below  $q = 2$  the growth rate quickly reaches its maximum to be reduced again as the profile is

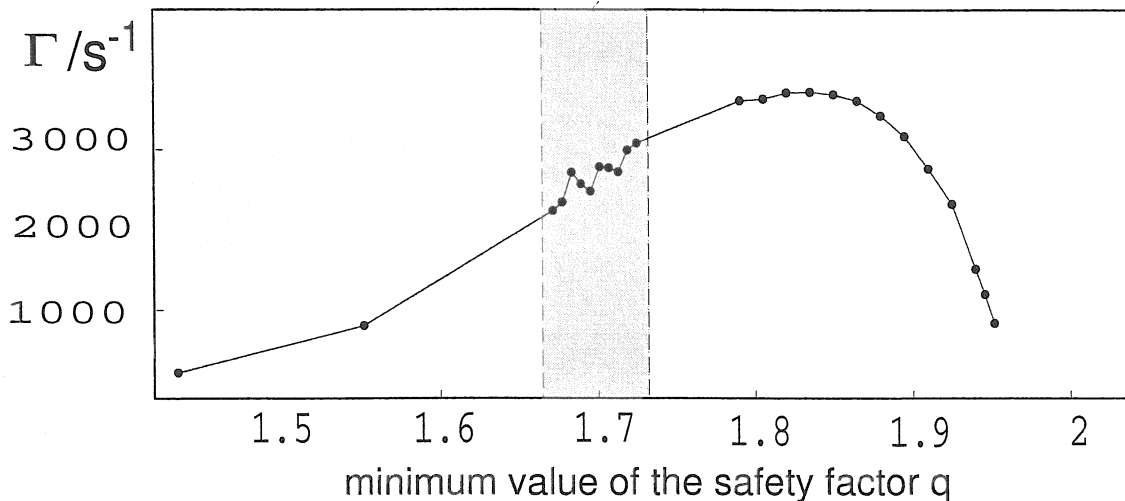


Figure 5.4: Dependence of the DTM growth rate on the minimum value of the safety factor as the profile is scaled up and down. The fluctuation of the growth rate in the shaded area is caused by the coupling to an external mode which appears as the edge value of  $q$  approaches a rational number.

lowered further. The reason for this behaviour is a reduction of the coupling between the two resonant surfaces as their positions are moved apart. The effect has been studied at length for a different case (compare Sect. 4.3.1) and is a general property of the DTM instability.

Performing nonlinear cylinder simulations [47] Q. Yu was able to explain the local clamping of the  $q$  profile by the current diffusion across the island. Thus the safety factor profile is flattened around the minimum implying a growing distance between the islands even for a virtually unchanged value of  $q_{min}$ . In conjunction with this result the transient character of the mode is explained by the calculation: The increasing distance of the rational surfaces spatially decouples the mode.

It has been reported that the DTM has been found to be stable for cases with additional electron heating [36]. The increased temperature accounts for a decreased resistivity at the inner surface, which weakens the resistive mode and could decouple the two island chains. The calculations presented in Fig. 5.5 however did show the effect on the growth rate to be too small to cause the stabilisation in the experiment. An explanation for the observation was given by S. Günter [44]: As the islands in the negative shear region are differently orientated (comp. Fig. 3.5-B) the island

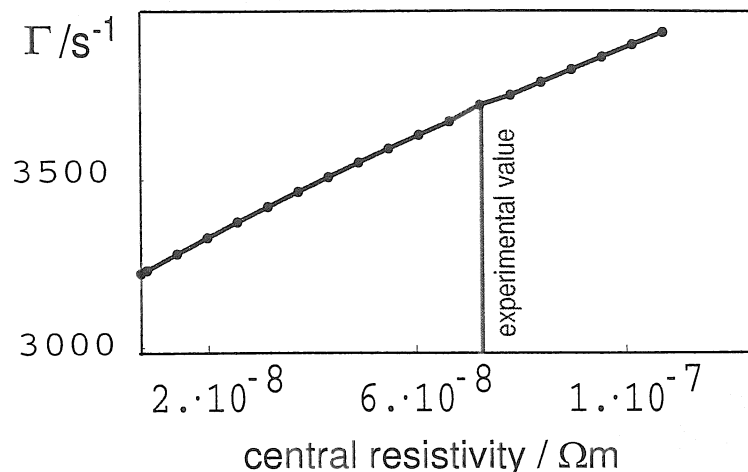


Figure 5.5: The variation of the resistivity at the inner surface does not yield a drastic change of the linear growth rate of the double tearing mode. (Note that the point  $\Gamma = 0$  is suppressed.) Thus the stabilisation in the experiment has to be caused by a different mechanism.

current is flowing in different direction for the inner, than for the outer island chain. thus the bootstrap current yields a stabilisation of the mode in inversion to the destabilisation of single tearing modes found in positive shear (comp. Sect. 3.2.1).

## 5.4 Infernal Modes

### 5.4.1 Experimental Observation

The temporal evolution of the central electron temperature is compared for two heating mechanisms in Fig. 5.6. #12229 was purely NBI heated and exhibits the temporal loss of confinement caused by the DTM, as discussed above. It was reported that this mode is suppressed as ECR heating is switched on [36]. This can be observed in the time trace of the discharge #12224. If the heating however is provided too early, the plasma disrupts (#12458).

Shortly after the steep gradients have been established in the electron channel of #12229 there appear sudden drops of the central temperature indicating an additional MHD instability. It is also of 2/1 helicity, but grows on much faster timescales ( $\tau < 40\mu s$ ) revealing an ideal nature. It does not destroy the transport barrier as the temperature drop at  $t = 1.03$  s is caused by switching off two of the three ap-

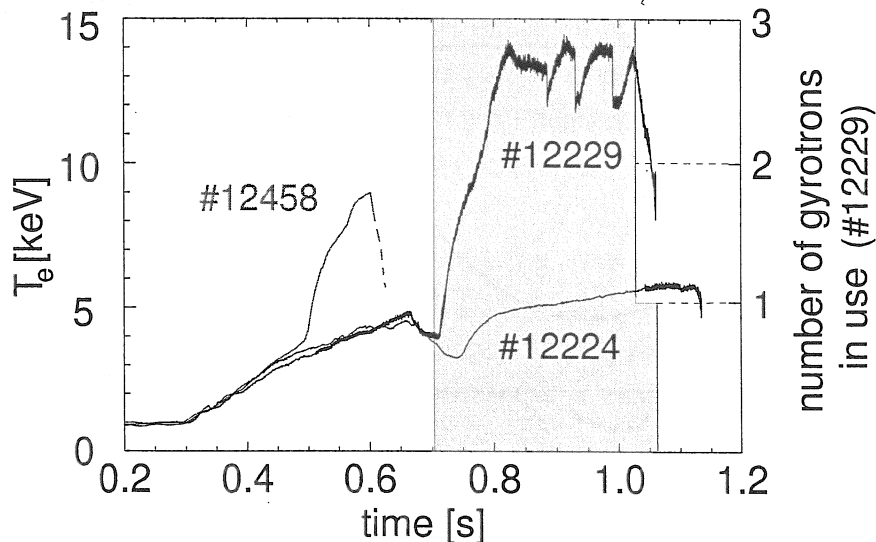


Figure 5.6: The evolution of the central electron temperature measured by ECE for a discharge with NBI heating (#12229) and two with combined NBI and ECRH (#12224 and #12458). It can be seen that fast modes ( $\tau < 40\mu s$ ) set in. If the ECRH is applied early (#12458) they terminate the discharge, if it is applied at later times (#12229) the modes appear repeatedly ( $0.9s < t < 1.1s$ ) without deteriorating the transport barrier or destroying the equilibrium. In #12224 similar activity causes a disruption at  $t \approx 1.1s$ . The shaded area gives the number of gyrotrons in operation during discharge #12229

plied gyrotrons. In discharges with an earlier application of ECRH however the same instability has caused disruptions (e.g. #12458). Also the purely NBI heated shot was terminated by a disruption that was triggered by a closely related activity, analysed in 5.6.

#### 5.4.2 Identification and Discussion

A linear stability analysis has been carried out finding an internal 2/1 mode. Remaining unstable for vanishing resistivity it constitutes an ideal instability.

To further characterise the activity, the equilibrium has been parameterised as indicated in Fig. 5.7-1. The safety factor profile was kept fixed, while the transport barrier in the pressure,  $P$  was modeled by a Gauss distributed pressure gradient ( $dP/d\psi$ ). The setup was varied in two ways:

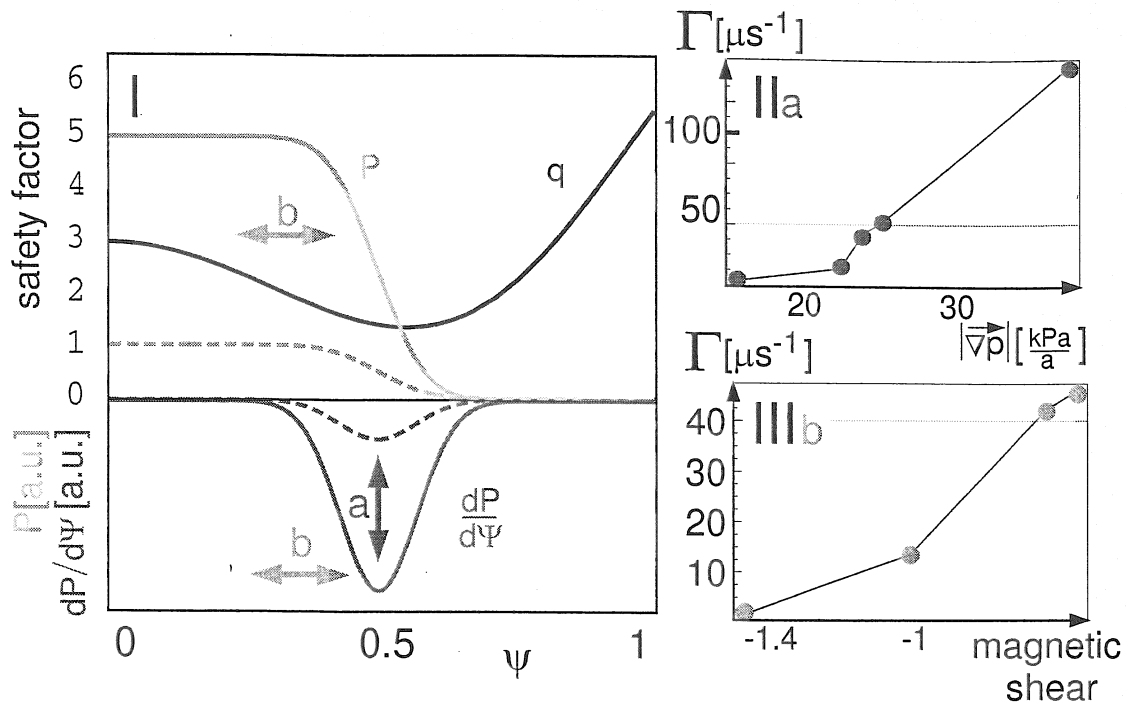


Figure 5.7: I shows the parameterised equilibrium. The pressure gradient ( $dP/d\psi$ ) is presented by a Gauss distribution resulting in the pressure profile,  $P$ . The safety factor profile  $q$  is kept fixed, while the pressure gradient is changed in amplitude and position. II presents the response linear growth rate found with CASTOR to a change in amplitude, III to a change in position, where the abscissa denotes the value of the magnetic shear at the position of the maximal pressure gradient.

- a The pressure gradient was scaled up and down. The resulting growth rate is plotted against the maximum value of the pressure gradient in Fig. 5.7-II. The units of the abscissa are given in kPa per minor radius ( $a$ ). As mentioned above, ASDEX Upgrade transport barriers exhibit even higher values ( $\approx 100$  kPa/ $a$ ).
- b The centre of the Gauss distribution has been shifted radially keeping the normalised plasma pressure constant. Thus the magnetic shear at the maximum pressure gradient has been varied. Fig. 5.7-III projects response of the linear growth rate to this change.

The scan shows that the mode is ideal and pressure gradient driven, and depends on the magnetic shear. This agrees with the experiment: The mode has been observed either shortly after the additional heating was established (e.g. #12458) or at

later times, when the current diffusion has flattened the  $q$  profile implying a lower magnetic shear (e.g. #12229). The growth rate that associates to the experimental timescale has been marked in Fig. 5.7-II-III with horizontal lines. These characteristics identify the mode as the infernal mode, described in Sect. 3.2.5.

The examinations have shown the mode to be most dangerous, when high pressure gradients coincide with low shear. Therefore it should be avoided to have rational surfaces close to the low shear region in the plasma. Since this can not be realised with the non stationary experimental profiles it is of interest to avoid very high pressure gradients in the low shear region. At this point MHD activity might prove to have an advantageous side. It can be seen in Fig. 5.6 how #12229 is suffering from low amplitude activity in the time interval  $0.9\text{ s} < t < 1.1\text{ s}$ . It neither destroys the transport barrier, nor causes a disruption. The result of this activity is the desired limitation of the pressure gradient in the most crucial region. Without this activity the gradients steepen further causing a stronger mode, resulting in a disruption (e.g. #12458).

Thus MHD can contribute to the attainment of quasistationary discharge conditions. This positive feedback is well known for other instabilities. For example, the  $m = 1$ ,  $n = 1$  fishbone prevents the accumulation of impurities in the centre and ELMs (Edge Localised Modes) limit edge gradients in a similar way. Therefore it is advisable to continue the experiments and explore how to control the infernal mode with central heating.

## 5.5 External Kink Modes

### 5.5.1 External Kink Modes Limit $\beta_N$ in Advanced Scenarios

It has already been pointed out in the introduction that a high value of  $\beta_N$  is essential for the steady state tokamak concept. As this parameter depends on the averaged pressure (see Eq. 1.8) it is of advantage to extend the domain of high pressure by pushing the  $q$  minimum and the associated transport barrier outward. Unfortunately such a change gives rise to external kink modes.

Fig. 5.8 illustrates the problem. A represents an ASDEX Upgrade like equilibrium. Using HELENA, a series of equilibria has been calculated. As seen they



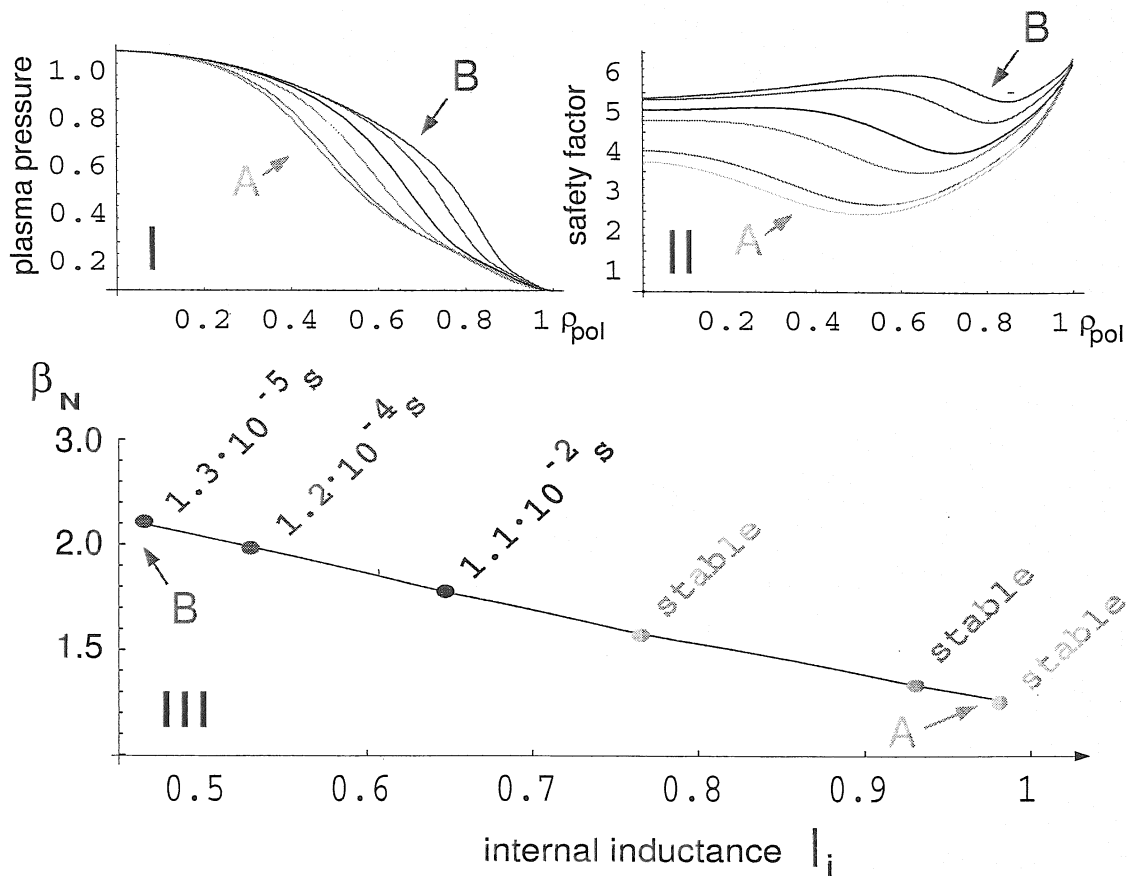


Figure 5.8: The ASDEX Upgrade like equilibrium A has been changed into the model equilibrium B, by pushing the ITB and the associated  $q$  minimum outward. This gives rise to external kink modes of increasing growth rate. I presents the transition between A and B in the pressure, II in the safety factor profiles. The resulting increase in  $\beta_N$  is associated with a drop of the internal inductance as can be seen in III. The times given in this diagram are growth times of the external kink modes.

constitute a successive transition to the model equilibrium B. During this change, the minimum structure in the safety factor has been pushed out as seen in Fig. 5.8-II. As the edge value of  $q$  constitutes a crucial parameter for kink stability (compare Sect. 3.2.3), it has been kept fixed during the transition. The domain of high pressure gradients has been pushed to higher values of  $\rho_{pol}$  correspondingly (Fig. 5.8-I). Technically the transition was achieved rescaling the input profiles of the equilibrium calculation. The (bootstrap-)current is thus not self-consistently derived from the pressure profile.

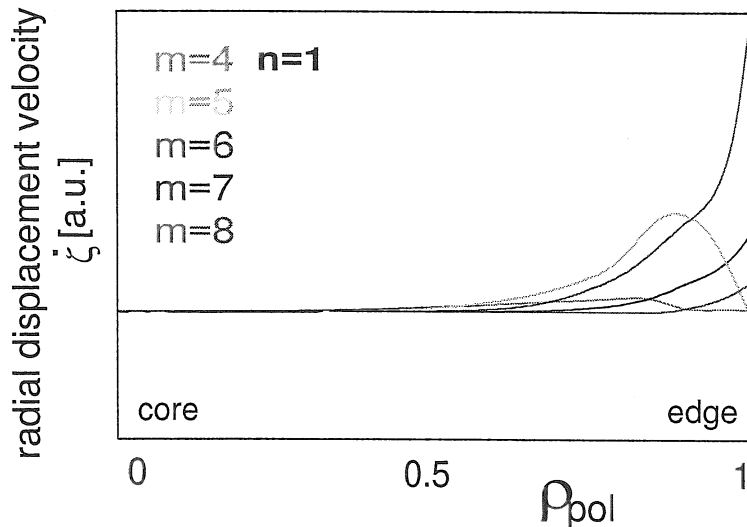


Figure 5.9: CASTOR calculations show, that the equilibrium B is unstable to the external kink mode. The most prominent of 15 contributions to the eigenfunction for the radial displacement velocity,  $\dot{\xi}$ , have been projected. The mode activity is localised at the plasma surface.

The resulting increase in  $\beta_N$  can be seen from the diagram below (Fig. 5.8-III). A more pronounced internal transport barrier would yield an even bigger gain. As the safety factor profile is linked to the current distribution the change reduces the equilibrium's internal inductance ( $l_i$ ) substantially. It is found that this drives external kinks of the helicity ( $m = 6, n = 1$ ) unstable. The growth time of the mode is denoted on the diagram. While the first equilibria are stable, there appears an instability of increasing growth rate as the ITB is pushed outward. Thus the external kink mode constitutes an obstacle for the increase of  $\beta_N$ .

### 5.5.2 Wall Stabilisation

The eigenfunctions of the external kink mode arising in equilibrium B are projected in Fig. 5.9. The eigenfunctions exhibit a strong peaking at the edge. The associated flux perturbation at the edge would not be possible in the presence of an ideal conducting shell at the plasma surface, therefore the modes can only be found, if a vacuum region between wall and plasma is accounted for. A conducting structure of finite resistivity would slow down the mode growth to the penetration time of the wall. The process is described by Eq. 2.14 and realistic parameters result in a

wall time of the order of milliseconds [7]. On these timescales a control by an active feedback system is possible.

In reality the stabilising structure is limited by geometrical constraints. Heating and diagnostics need access to the plasma and a direct contact stabilising wall with the plasma would lead to a pollution with sputtered impurities. Therefore the influence of a partial wall and the dependence of the stabilisation on the size and distance has been examined for the geometry of the ASDEX Upgrade wall.

The kink unstable equilibrium B has been analysed using 15 poloidal Harmonics. The plasma is surrounded by a vacuum region, which is bounded by the mechanical structure of the vacuum vessel and the Passive Stabilisation Loop (PSL). In addition the yellow shaded stabilising structure has been put on the mid-plane of the low-field-side, while the toroidal symmetry is preserved. Prior calculations have shown that the kink mode is most sensible to a stabilisation at this point, which results from the "bad curvature" discussed in Sect. 3.2.4. Modes of ballooning nature are therefore localised here. Although the kink instability is primarily current gradient driven, it will be enhanced by any negative contribution to the energy functional  $\delta W$  (compare Eq. 2.39). The poloidal width of the structure and the distance from the plasma have been varied.  $\alpha$  is defined as the poloidal angle spanned by the partial wall, so  $\alpha = 360^\circ$  indicates a closed shell. The distance to the plasma is characterised by a factor  $d$ , where  $d/a = 1$  is equivalent to a structure in direct contact to the plasma. The shape of the partial wall agrees with the one of the plasma boundary, just scaled up by  $d$ .

Fig. 5.10-II shows the stabilisation provided by a closed shell in dependence of the distance. It can be seen that a wall close to the plasma surface prevents the growth. Fig. 5.10-I confirms, that the activity is centred on the low-field-side, so the stabilisation is most effective there. As the poloidal range taken up by the partial wall reaches the Stabilisation loops the stabilising effect saturates as can be seen by comparison with the point at  $d/a = 1.1$  in Fig. 5.10-II. The work has been continued in a Diploma-thesis by P. Lauber [71], where it was shown, that the rapid transition between stability and instability in Fig. 5.10-I reflects that at a certain point the mode does not fit between the wall segments anymore. Also more complicated arrangements like several segmented partial walls and a non toroidally symmetric arrangement have been considered.

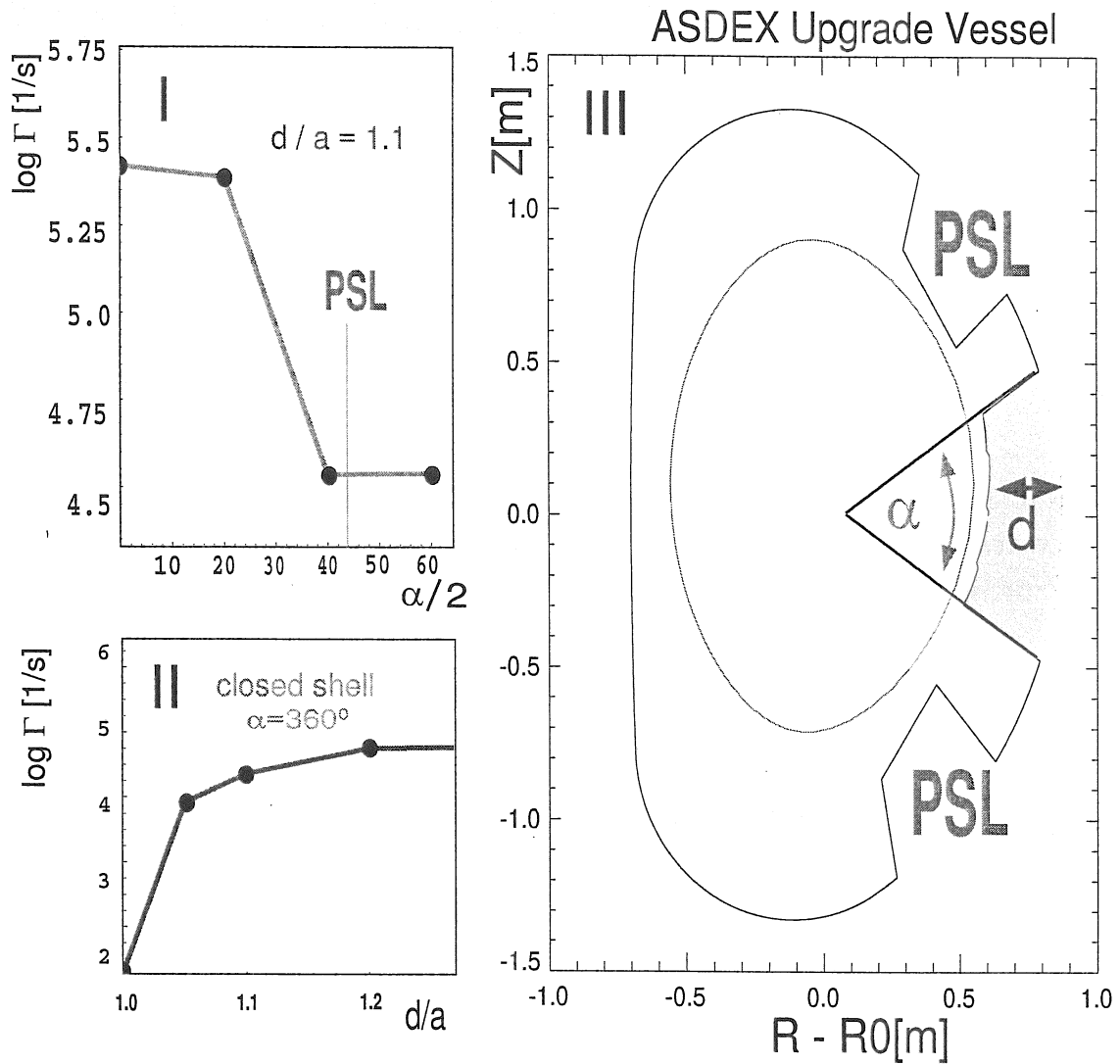


Figure 5.10: Dependence of the external kink growth rate on the presence of a stabilising structure: III shows the plasma boundary, the vacuum region and the perfectly conducting wall. The general shape complies with the ASDEX Upgrade geometry. How the stability changes if the shaded structure is put near to the plasma has been studied. Its shape is defined by the plasma boundary, but scaled by a factor of  $d$ , so that  $d/a = 1$  is equivalent to a structure in direct contact to the plasma. II shows the reaction of the growth rate to a change in  $d$  for the case of a poloidally closed shell. As the modes turn out to be most sensible to a stabilisation on the mid-plane of the low field side, the structure is centred around this poloidal angle. The angle spanned by the structure ( $\alpha$ ) has been changed as well. The reaction of the growth rate on a variation of  $\alpha$  with is projected in I. (PSL denotes the mechanical structure of the “Passive Stabilisation Loop”)

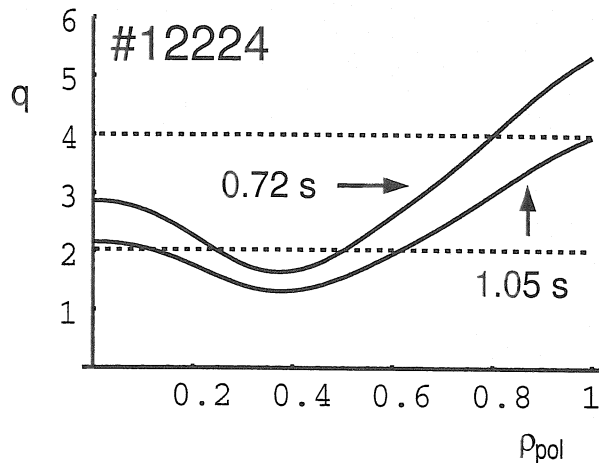


Figure 5.11: The safety factor profile of the discharge #12224 at two times, as reconstructed with CLISTE. The first time point ( $t = 0.72$  s) was during the DTM activity, the second ( $t = 1.05$  s) was shortly before the disruption.

## 5.6 Coupling Between Kink and Infernal Modes

As already pointed out above, the plasma not only disrupts in the case of early auxiliary heating. Also in the purely NBI heated shot #12224 shown in Fig. 5.6, a fast growing mode was observed which locked to the wall and caused a disruption about 10 ms after its onset. This behaviour is characteristic and typically appears for  $t > 1$  s and  $q_{95}$  close to a rational value.

Fig. 5.11 compares the  $q$  profile shortly before the disruption to the one at an earlier time, which has been analysed in Sect. 5.3. Both profiles are taken from the CLISTE equilibrium reconstruction, including data from the MSE diagnostic. At the time  $t = 0.72$  s, the equilibrium was found to be unstable to the DTM, at  $t = 1.05$  s, the rational surfaces are further apart, the shear is lower and the edge value of the safety factor is approximately 4.

It has already been shown that low shear is favourable for the growth of infernal modes and a low order rational value of  $q$  enables external modes to develop. The ECE measurement of the temperature fluctuations confirms these suggestions. Fig. 5.12 compares the measurement with the structure of the eigenfunctions found in a linear stability analysis with CASTOR and exhibits good agreement.

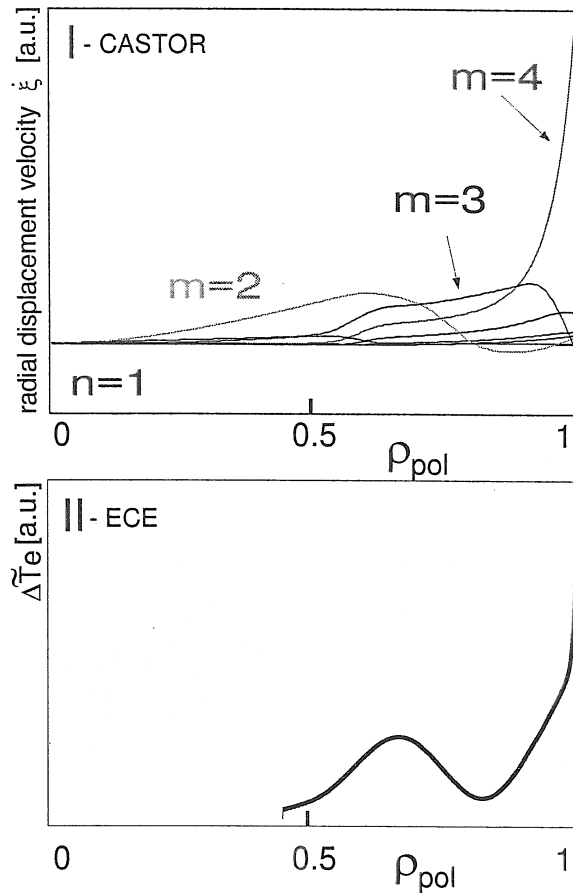


Figure 5.12: The mode structure exhibits a good agreement between calculation and measurement I: Eigenfunction of the displacement velocity  $\dot{\xi}$ , as given by the CASTOR code. It can be seen, that the external kink mode ( $m = 4$ ) couples with the infernal mode ( $m = 2$ ) through the intermediate  $m = 3$  component. II: An ECE measurement of the Temperature fluctuations immediately before a disruption. The contributing poloidal mode numbers can not be separated.

The calculated eigenfunctions (Fig. 5.12-I) reveal the coupling mechanism: The  $m = 4$ ,  $n = 1$  external kink modes couples to the  $m = 2$ ,  $n = 1$  infernal mode through the intermediate  $m = 3$ ,  $n = 1$  component. The external part is essential for the observed locking to the wall and the subsequent disruption.

The described activity illustrates the importance of a wall stabilisation not only for future plasma with higher  $\beta_N$ , but also for experiments nowadays.

# Chapter 6

## Summary and Conclusion

### 6.1 The Work Contributed to an Understanding of the Experiments

The linear calculations with the resistive MHD code CASTOR did contribute to an interpretation of the observations at two tokamaks.

#### 6.1.1 TEXTOR-94

The activity responsible for the internal disruptions in TEXTOR-94 reversed shear scenarios has been identified as a set of coupled Double Tearing modes (DTMs) of the helicities  $2/1$  and  $3/2$ , each of which modes being associated with two island chains.

- The equilibrium has been shown to be susceptible to this instability for a wide range of parameters.
- During the crash changes were observed in the experiment. They can be explained by the presence of various possibly overlapping island chains:
  - The loss of confinement (comp. Fig. 4.1) results from the improved transport across the islands.
  - The change of the safety factor profile (comp. Fig. 4.3) can be explained by the enhanced current diffusion across the islands.

The stabilisation by the Neutral Beam Injection (NBI) found in the experiment is explained by the rotation imposed on the plasma by this heating mechanism.

Since the differential rotation in the experiment (comp. Fig. 4.4) exceeds a distance-dependent threshold (comp. Fig. 4.16), the differential movement of the bulk plasma forces the two island chains to unlock. The unlocked island chains move against each other without adopting a fixed phase. In agreement with theory it is found that this prevents the mutual coupling of the two tearing modes and thus yields a reduction of the linear growth rate (comp. Fig. 4.18).

The diagnostics cannot tell, whether the mode disappears for the NBI discharges or whether its amplitude is just reduced preventing the islands to overlap. The calculations suggest a continuing activity, but it has to be pointed out, that it relies on the equilibrium properties measured by the diagnostics. A future comparison would be of interest.

### 6.1.2 ASDEX Upgrade

The bootstrap current in current reversed shear experiments is not sufficient to obtain a stationary current profile. Therefore ASDEX Upgrade advanced scenarios exhibit a temporally changing profile of the safety factor  $q$ . As it changes, the discharges suffer from a range of MHD activities. They deteriorate the internal transport barrier (ITB) or even cause disruptions, terminating the discharges. Various shots have been analysed and different instabilities have been found.

**Double Tearing Mode:** As the minimum of the non monotonic  $q$  profile is reaching the value 2, an activity can be observed for a time interval of  $\approx 0.1s$ . It could be identified as a 2/1 DTM. The reason for the mode's transient character is the decoupling of the two islands by the increasing distance of the rational surfaces as  $q$  is lowered. Comparing the code output with the measurement, there is convincing agreement found in the mode structure (comp. Fig. 5.3). The measured decrease of the electron temperature and the transient destruction of the transport barrier are ascribed to parallel transport across the island. It was shown, that the reduction of the central plasma resistivity does not affect the DTM growth enough to explain the experimentally observed stabilisation of the mode by central radiative heating. (The observation was explained with neoclassical theory by S. Günter [44].)



**External Kink Mode:** To gain access to plasmas with a higher volume averaged pressure it is desirable to shift the ITB outwards. It is shown, that this change drives external kink modes unstable. External modes would couple to the wall and result in disruptions, therefore this activity limits the achievable pressure and presents an obstacle for further progress of the advanced scenarios.

To overcome this limitation it has been proposed to put a conducting structure in the vicinity of the plasma surface. A closed, perfectly conducting shell would stabilise external modes completely, but in reality one is restricted to a partial wall at a finite distance to the plasma surface. The expected stabilisation yielded by such an arrangement has been calculated.

**Infernal Mode:** A fast ( $\tau < 40\mu s$ ), and therefore ideal activity which can lead to disruptions was observed in the experiment. A model equilibrium has been found to be unstable to an ideal instability, which is pressure driven and depends on the magnetic shear. The instability is identified as an infernal mode. It is pressure driven and can cause the plasma to disrupt.

**Coupled Infernal and Kink Mode:** In shots without the additional heating the DTM did appear transiently. In a later phase, disruptions have been observed. They occur as the shear is weakened by current diffusion (comp. Fig. 5.11) and as the edge value of the safety factor approaches rational values. The shear dependence suggests the influence of an infernal mode and the rational  $q_{edge}$  indicates the influence of an external mode. The analysis has shown the plasma to suffer from a combination of Infernal and Kink Mode. As already in the case of DTMs, there is an impressive agreement of the mode structure found between the ECE measurement and the code output. It has therefore been shown that even current ASDEX Upgrade plasmas disrupt due to external modes. This stresses the importance of wall stabilisation for experiments nowadays.

## 6.2 One can Recomend Strategies to Avoid Activities

MHD instabilities present a challenge for future experiments devoted to a progress in the advanced tokamak concept. On the basis of the presented work recomendations

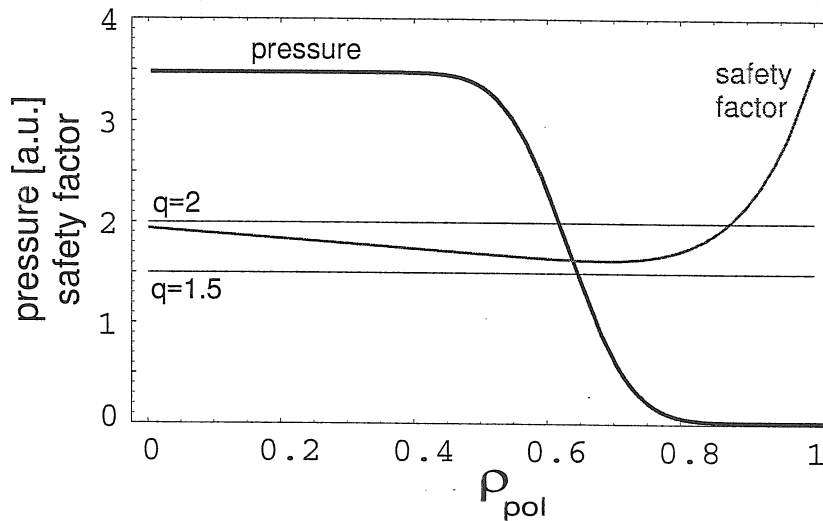


Figure 6.1: Optimised profiles for safety factor and pressure. There is no  $q = 1.5$  surface and only one  $q = 2$  surface in the plasma (1). The remaining one is located where the pressure gradient is low (4). If it is not possible, to keep the safety factor below 2 on axis the rational surfaces should be far apart (2).  $q_{min}$  and the associated ITB are far outside (5) and not coinciding with a rational surface (3).

for the design of optimised profiles (Fig. 6.1) can be given.

1. As far as possible, low  $n$  rational  $q$  profiles should be avoided (in particular  $2/1$  and  $3/2$ ).
2. If double rational surfaces  $q = 2$  cannot be avoided in the plasma, they should be far apart to weaken the coupling of a DTM. The presence of a sheared rotation can be advantageous to unlock and decouple the islands.
3. The minimum in the safety factor and the associated transport barrier present a crucial arrangement for the infernal mode. Therefore this structure should be kept away from low order rationals.
4. The outer rational surface (positive shear) should be at a radial position, where the pressure gradient is low. This excludes the neoclassical drive of the outer island that would further destabilise a DTM.
5. The ITB should be as far out as possible to obtain a high  $\beta_N$ . Since this can give rise to External Kink Modes wall stabilisation might be necessary.

# Bibliography

- [1] N.P. Taylor, I. Cook, R.A. Forrest, C.B.A. Forty, W.E. Han, and D.J. Ward. The safety, environmental and economic implications of the use of silicon carbide in fusion power plant blankets. *27<sup>th</sup> Symposium on Fusion Technology, Madrid*, 2000.
- [2] J. Wesson. *Tokamaks*. Oxford Science Publications, 1997.
- [3] *Overview of Recent Experimental Results From The DIII-D Advanced Tokamak Program*, 2000.
- [4] M. Greenwald, J.L. Terry, S.M. Wolfe, S. Ejima, M.G. Bell, S. M. Kaye, and G. H. Neilson. A new look at density limits in tokamaks. *Nuclear Fusion*, 1988.
- [5] ITER Physics Basis editors, ITER Physics Expert Group Chairs and Co-chairs, ITER Joint Central Team, Physics Integration Unit, and ITER EDA Naka Joint Work Side. ITER physics basics. *Nuclear Fusion*, 1999.
- [6] A.G. Peeters. The bootstrap current and its consequences. *Plasma Physics and Controlled Fusion*, 2000.
- [7] J.P. Freidberg. *Ideal Magnetohydrodynamics*. Plenum Press, 1987.
- [8] J.D. Jackson. *Classical Electrodynamics*. John Wiley & Sons, 1975.
- [9] *Conference of Computational Physics*, 1990.
- [10] E.J. Strait, L.L. Lao, M.E. Mauel, B.W. Rice, T.S. Taylor, K.H. Burrell, M.S. Chu, and E.A. Lazarus. Enhanced confinement and stability in DIII-D discharges with reversed magnetic shear. *Physical Review Letters*, 1995.
- [11] S.D. Pinches. *Nonlinear Interaction of Fast Particles with Alfvén Waves in Tokamaks*. PhD thesis, University of Nottingham, 1996.

- [12] S.D. Pinches, L.C. Appel, J. Candy, S.E. Shapapov, H.L. Berk, D. Borba, B.N. Breizman, T.C. Hender, K.I. Hopcraft, G.T.A. Huysmans, and W. Kerner. The HAGIS self-consistent nonlinear wave-particle interaction model. *Computer Physics Communications*, 1998.
- [13] D. Biskamp. *Nonlinear Magnetohydrodynamics*. Cambridge University Press, 1993.
- [14] W. Kerner, J.P. Goedbloed, G.T.A. Huysmans, S. Poedts, and E. Schwartz. CASTOR: Normal-mode analysis of resistive MHD plasmas. *Computational Physics*, 1998.
- [15] M.S. Chu, J.M. Greene, T.H. Jensen, R.L. Miller, A. Bondeson, R.W. Johnson, and M.E. Mauel. Effect of toroidal plasma flow and flow shear on global magnetohydrodynamic modes. *Physics of Plasmas*, 1995.
- [16] E. Strumberger, H.P. Zehrfeld, S. Günter, and ASDEX Upgrade Team. Damping of double tearing modes by differential plasma rotation. *27<sup>th</sup> EPS Conference on Controlled Fusion and Plasma Physics, Budapest, 2000*.
- [17] H.P. Zehrfeld. Dissipative magnetohydrodynamic equilibria with compressible fluid flow. *27<sup>th</sup> EPS Conference on Controlled Fusion and Plasma Physics, Budapest, 2000*.
- [18] M. Bessenrodt-Weberpals and al. The multiple facets of ohmic confinement in ASDEX. *Nuclear Fusion*, 1991.
- [19] R.J. Goldston. Energy confinement scaling in tokamaks: Some implications of recent experiments with ohmic and strong auxiliary heating. *Plasma Physics and Controlled Fusion*, 1984.
- [20] F. Wagner and al. Regime of improved confinement and high beta in neutral-beam-heated divertor discharges of the ASDEX tokamak. *Physical Review Letters*, 1982.
- [21] Ida et al. Collisional H-mode at JFT. *Physical Review Letters*.
- [22] J.M. Greene and M.S. Chance. The second region of stability against ballooning modes. *Nuclear Fusion*, 1981.

- [23] E.J. Synakowski. Formation and structure of internal and edge transport barriers. *Plasma Physics and Controlled Fusion*, 1998.
- [24] G.M. Staebler. Theory of internal and edge transport barriers. *Plasma Physics and Controlled Fusion*, 1998.
- [25] C.L. Rettig, K.H. Burrell, B.W. Stallard, G.R. McKee, G.M. Staebler, T.L. Rhodes, C.M. Greenfield, and W.A. Peebles. Dynamics of core transport barrier formation and expansion in the DIII-D tokamak. *Physics of Plasmas*, 1998.
- [26] K.H. Burrell. Effects of  $\mathbf{E} \times \mathbf{B}$  velocity shear and magnetic shear on turbulence transport in magnetic confinement devices. *Physics of Plasmas*, 1997.
- [27] J. Manickam, N. Pomphrey, and A.M.M. Todd. Ideal MHD stability properties of pressure driven modes in low shear tokamaks. *Nuclear Fusion*, 1987.
- [28] T. Ozeki, M. Azumi, S. Tokuda, and S. Ishida. Effects of a hollow current profile on the ideal MHD stability of high  $\beta_{pol}$  plasmas in a tokamak. *Nuclear Fusion*, 1993.
- [29] R. Fitzpatrick. On the stability of equilibria with unorthodox  $q(r)$  profiles to the resistive internal kink mode. *Plasma Physics and Controlled Fusion*, 1989.
- [30] B.B. Kadomtsev. Plasma instability due to particle trapping in a toroidal geometry. *Soviet Physics JETP*, 1967.
- [31] R.J. Goldston, S.H. Batha, R.H. Bulmer, D.N. Hill, A.W. Hyatt, S.C. Jardin, F.M. Levinton, S.M. Kaye, C.E. Kessel, E.A. Lazarus, J. Manickam, G.H. Neilson, W.M. Nevins, L.J. Perkins, G. Rewoldt, K.I. Thomassen, M.C. Zarnstorff, and the NTPX Physics Team. Advanced tokamak physics - status and prospects. *Plasma Physics and Controlled Fusion*, 1994.
- [32] B.W. Rice, T.S. Taylor, K.H. Burrell, T.A. Casper, C.B. Forest, H. Ikezi, L.L. Lao, E.A. Lazarus, M.E. Mauel, B.W. Stallard, and E.J. Strait. The formation and evolution of negative central magnetic shear current profiles on DIII-D. *Plasma Physics and Controlled Fusion*, 1996.
- [33] Hugon et al. Shear reversal and MHD activity during pellet enhanced performance pulses in JET. *Nuclear Fusion*, 1992.

- [34] F.M. Levinton, M.C. Zarnstorff, S.H. Batha, M. Bell, R.E. Bell, R.V. Budny, C. Bush, Z. Chang, E. Fredrickson, A. Janos, J. Manickam, A. Ramsey, S.A. Sabbagh, G.L. Schmidt, E.J. Synakowski, and G. Taylor. Improved confinement with reversed magnetic shear in TFTR. *Physical Review Letters*, 1995.
- [35] T. Fujita and the JT-60 Team. High-performance experiments towards steady-state operation in jt-60u. *Plasma Physics and Controlled Fusion*, 1997.
- [36] R. Wolf, S. Günter, F. Leuterer, A. Peeters, G. Pereverzev, O. Gruber, M. Kaufmann, K. Lackner, M. Maraschek, P.J. Mc Carthy, H. Meister, H. Salzmann, S. Schade, J. Schweinzer, W. Sutrop, and ASDEX Upgrade Team. Response of internal transport barriers to central electron heating and current drive on ASDEX Upgrade. *Physics of Plasmas*, 2000.
- [37] H.R. Koslowski, G. Fuchs, A. Krämer-Flecken, J. Rapp, and TEXTOR 94 Team. Characteristics of the q profile for different confinement conditions on TEXTOR-94. *Plasma Physics and Controlled Fusion*, 1997.
- [38] H.P. Furth, J. Killeen, and M.N. Rosenbluth. Finite-resistivity instabilities of a sheet pinch. *Physics of Fluids*, 1963.
- [39] H.P. Furth, P.H. Rutherford, and H. Selberg. Tearing mode in the cylindrical tokamak. *Physics of Fluids*, 1973.
- [40] A.H. Glaser, J.M. Greene, and J.L. Johnson. Resistive instabilities in general toroidal plasma configurations. *Physics of Fluids*, 1975.
- [41] R.J. Hastie, A. Sykes, M. Turner, and J.A. Wesson. Stabilization of tearing modes in tokamaks. *Nuclear Fusion*, 1977.
- [42] J.M. Finn. Coupling of tearing modes in tokamaks. *Physics of Fluids*, 1977.
- [43] Z. Chang, J.D. Callen, E.D. Fredrickson, R.V. Budny, C.C. Hegna, K.M. McGuire, M.C. Zarnstorff, and TFTR group. Observation of nonlinear neo-classical pressure-gradient-driven tearing modes in TFTR. *Physical Review Letters*, 1995.
- [44] S. Günter, S. Schade, M. Maraschek, S.D. Pinches, E. Strumberger, R. Wolf, Q. Yu, and ASDEX Upgrade Team. MHD phenomena in reversed shear discharges on ASDEX Upgrade. *Nuclear Fusion*, 2000.

- [45] P.L. Pritchett, Y.C. Lee, and J.F. Drake. Linear analysis of the double-tearing mode. *Physics of Fluids*, 1980.
- [46] J.W. Connor, S.C. Cowley, R.J. Hastie, T.C. Hender, A. Hood, and T.J. Martin. Tearing modes in toroidal geometry. *Physics of Fluids*, 1988.
- [47] Qingquan Yu. Nonlinear growth of the double tearing mode. *Physics of Plasmas*, 1996.
- [48] R.L. Dewar and M. Persson. Coupled tearing modes in plasmas with differential rotation. *Physics of Fluids*, 1993.
- [49] Y. Nishimura, Callen J.D., and C.C. Hegna. Tearing mode analysis in tokamaks, revised. Technical report, Department of Engineering Physics, University of Wisconsin-Madison, 1997.
- [50] M. Persson, R.L. Dewar, and E.K. Maschke. Nonlinear self-reinforced growth of tearing modes with multiple rational surfaces. *Physics of Fluids*, 1993.
- [51] A.M.M. Todd, M.S. Chance, J.M. Greene, R.C. Grimm, J.L. Johnson, and J. Manickam. Stability limitations for high-beta tokamaks. *Physical Review Letters*, 1977.
- [52] J.W. Connor, R.J. Hastie, and J.B. Taylor. High mode number stability of an axisymmetric toroidal plasma. *Proc. R. Soc. Lond.*, 1979.
- [53] H.A. Holties. *Magnetohydrodynamic analysis of fusion plasmas*. PhD thesis, Universiteit Utrecht, 1996.
- [54] H.R. Koslowski, E. Graffmann, S. Günter, J. Rapp, and S. Schade. Investigation of internal disruptions in reversed shear plasmas on TEXTOR-94. *submitted to Nuclear Fusion*, 2001.
- [55] H.R. Koslowski and H. Soltwisch. Electron density and  $q$  profile measurements with the far-IR interferometer-polarimeter on the TEXTOR tokamak. *Fusion Engineering and Design*, 1997.
- [56] J. Rapp, M.Z. Tokar, L. Könen, H.R. Koslowski, G. Bertschinger, M. Brix, H. Claassen, R. Jaspers, A. Krämer-Flecken, K. Ohya, V. Philipps, A. Pospieszczyk, U. Samm, T. Tanabe, G. Telesca, B. Unterberg, and G. van

- Oost. Transport studies of high-z elements in neon edge radiation cooled discharges in TEXTOR-94. *Plasma Physics and Controlled Fusion*, 1997.
- [57] H.R. Koslowski, G. Fuchs, A. Krämer-Flecken, J. Rapp, and the TEXTOR-94 team. Characteristics of the  $q$  profile for different confinement conditions on TEXTOR-94. *Plasma Physics and Controlled Fusion*, 1997.
- [58] P.H. Rutherford. Nonlinear growth of the tearing mode. *Physics of Fluids*, 1973.
- [59] Q. Yu. private communication.
- [60] R. Fitzpatrick, R.J. Hastie, T.J. Martin, and C.M. Roach. Stability of coupled tearing modes in tokamaks. *Nuclear Fusion*, 1993.
- [61] M.S. Chu, L. Chen, L.-J. Zheng, C. Ren, and A. Bondeson. Effect of rotation on ideal and resistive MHD modes. *Nuclear Fusion*, 1999.
- [62] S.C. Cowley and R.J. Hastie. Electron diamagnetism and toroidal coupling of tearing modes. *Physics of Fluids*, 1988.
- [63] Q. Yu and S. Günter. Numerical modeling of neoclassical double tearing modes. *Nuclear Fusion*, 1999.
- [64] M. Sokoll. MHD-Instabilitäten in magnetisch eingeschlossenen Plasmen und ihre tomographische Rekonstruktion im Röntgenlicht. Technical report, Max Planck Institut für Plasmaphysik, 1997.
- [65] H.J. Hartfuss, T. Geist, and M. Hirsch. Heterodyne methods in millimetre wave plasma diagnostics with applications to ece, interferometry and reflectometry. *Plasma Physics and Controlled Fusion*, 1997.
- [66] *Proceedings 24<sup>th</sup> European Conference on Controlled Fusion and Plasma Physics, Berchtesgaden*, 1997.
- [67] P.J. McCarthy, P. Martin, and W. Schneider. The CLISTE interpretive equilibrium code. Technical report, Max Planck Institut für Plasmaphysik.
- [68] S.D. Pinches. private communication.
- [69] L. Spitzer. *The physics of fully ionized gases*. Interscience, NY, 1956.



[70] K.M. Quire. *Physical Review Letters*, 1983.

[71] P.W. Lauber. Resistive Wand-Moden und aktive Feedbackstabilisierung. Master's thesis, Universität Bayreuth, Germany, 2000.

# Appendix A

## Publications

### A.1 Contribution to Articles

Günter, S., G. Giruzzi, A. Gude, R.J. LaHaye, K. Lackner, M. Maraschek, S. Schade, S. Sesic, R. Wolf, Q. Yu, H. Zohm and ASDEX Upgrade Team: *MHD Modes in Regular and Reversed Shear Scenarios and Possibilities for their Control through Current Drive*. Plasma Physics and Controlled Fusion **41**, B231-B241 (1999)

Günter, S., S. Schade, M. Maraschek, S. Pinches, E. Strumberger, R. Wolf, Q. Yu and ASDEX Upgrade Team: *MHD Phenomena in Reversed Shear Discharges on ASDEX Upgrade*. Nuclear Fusion **40**, 1145-1155 (2000)

Günter, S., R. Wolf, F. Leuterer, O. Gruber, M. Kaufmann, K. Lackner, M. Maraschek, P. McCarthy, H. Meister, A.G. Peeters, G. Pereverzev, H. Salzmann, S. Schade, J. Schweinzer, W. Suttrop and ASDEX Upgrade Team: *Simultaneous Attainment of High Electron and Ion Temperatures in Discharges with Internal Transport Barriers in ASDEX Upgrade*. Physical Review Letters **84**, 3097-3100 (2000)

Wolf, R., S. Günter, F. Leuterer, A.G. Peeters, G. Pereverzev, O. Gruber, M. Kaufmann, K. Lackner, M. Maraschek, P. McCarthy, H. Meister, H. Salzmann, S. Schade, J. Schweinzer, W. Suttrop and ASDEX Upgrade Team: *Response of Internal Transport Barriers to Central Electron Heating and Current Drive on ASDEX Upgrade*. Physics of Plasmas **7**, 1839-1844 (2000)

*S. Günter, A. Gude, J. Hobrik, M. Maraschek, S. Saarelma, S. Schade, R.C. Wolf and ASDEX Upgrade Team: MHD phenomena in advanced scenarios on ASDEX Upgrade and the influence of localized electron heating and current drive. Nuclear Fusion* **9** 1283-1290 (2001)

*Koslowski, H.R., E. Graffmann, S. Günter, J. Rapp, S. Schade: Investigation of internal disruptions in reversed shear plasmas on TEXTOR-94. Submitted to Nuclear Fusion* (2001)

## A.2 Contributions to Conference Presentations

*Schade, S., R. Novotny, W. Kühn, H.W. Pfaff: Der HADES-Startdetektor. Verhandl. DPG (IV)* **32**, 22, HK 10.7 (1997).

*Günter, S., Q. Yu, A. Gude, H.R. Koslowski, M. Maraschek, S.D. Pinches, S. Schade and ASDEX Upgrade Team: MDH Phenomena in Low and Reversed Shear Plasmas. In: Proc. Int. Congress Plasma Phys. and 25<sup>th</sup> EPS Conf. on Control. Fusion and Plasma Phys., Prague 1998, (Ed.) P.Pavlo. ECA 22C. Europ. Phys. Soc., Geneva 1998, 1840-1843.*

*Günter, S., A. Gude, M. Maraschek, S. Schade, S. Sesic, R. Wolf, Q. Yu, H. Zohm and ASDEX Upgrade Team: Theoretische und experimentelle Untersuchungen von Neoklassischen Tearing Moden an ASDEX Upgrade. Verhandl. DPG (VI)* **34**, 347, P11.1 (1999).

*Gruber, O. et al.: Overview of ASDEX Upgrade Results. 18<sup>th</sup> IAEA Fusion Energy Conf. Sorrento 2000.*

*Gruber, O., S. Günter, A. Gude, M. Maraschek, S. Schade, S. Sesnic, R. Wolf, Q. Yu, H. Zohm, and ASDEX Upgrade Team: The Effect of MHD Modes on Confinement and Current Profile in Advanced Scenarios on ASDEX Upgrade. US-Japan Workshop on MHD Stability Limits at High Beta in Toroidal Devices, JAERI, Naka 2000.*

Günter, S., A. Gude, J. Hobirk, M. Maraschek, A.G. Peeters, S.D. Pinches, S. Saarelma, S. Schade, R. Wolf and ASDEX Upgrade Team: MHD Phenomena in Advanced Scenarios on ASDEX Upgrade and the Influence of Localized Electron Heating and Current Drive. 18<sup>th</sup> IAEA Fusion Energy Conf. Sorrento 2000

Günter, S., A. Gude, P. Lauber, M. Maraschek, S.D. Pinches, E. Strumberger, S. Schade, R. Wolf and ASDEX Upgrade Team: MDH Phenomena in Advanced Scenarios on ASDEX Upgrade. 27<sup>th</sup> EPS Conf. on Control. Fusion and Plasma Phys., Budapest 2000.

Günter, S., S. Schade, A. Gude, P. Lauber, M. Maraschek, E. Strumberger, R. Wolf and ASDEX Upgrade Team: MHD Phänomene in Advanced Tokamak-Szenarien. Verhandl. DPG (VI) **35**, 1006, P4.2 (2000).

Koslowski, H.R. E. Graffmann, S. Günter, J. Rapp and S. Schade: Untersuchung an internen Disruptionen an TEXTOR-94. Verhandl. DPG (VI) **35**, 1005, P4.1 (2000).

# Appendix B

## Danksagung

Zunächst gilt mein Dank meinen Betreuern Frau Prof. Dr. Günter und Herrn Prof. Dr. Röpke für ihre Unterstützung. Außerdem danke ich den Mitgliedern der Bereiche Tokamak und ASDEX Upgrade am Max-Planck-Institut für Plasmaphysik, die mir während der Promotionszeit ein angenehmes und fruchtbares Arbeitsumfeld boten.

Bei der Zusammenarbeit haben meine Kollegen nicht nur Offenheit für Fragen bewiesen, sondern sich oft Zeit für wertvolle Erklärungen genommen. Dafür sei ihnen an dieser Stelle mein herzlicher Dank ausgesprochen. Insbesondere möchte ich an dieser Stelle erwähnen: Dr. Coster, Dr. McCarthy, Dr. Peeters Dr. Pinches, Dr. Scott, Dr. Strumberger, Dr. Yu und Dr. Zehrfeld.

Ich danke sowohl den "native speakers" der Abteilung für sprachliche Hinweise, als auch den zahlreichen Kollegen, die mir mit fachlichen Anregungen und Kommentaren geholfen haben.

# Appendix C

## Curriculum Vitae

Name: *Diplom-Physiker*  
*Stefan Schade*

Geburtstag: *29.12.'72*

Geburtsort: *Braunfels*

'79-'89 *Grund- und Gesamtschule an der Schwingbachschule, Hüttenberg*

'89-'92 *Gymnasiale Oberstufe an der Goetheschule, Wetzlar*  
*Leistungskurse: Mathematik und Physik, Abschluß: Abitur*

'92-'97 *Physikstudium an der Justus-Liebig-Universität, Gießen*  
*Diplomarbeit in experimenteller Hochenergiephysik, Abschluß: Diplom*

'97 *Preis der Heraeus-Stiftung wegen Diplomnote "sehr gut" in 10 Semestern*

'97 *"Summer University" des Max-Planck-Instituts für Plasmaphysik,*  
*Greifswald*

WS '97/'98 *Beginn des Promotionsstudiums an der Universität Rostock*

seit 11/'97 *Wissenschaftliche Mitarbeit am Max-Planck-Institut für Plasmaphysik,*  
*Garching — In diesem Rahmen entstand die vorliegende Arbeit.*

# Appendix D

## Erklärung

*Hiermit versichere ich, daß ich die vorliegende Arbeit selbstständig angefertigt und ohne fremde Hilfe verfaßt habe, keine außer den von mir angegebenen Hilfsmitteln und Quellen dazu verwendet habe und die den benutzten Werken inhaltlich und wörtlich entnommenen Stellen als solche kenntlich gemacht habe.*

*Garching bei München, den 24.7.2001*